

THESIS

QUANTITATIVE ANALYSIS OF THE MECHANICAL ENVIRONMENT IN THE
EMBRYONIC HEART WITH RESPECT TO ITS RELATIONSHIP IN CARDIAC
DEVELOPMENT

Submitted by

Alexander T. Bulk

Department of Mechanical Engineering

In partial fulfillment of the requirements

For the Degree of Master of Science

Colorado State University

Fort Collins, Colorado

Fall 2015

Master's Committee:

Advisor: Lakshmi Prasad Dasi

Co-Advisor: Deborah Garrity

Ketul Popat

Christopher Orton

Copyright by Alexander Thomas Bulk 2015

All Rights Reserved

ABSTRACT

QUANTITATIVE ANALYSIS OF THE MECHANICAL ENVIRONMENT IN THE EMBRYONIC HEART WITH RESPECT TO ITS RELATIONSHIP IN CARDIAC DEVELOPMENT

In order to understand the causes of congenital heart defects, which afflict at least 4 infants per 1,000 live births, research has implemented the use of animal models to study embryonic heart development. Zebrafish (*Danio rerio*) have become one of the more prominent of these animal models due to the fact that their heart morphology at the earliest stages of development is remarkably similar to humans, and because embryos lack pigmentation, rendering them transparent. This transparency allows for high-speed images of blood flow to be acquired in the developing heart so that the mechanotransductive relationship between the intracardiac flow environment and myocardial progenitor cell differentiation can be understood. One particular aspect of the flow environment, a cyclic retrograde flow at the junction of the forming atrium and ventricle, has been shown to be necessary for valve formation, though the mechanisms causing it to occur had previously been unknown. By comparing the results of two-dimensional spatiotemporal analysis applied to embryos both with normal retrograde flow and inhibited retrograde flow, this study shows that a particular range of pressures associated with the pumping mechanics of the heart as well as resistance due to systolic contractile closure must exist in order to maintain adequate retrograde flow to induce valve formation. The use of two-dimensional spatiotemporal analysis was sufficient to acquire these results, however when applied to analysis of other aspects of

the intracardiac flow environment, this computational method is subject to critical limitations. Therefore, this study includes the development of methodology to integrate the results of spatiotemporal analysis on multiple focal planes bisecting the heart into a more accurate, three-dimensional result. The results of this study not only increase our understanding of the mechanics behind an important factor in embryonic development, but also enable future experiments pertaining to the measurement of embryonic intracardiac blood flow to be performed with increased certainty.

ACKNOWLEDGEMENTS

Numerous individuals have provided me with substantial guidance throughout my graduate career, of whom I would like to acknowledge. In particular I would like to thank my advisor, Dr. L. Prasad Dasi, as I feel extraordinarily lucky to have been given the chance to work with you. It is without a doubt that I would not have learned as much nor accomplished what I have in the last year and a half without your mentorship. I would also like to give notable thanks to my co-advisor, Dr. Deborah Garrity, and to Dr. David Bark, as both of you have consistently taken the time to provide me with critical advice on both my research and career throughout these years. I would like to thank my committee members, Dr. Ketul Popat and Dr. Christopher Orton for their advisement in completing this thesis as well as Dr. Brennan Johnson for creating and guiding me through the software and experimental protocol used throughout my studies.

I would like to acknowledge the Mechanical Engineering Department for supporting me through a Graduate Teaching Assistantship as well as give thanks to my T.A. advisor, Dr. Kimberly Catton for the invaluable experience you have offered me as well as the advice you have given me in my teaching.

Last but not least, I would like to acknowledge all of the members of the Dasi Cardiovascular & Biofluid Mechanics Lab and the Garrity Lab for all of their friendship and support, especially to August Martin, Molly Zeller, and Neha Ahuja for all of their help with performing some of the most difficult experiments on zebrafish embryos.

TABLE OF CONTENTS

ABSTRACT	ii
ACKNOWLEDGEMENTS	iv
TABLE OF CONTENTS	v
LIST OF TABLES	vii
LIST OF FIGURES	viii
1. INTRODUCTION	1
2. LITERATURE REVIEW	5
2.1 Congenital Heart Disease	5
2.2 Embryonic Zebrafish as a Model to Study Heart Development	7
2.3 Mechanical Environment in the Developing Heart	14
2.4 Relationship of Mechanics to Heart Development	23
2.5 Methods for Analyzing Embryonic Heart Function	32
3. AIM 1	46
3.1 Methods: Experimental Groups	46
3.2 Methods: Zebrafish Breeding and Embryo Preparation	48
3.3 Methods: Centrifugation	50
3.4 Methods: Imaging the Embryonic Heart	54
3.5 Methods: Estimating Pressure due to Chamber Contraction and Expansion	56
3.6 Methods: Diameter Measurement	59
3.7 Methods: Length of Closure Measurement	61
3.8 Results: Pressure due to Chamber Expansion/Contraction	63

3.9 Results: Length of Endothelial Closure	68
3.10 Discussion.....	71
4. AIM 2.....	78
4.1 Methods: Zebrafish Embryo Preparation and Imaging	79
4.2 Methods: Estimating the Shape of the Intracardiac Flow Profile	85
4.3 Methods: Estimating Mean Velocity, Flowrate, and Further Parameters.....	91
4.4 Results of Multi-Focal Plane Spatiotemporal Analysis on a Test Embryo	94
4.5 Discussion.....	101
5. CONCLUSION	112
5.1 Summary of Results.....	112
5.2 Original Contributions.....	114
5.3 Future Work	116
REFERENCES.....	118

LIST OF TABLES

Table 3.1: Periods of Centrifugation and Associated Developmental Stages.....	51
Table 4.1: Output Parameters Descriptive of Overall Heart Function using both Multi-Focal Plane Spatiotemporal Analysis and Two-Dimensional Spatiotemporal Analysis on a Test Embryo.....	99
Table 4.2: Error in Diameter, Velocity, and Distance between Focal Planes and Associated Propagated Error of Estimated Parameters	101

LIST OF FIGURES

Figure 2.1: Mouse, Chick, and Zebrafish Embryos	10
Figure 2.2: Formation of the Embryonic Heart Tube	11
Figure 2.3: Heart Development in the Zebrafish.....	13
Figure 2.4: Pumping Mechanics of the Valveless Post-Tube Stage Embryonic Heart ..	17
Figure 2.5: The Actin-Myosin Chain Complex	19
Figure 2.6: Shear Stress vs. Shear Rate of Blood at Various Hematocrit, Fibrinogen Levels.....	21
Figure 2.7: Effect of Flow-Induced Shear Stress on Cultured Endothelial Cells.....	26
Figure 2.8: Model of Shear Stress-Mediated Mechanotransduction in Endothelial Cells	27
Figure 2.9: Relationship Between Retrograde Flow, KLF2a, and Valvulogenesis.....	31
Figure 2.10: Embryonic Zebrafish Heart Imaged Under OCT, Confocal, and Bright-Field Microscopy	34
Figure 2.11: Example Spatiotemporal Plots of Diameter and Velocity Generated with KAT	40
Figure 2.12: Velocity Calculation of an Example ST Plot Bin via Radon Transform.....	42
Figure 3.1: Scale of Chorionated and Dechorionated Zebrafish Embryos.....	50
Figure 3.2: Centrifugation Experimental Setup.....	53
Figure 3.3: Differential Cylindrical Control Volume to Estimate Pressures due to Chamber Diameter Change	57
Figure 3.4: Locations of Diameter Measurement in the Atrium and Ventricle.....	60
Figure 3.5: Eccentric Deformation and Contractile Closure Length Measurement in the Atrium/AVC	62
Figure 3.6: Timing of Retrograde Flow at the AVC Relative to Chamber Expansion and Contraction.....	64

Figure 3.7: Pressure Differences due to Chamber Expansion and Contraction in Relation to Retrograde Flow.....	67
Figure 3.8: Atrial and AVC Endothelial Closure Length in Relation to Retrograde Flow.....	69
Figure 3.9: Model Illustrating the Dual Mechanisms Regulating Retrograde Flow	74
Figure 4.1: Orientation of Embryo for Approximate Alignment of Chambers.....	81
Figure 4.2: Focal Depth Determination and Z-Axis Calibration of the Olympus SZX12 Microscope.....	84
Figure 4.3: Generation of Polar Points about the Intracardiac Flow Profile from “Diameters” Measured on Separate Focal Planes through Spatiotemporal Analysis	88
Figure 4.4: Area Calculation of the Intracardiac Flow Profile and Associated Error Resolution	90
Figure 4.5: Mean Velocity Calculation of the Intracardiac Flow Profile through Riemann Sums.....	92
Figure 4.6: Snapshots of the Embryonic Zebrafish Heart on Separate Focal Planes....	95
Figure 4.7: Output Parameters Across a Cardiac Cycle using Multi-Focal Plane Spatiotemporal Analysis on a Test Embryo.....	96-98
Figure 4.8: Diagram Illustrating the Limitation of Multi-Focal Plane Velocity Estimation	109

1. INTRODUCTION

In order for the heart to form normally during embryonic development, it must be exposed to a particular mechanical environment, both in terms of intracardiac blood flow mechanics, or hemodynamics, and pumping mechanics of the cardiac tissue. This mechanical environment induces cyclic forces, stresses, and pressures on the cardiac progenitor cells, which lead to signaling cascades that ultimately control cellular differentiation and organization. When the mechanical environment in and around the embryonic heart is altered, the morphology of the heart is affected, which is likely the cause of congenital heart defects, or CHDs. Though numerous alterations to various aspects of intracardiac flow and pumping mechanics have been determined to be highly correlated to various forms of CHDs, the exact cause of most CHDs remains elusive.

To study potential causes of CHDs, first, the mechanical environment necessary for cardiac development to occur normally must be understood. Invasive research on human embryos can present both medical and ethical implications, therefore zebrafish (*danio rerio*) are used as an animal model to study heart development. At the earliest stages of heart formation, zebrafish exhibit strikingly similar morphology to humans, both in structure as well as in gene expression. Zebrafish are also an excellent model due to their lack of pigmentation during these earliest developmental stages, allowing the structure of the heart and the flow of intracardiac red blood cells to be viewed with extraordinary detail under microscopy.

This detailed motion of red blood cells within the heart is able to be captured as high-speed image sequences and processed such that intracardiac flow can be computationally analyzed. Because of this capability, this research uses various computational methods to quantitatively analyze aspects of both the intracardiac flow mechanics and pumping mechanics of the cardiac tissue related to specific morphological phenomena. **The overarching hypothesis of this thesis is that both pumping and intracardiac flow mechanics in the embryonic heart can be quantified to better understand aspects of the overall mechanical environment influencing heart development.** This hypothesis is tested through two aims:

First, Aim 1 focuses on the pumping mechanics necessary to induce the hemodynamic conditions that drive one morphological phenomenon: the formation of a valve at the junction of the forming chambers of the heart, known as the atrioventricular junction, or AVJ. Previous research has determined that the presence of an adequate level of retrograde flow for a short duration of each cardiac cycle flowing through the atrioventricular canal (AVC) interior to the AVJ is necessary for normal valve formation. Though it has been illustrated that this retrograde flow is a regulator of valve development, the mechanisms causing it to occur had not been elucidated. Here, two important factors were determined to be linked with this retrograde flow: Pressure difference across the AVC generated by simultaneous expansion of the atrium and contraction of the ventricle was investigated as a driving mechanism of retrograde flow, and resistance due to contractile closure of the atrium and AVC was investigated as an inhibiting mechanism. To measure these two parameters, computational analysis was

performed on high-speed image sequences of embryonic zebrafish hearts captured under bright-field microscopy. Retrograde flow was inhibited in some embryos by non-invasively altering the cardiac preload at earlier developmental time points through centrifugation. It was found that the occurrence of retrograde flow was significantly correlated with the pressure difference across the AVC created by the expansion and contraction of the atrium and ventricle; though this mechanism failed to solely explain the occurrence of retrograde flow on its own. A secondary mechanism restricting retrograde flow to only the period of the cardiac cycle observed was then postulated based on data describing the resistance due to contractile closure. Overall, the sensitivity of the hemodynamic conditions necessary for cardiac development to small changes in pumping mechanics were illuminated in this study.

Next, Aim 2 focuses on the development of computational methodology to more accurately quantify numerous parameters associated with both intracardiac flow and overall heart function. Various computational flow-measurement methods have been used to analyze embryonic intracardiac flow, though all are subject to critical limitations that result in significant error. One of the most successful of these methods implements spatiotemporal analysis of two-dimensional image sequences captured across a focal plane bisecting the heart. Because analysis is only performed in two dimensions, multiple assumptions must be made that limit the accuracy of this method. In this study, a complementary algorithm was developed to enhance software used for spatiotemporal analysis to address the constraints elicited by limiting analysis to two dimensions. The algorithm allows for image sequences of the embryonic heart to be

captured on multiple focal planes so that they can be integrated to obtain a more accurate, three-dimensional result. Upon implementing this multi-focal plane method in analysis of a test embryo, error analysis was performed to evaluate its accuracy in comparison with the previous method. The multi-focal plane approach was found to result in a significant reduction in downstream error. Due to the prominence of intracardiac flow studies in embryonic zebrafish, this refined method of analysis will greatly benefit future research aimed at improving our understanding of cardiac development.

This thesis will be organized into four subsequent chapters. The following chapter is a literature review that provides the framework for the motivation behind this research and implemented theories and techniques. Chapters 3 and 4 will cover Aims 1 and 2, respectively. In those two chapters, the methods used, results obtained, and a discussion of those results will be provided. Since the focus of Aim 2 is on development of methodology, the results section in chapter 4 will be concentrated on validation of that methodology. Finally, chapter 5 will provide the conclusion of the thesis, which will be divided into three sections: 1) a summary of the results, 2) a list of article submissions, conference presentations, and seminars performed related to the material of this thesis, and 3) a discussion of ongoing and future research related to the results of this thesis.

2. LITERATURE REVIEW

The following chapter provides an overview of the past research that provided motivation for this work, as well as theories utilized in the experimental methodology. This chapter will be divided into five sections: Section 2.1 provides an overview of congenital heart disease, its causes, symptoms, and statistics. Section 2.2 outlines the use of embryonic zebrafish as an animal model to understand heart development. Section 2.3 covers existing scientific understanding of the pumping and flow mechanics within the embryonic heart. Section 2.4 provides an explanation as to the relationship between the internal flow mechanics within the heart and cellular response in coordinating heart development. Finally, Section 2.5 reviews alternate methodologies for analyzing embryonic heart function.

2.1 Congenital Heart Disease

Congenital Heart Disease, or Congenital Heart Defects, (CHDs) consist of significantly impaired cardiac function arising from alterations in the structure of the heart or intrathoracic vessels during embryonic development [1]. Depending on the study, the incidence of CHDs varies between 4 and 50 infants per 1,000 live births [2]. In 2000, it was estimated that 800,000 American adults were afflicted with CHDs [3]. Ventricular Septal Defects (VSDs) are the most common form of CHDs, often resulting in a heart with a single-ventricle physiology. If trivial lesions are included in the statistics of VSDs, the incidence of CHDs increases to 75 infants per 1,000 births, and as much as six of

those infants are born with moderate or severe defects [2]. The cause of a majority of CHD cases are relatively unknown, though many are believed to be due to abnormal gene expression arising from mechanotransduction factors, or any mechanism by which cells convert mechanical stimulus into a chemical response. Only 20% of CHDs have been attributed to chromosomal anomalies, and only 3-5% are known to be due to mutations in single genes [4]. Patients suffering from Down syndrome and Edwards syndrome, for instance, have an approximately 45% and 90% chance of developing CHDs, respectively [5]. In the approximately 80% of the remaining CHD cases likely caused by mechanotransduction factors, abnormal differentiation of cardiac cells is assumed to be the result of changes in the complex relationship between these cells and their environment. For example, maternal diabetes can alter the physiology of the pregnancy to such an extent that the likelihood of the fetus developing a CHD can increase by 500% [2].

Mechanical stresses related to the contraction and expansion of cardiac muscle tissue as well as blood flow dynamics within the heart are some of the most studied mechanotransduction factors affecting congenital heart disease. The evidence suggests that myocytes have the capacity to adapt and remodel under varying mechanical loads both structurally and functionally, and this response is assumed to mechanistically be the same in cardiomyocytes during development [6]. The developing heart in vertebrates typically used as animal models to study human heart development begins to contract and effectively pump blood throughout the embryo long before circulation is necessary to supply the body with oxygen, which supports the notion that

the pumping and flow mechanics at these early stages are necessary for normal cardiogenesis [7]. The exact parameters of these mechanics transduced by the cardiac cells as well as the signaling pathways linking mechanotransduction to differentiation, however are less understood. Fluid shear stresses and pressure gradients on the interior endothelial cells of the heart, elastic stresses associated with myocytic contraction, and even fluid vorticity associated with chamber anatomy have all been studied as key parameters involved in various aspects of heart development [8, 9].

2.2 Embryonic Zebrafish as a Model to Study Heart Development

Many types of animal models have been used to research cardiac development; one of the most widely used is the mouse. The mouse is an effective model in that it is genetically and developmentally more closely related to humans than other non-mammalian models. Unfortunately, like all mammalian models, the development of the mouse occurs *in utero*, requiring the mother to be sacrificed in order to view the embryo [10]. Nutritional and environmental information is also transduced from the mother to the embryo via the placenta, so by removing the embryo from the uterus, important physiological factors that regulate normal development are removed [11]. Embryo dissection results in a limited *ex-utero* survival of only two days, requiring normal heart function in the mouse embryo to only be observed *in-utero* [12]. Ultrasound is the most effective imaging modality for viewing the embryonic heart *in utero*, however it is limited by its spatial and temporal resolution [13]. This limitation makes the embryonic mouse

an adequate model for viewing developmental cardiac anatomy, but an insufficient model for measuring the intracardiac flow environment during development [13].

Another widely used animal model is the chick embryo, which has the benefit of developing externally from the mother. Although adult morphology of the chicken heart is much less similar to the human heart than that of the mouse, at the earliest stages of development, cardiac morphology in all vertebrates is nearly identical [14]. An added benefit of the chick embryo model is that despite the fact that it requires the environment within the egg to supply it with the necessary nutrients, small portions of the egg shell can be removed without drastically impairing heart function as long as the imaging occurs at a maintained incubation temperature [15, 16]. By implementing 4-D optical coherence tomography, (OCT) intracardiac flow mechanics are then able to be observed, unlike with *in-utero* models, by injecting Indian ink into the blood [17]. Unfortunately, OCT is limited to large-scale blood flow patterns, and inaccuracies when applying computational flow-measurement methods to OCT-captured images require the use of Doppler ultrasound for comparison and validation [18].

The embryonic zebrafish (*Danio rerio*) is another widely-used animal model to study embryonic development. Though zebrafish cardiogenesis concludes with the formation of only a single atrium and ventricle, unlike the four-chambered hearts of the chicken and mouse, early stages of heart development are remarkably comparable to humans [14, 19, 20]. Zebrafish embryos also possess a complex circulatory system and organ system counterparts that are strikingly similar to that of all mammals [19]. An important

benefit of the zebrafish embryo model is that the embryo is able to receive oxygen through diffusion until late in embryonic development, which allows for even the most severe alterations to the cardiovascular system to be made without drastically affecting the overall health of the embryo [21]. Zebrafish embryos are also easy to maintain, and develop much more rapidly than other animal models [21]. Most importantly, the zebrafish embryo is fertilized externally so that embryonic time points can be measured accurately, and the embryo is transparent prior to approximately 55 hours post-fertilization (hpf), allowing for the individual red blood cells (RBCs) within the heart as well as the overall heart structure to be viewed with vivid detail [22, 23]. Because zebrafish matings can yield up to hundreds of eggs, large genetic screens have been widely performed and many different cardiovascular mutant phenotypes that emulate adult human CHDs have been recognized [20, 24, 25].

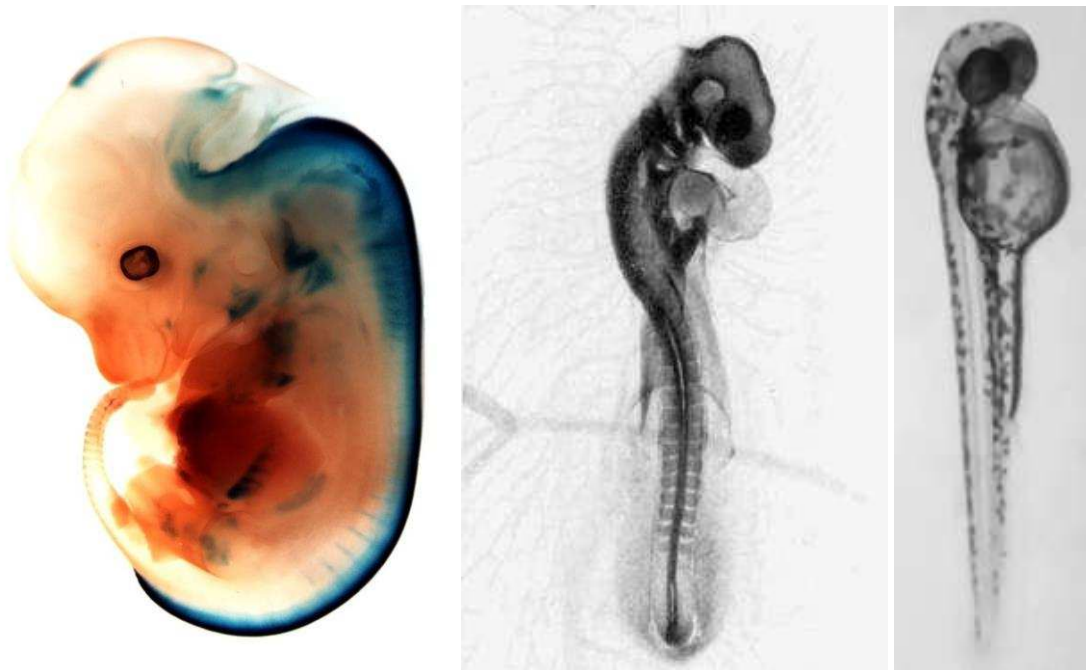


Figure 2.1: Mouse, Chick, and Zebrafish Embryos

Left: Mouse Embryo at 12 days post-fertilization. Image taken from Schmidt, et al., 2009 [26]. **Center:** Chick Embryo at ~51-56 hpf (hours post-fertilization). Image taken from Hamburger and Hamilton, 1951 [27]. **Right:** Zebrafish Embryo at 48 hpf. Image taken from Scholz, et al., 2008 [28].

Like all vertebrate embryos, zebrafish embryos contain three germ layers consisting of progenitor cell populations that differentiate into the various organ systems of the adult body: the ectoderm, mesoderm, and endoderm [29, 30]. The mesoderm is the germ layer from which the heart differentiates, beginning with a progenitor cell population called the anterior splanchnic, or cardiogenic mesoderm [30, 31]. The myocardial cells are derived from two laterally-aligned crescent-shaped cell populations within the cardiogenic mesoderm called “cardiogenic plates” that loop into two laterally-aligned heart tubes, or “tubular primordia” at 20 hpf [14, 31]. In between these cardiogenic plates lies the progenitor population of the endocardial cells, called the “endothelial plexus,” which diverges and migrates from a population of hematopoietic and vascular lineages [32]. Meanwhile, atrial progenitor populations and ventricular progenitor populations are aligned such that the ventricular progenitors are on the proximal side of

the heart tubes, whereas the atrial progenitors are distal [22]. The two cardiogenic heart tubes then migrate towards each other and fuse around the endocardial progenitors to form a single heart tube with the endocardial cells interior to the myocardial cells by 24 hpf [14, 33].

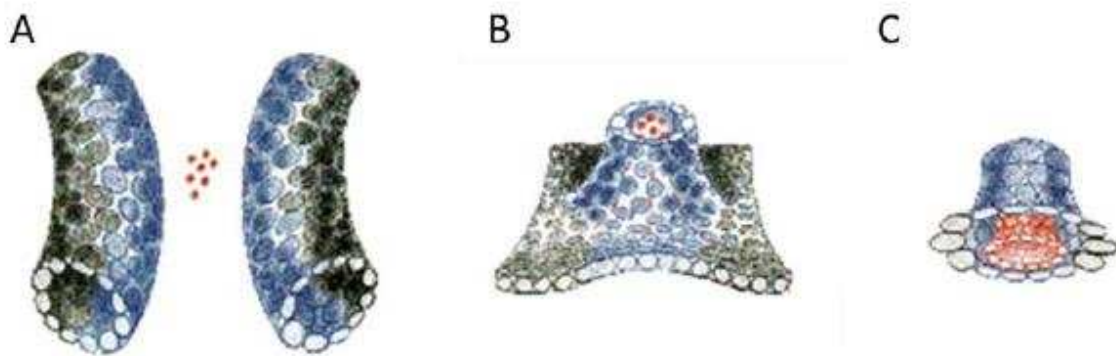


Figure 2.2: Formation of the Embryonic Heart Tube

A: Tubular primordia with ventricular progenitors (purple) and atrial progenitors (black) around endocardial progenitors (red). **B:** Fusion of tubular primordia around endocardial progenitors, with separation of atrial and ventricular progenitors. **C:** Final heart tube configuration. Image taken from Bakkers, et al., 2011 [34].

After formation of the heart tube, the cardiac jelly, an extracellular matrix of extremely thin fibrils, is formed in between the layers of endocardial and myocardial progenitors originating from the latter [35-37]. The role of the cardiac jelly is not completely understood, though it is presumed to increase the efficiency of pumping mechanics by providing cushioning as well as stored recoverable energy through elastic properties to aid in passive expansion [35, 37]. The reason for this presumption is because the cardiac jelly is composed of an arrangement of cross-banded collagen fibrils, along with an assortment of other glycoproteins, which are known to have elastic properties [38, 39]. This elastic behavior has been exhibited by the cardiac jelly in that when isolated

from the rest of the heart in chick embryos, the cardiac jelly will revert back to its original size and shape [37, 39].

By 30 hpf, the posterior end of the heart tube begins to bend in an S-shape up towards the embryo's left side, in a process called cardiac looping [30, 34]. It has been hypothesized that the cardiac jelly also plays an important role in both signaling and structural control of the looping process [37]. Some literature states that looping is complete by 48 hpf, though there is disagreement on the actual termination of looping, as overall changes in heart structure continue beyond full pigmentation of the embryo [40]. Throughout the process of cardiac looping, two regions of the tube balloon into the two chambers that define the atrium and ventricle, and the region intermediate to the chambers constricts to form the atrioventricular junction (AVJ) [41]. Morphology of the human heart is equivalent to that of the zebrafish through 48 hpf, though beyond this point, the human heart begins to develop septa that divide the two chambers into the final four-chambered structure [36].

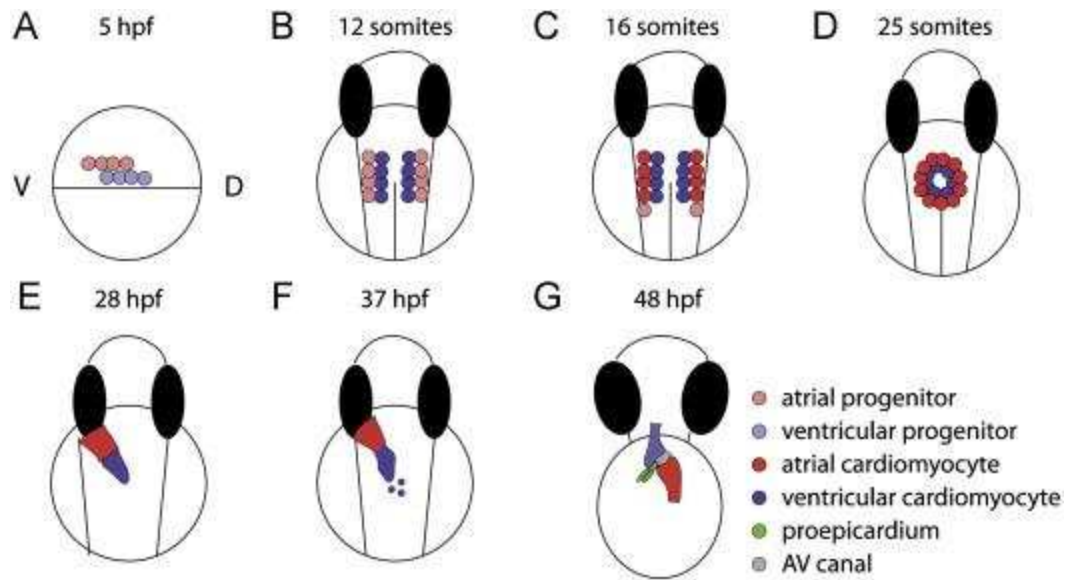


Figure 2.3: Heart Development in the Zebrafish

A-D: Organization of cardiomyocyte progenitor populations and migration and fusion to the heart tube morphology. **E-G:** Cardiac looping of the heart tube, where **E** and **F** are dorsal views and **G** is a ventral view. Image taken from Tu and Chi, 2012 [22].

Circulation within the heart begins almost immediately after formation of the heart tube around 24 hpf through coordinated contractions that propagate along the length of the tube [14]. These coordinated contractions move in a wave-like motion, exhibiting peristaltic-like pumping that maintains unidirectionality of blood flow, though the exact pumping mechanics at this stage will be discussed in the following section [41, 42]. As the chambers forming the atrium and ventricle expand, the coordinated contractions along the tube transition into independent contractions of the separate chambers [43]. The contractions of the atrium and ventricle are highly synchronized such that expansion of the atrium occurs simultaneously with contraction of the ventricle, and vice versa. At this stage, unidirectionality of flow however is no longer able to be maintained until the formation of a valve from the endothelial cushions around 105-111 hpf, resulting in a significant amount of flow moving in reverse for a brief period of each cardiac cycle [34, 40, 41].

2.3 Mechanical Environment in the Developing Heart

As stated in the previous section, during the tube-stage of heart development, coordinated contractions along the length of the tube appear to pump in a peristaltic manner. Prior to 2006, it was believed that the heart tube functioned as a technical peristaltic pump [42]. Peristalsis is defined as the progression of area contraction or expansion propagating in a wave-like motion along the length of a distensible tube of fluid in which the mean velocity of the fluid is relatively the same as the wave velocity [44]. Forouhar et al. showed in 2006 using confocal microscopy however, that the mean velocity of blood in the heart tube is significantly greater than that of the wave velocity, rendering the peristalsis theory invalid [42, 45]. Instead, it has been suggested that the tube functions as a “Liebau pump,” or impedance pump based on two observed phenomena [42, 45]: First, the maximum acceleration of blood within the tube and maximum local pressure gradients associated with contraction exhibit a large phase difference; Secondly, the contraction waves reflect off of the boundary of the heart tube [45]. Moreover, in the heart tube, the relationship between flow and heart rate is nonlinear, as is the case in an impedance pump, whereas with a peristalsis pump, flow is linearly related to wave frequency, or the heart rate [46].

The impedance pump theory of the heart tube is not widely accepted, however, and the exact pumping mechanisms of the tube-stage heart are still under debate. A typical impedance pump operates near its resonant frequency, however research has shown that the resonant frequency of the heart tube should be far greater than the observed

frequency [46, 47]. In a technical impedance pump, there should also be only one site of active contraction or expansion, with passive contraction/expansion occurring in the propagating wave [48]. In the heart tube however, there appear to be multiple sites of active contraction, which can be partially explained by a multi-stage impedance pump model [49]. In the multi-stage model, active contraction occurs at multiple locations, causing interference of the propagating waves [49]. Maes, et al. however showed in 2012 that multi-stage impedance could not be the mechanism of pumping by examining signaling between myocardial cells along the tube wall [48]. It was found that calcium signaling propagated along the myocardial cells at the same instant as contraction occurred, indicating that contractions are coordinated similar to a peristaltic pump [48]. Since both multi-stage impedance and peristalsis have been refuted as the innate pumping mechanisms of the tube-stage heart, it has been suggested that the heart functions through a combination of both, though this theory has yet to be examined [42, 50].

As the heart transitions from the tube stage to cardiac looping with chamber expansion, alternating independent contractions between the atrium and ventricle drive blood flow, though unidirectionality of flow is no longer able to be maintained [43]. Very little research has been conducted to understand the pumping mechanics of the valveless, post-tube stage embryonic heart. What is understood is that each chamber undergoes passive expansion to fill the chamber with a bolus of blood, and then undergoes active contraction to eject the blood, much like a classic displacement pump [50, 51]. Throughout the process of cardiac looping, the chambers increase in stiffness as they

balloon outward, and therefore the force of contraction in the atrium increases in order to maintain efficiency of ventricular filling [51]. As the atrium and ventricle contract, constriction at the atrioventricular canal (AVC) and atrial inlet is able to prevent the majority of blood flow from moving in the retrograde direction [43]. As the atrium nears the end of diastole and ventricle nears the end of systole however, a significant amount of blood is nevertheless forced in reverse across the AVC from the ventricle to the atrium [43, 50]. This atrioventricular retrograde flow is of much greater velocity than in the rest of the heart due to the nozzle effect caused by the constriction [43]. An even greater fraction of the total stroke volume also exhibits retrograde motion at the atrial inlet near the end of atrial systole.

There is a distinct difference between the pumping mechanics of the atrium and ventricle in the post-tube/pre-valve stage embryonic heart in which all ventricular cardiomyocytes contract in unison, and at systole, a significant end-systolic volume exists [52]. In contrast, the pumping mechanics in the atrium exhibit the same peristaltic-like contraction as the tube-stage heart, where coordinated contractions begin at the atrial inlet and progress upward along the atrium and subsequently, the AVJ [43]. The propagation of these contractile waves along the atrium occur for a significantly longer portion of the cardiac cycle than the contraction of the ventricle, as the atrial inlet begins filling while the anterior end of the atrium and AVJ are still fully contracted [43]. Endothelial cells in the atrium and along the atrioventricular canal (AVC) also come into direct contact during contraction, unlike in the ventricle. This difference in contraction between chambers is evidently similar to the His-Purkinje system of ventricular

conduction in higher vertebrates, despite the fact that embryonic zebrafish at early stages of development lack differentiated conduction fascicles in the ventricle [53].

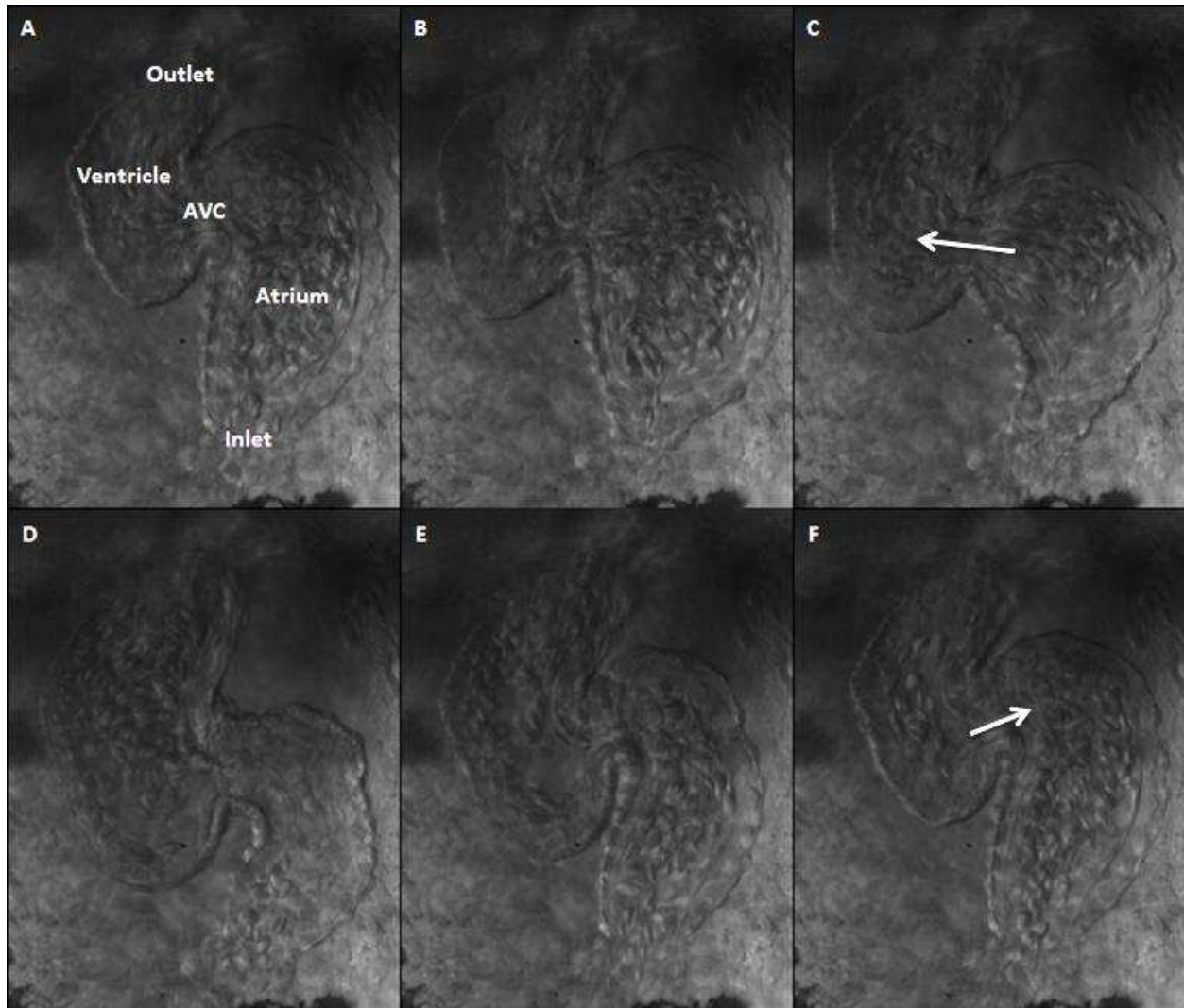


Figure 2.4: Pumping Mechanics of the Valveless Post-Tube Stage Embryonic Heart

A: As the atrium (lower chamber) nears the end of diastole, blood begins to eject into the ventricle (upper chamber). **B-C:** The inlet of the atrium contracts and the contraction wave moves along the atrium from the posterior end to the anterior end, ejecting blood into the ventricle, which begins to fill. **D:** The contractile wave propagates to the AVJ and posterior end of the atrium while the atrial inlet begins to fill. Meanwhile, the ventricle nears the end of diastole. **E-F:** The ventricle contracts, ejecting blood into the aortic arches as the atrium expands. As the atrium nears the end of diastole, a portion of blood moves in retrograde across the atrioventricular canal (AVC). Embryo is wildtype (WT) at 48 hpf. White arrows indicate the direction of flow forward (C) and in retrograde (F).

Pumping mechanics of the heart are not only critical to inducing adequate blood flow, but also play an important role in heart morphology, as elastic stresses induced on cardiomyocytes serve a mechanotransductive role in coordinating development [8]. It is not fully understood how contraction in embryonic zebrafish cardiomyocytes compares to adult cardiomyocytes, though it likely includes a similar process of binding between the proteins, myosin and actin that comprise cytoskeletal filaments. In the adult human heart, myocardial cell contraction initiates with an influx of extracellular calcium ions that bind to troponin, which then activates the actin-myosin chain complex as illustrated in Figure 2.5 [54]. This contraction induces an internal compressive stress within the myocardial cell that is opposed by an intercellular tensile stress generated by the connection to adjacent myocardial cells [55].

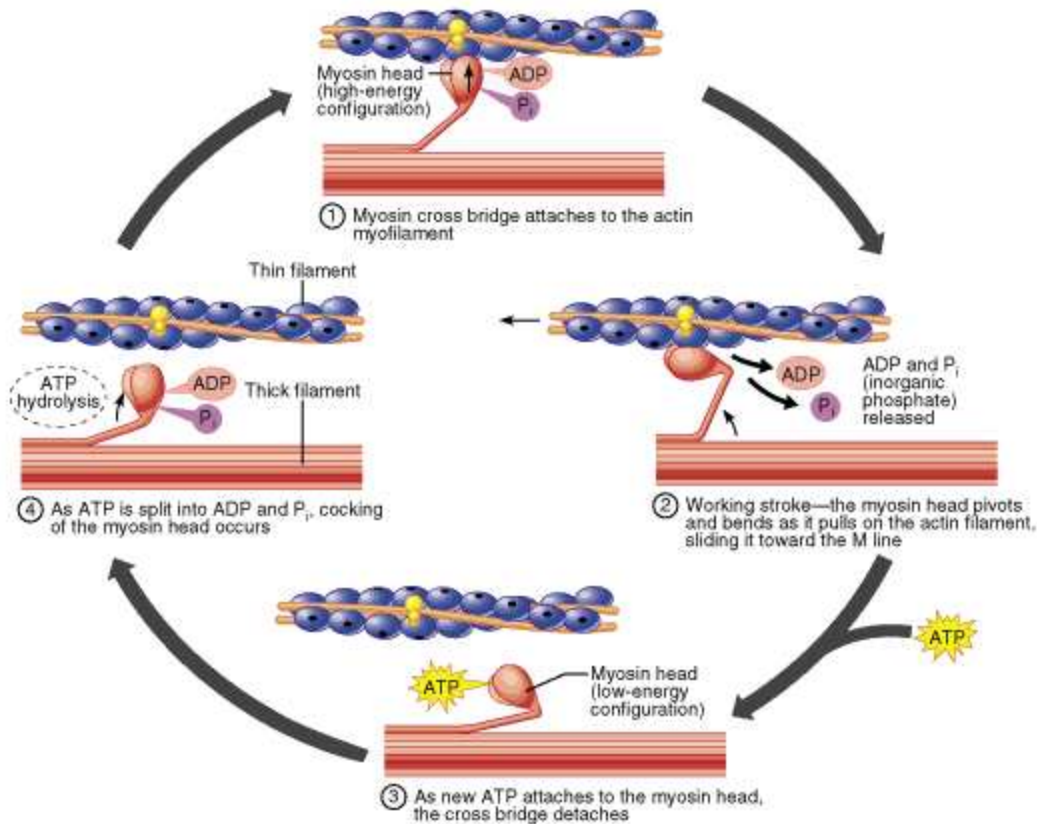


Figure 2.5: The Actin-Myosin Chain Complex

Diagram outlines the mechanism of muscle contraction through the actin-myosin chain cycle. Figure taken from Cummings, 2001 [56].

The combination of these intercellular stresses between myocardial cells results in an overall longitudinal and circumferential stress experienced by the heart during contraction. The circumferential stress, also known as hoop stress, is linearly related to the pressure within the chamber of the heart according to equation 2.1 below, where P is the intramural pressure, σ is the hoop stress, R is the heart radius, and t is the thickness of the myocardial, cardiac jelly, and endocardial layers [8].

$$\sigma = \frac{RP}{t} \quad (2.1)$$

In addition to elastic stresses, stresses on the endothelial cells within the interior of the heart generated by blood flow, or wall shear stresses, also play a critical role in heart development. In order to calculate these wall shear stresses, assumptions have to be

made based on two non-dimensional parameters that characterize the flow conditions within the heart. The first of these parameters is the Reynolds number, which describes the ratio between inertial forces and viscous forces as shown in equation 2.2 below, where D is diameter, U is the characteristic velocity, L is the characteristic length scale and μ is viscosity [8]. If the Reynolds number is below 1000, the flow is said to be laminar, and viscous forces dominate flow [8]. If the Reynolds number is greater than approximately 3300, inertial forces dominate, and the flow is considered to be turbulent [57].

$$Re = \frac{\rho UL}{\mu} \quad (2.2)$$

The second parameter is the Womersley number, which characterizes the stability of the flow profile in pulsatile flow conditions, as is the case in the cardiovascular system. The Womersley number is given in equation 2.3 below, where ω is the pulse frequency, or heart rate [8]. If the Womersley number is below 1, the velocity profile will be relatively parabolic, whereas if the Womersley number is greater than 1, the flow profile will be irregular and unstable [58].

$$Wo = L \sqrt{\frac{\omega \rho}{\mu}} \quad (2.3)$$

Because the scale of the zebrafish embryonic heart is on the order of microns, the Reynolds and Womersley numbers are low enough to be neglected, and all flow can be considered to be laminar with a stable velocity profile [9, 59]. Therefore, terms in the continuity and conservation-of-momentum equations that are proportional to these non-dimensionalized characteristic parameters can be ignored.

In a Newtonian fluid, viscosity is defined as the ratio of shear stress to shear rate, however adult human blood is considered to be a non-Newtonian fluid, as the viscosity is non-constant, increasing with greater shear rate [60]. Blood viscosity is based on both hematocrit count, or the percentage of blood consisting of RBCs, and fibrinogen content, since fibrinogen (a secreted glycoprotein involved in clotting) binds together RBCs [60]. In adult humans, the hematocrit count varies between 35-50%, but varies between 10-15% in the embryo [8]. It is assumed that fibrinogen content is not greater in the zebrafish embryo than the adult human, so based on the curves provided in Figure 2.6, blood in the embryonic zebrafish can be estimated to be approximately Newtonian and thus, of constant viscosity [60].

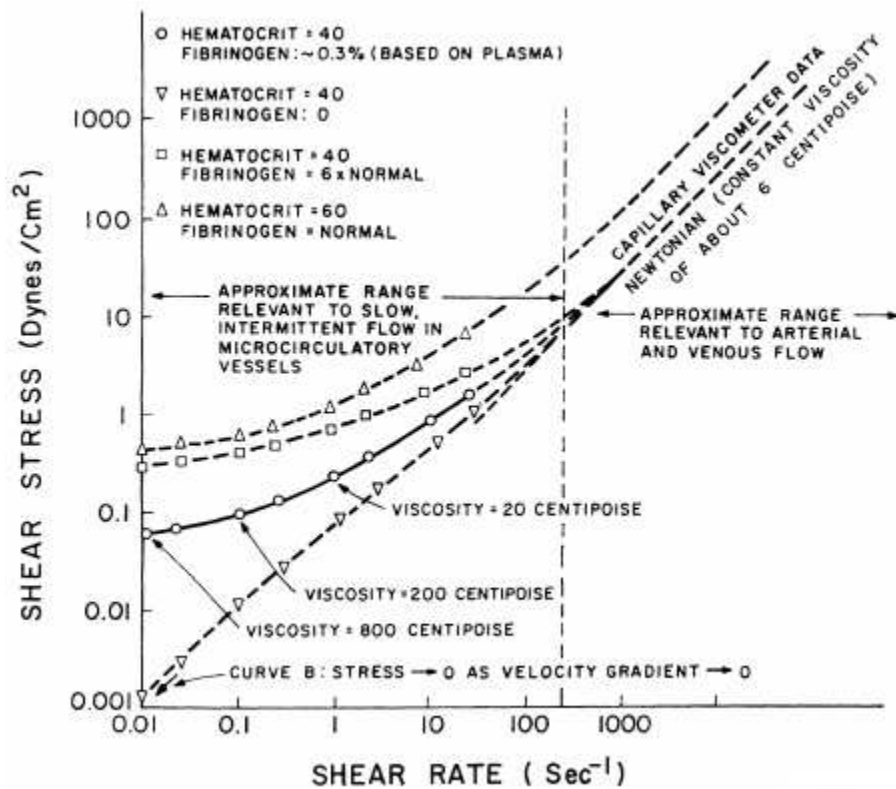


Figure 2.6: Shear Stress vs. Shear Rate of Blood at Various Hematocrit, Fibrinogen Levels
 Viscosity is calculated from the slope of the shear stress-shear rate curve. Shear stress is linearly related to shear rate in Newtonian fluids. Figure taken from Replogle et al., 1967 [60].

Since blood flow in the embryonic zebrafish heart is considered to be laminar, Newtonian and having a stable velocity profile, wall shear stress in the embryonic heart is derived from the simplified continuity equation and balance of momentum in a control volume as shown in equation 2.4, where τ_w is wall shear stress, D is diameter, μ is viscosity, Q is flowrate, v_{max} is the maximum velocity, and dP/dx is the pressure gradient in the direction of flow [8, 61].

$$\tau_w = -\frac{32\mu Q}{\pi D^3} = -\frac{4\mu v_{max}}{D} = \frac{D}{4\mu} \frac{dP}{dx} \quad (2.4)$$

By examining the first of these equations, it can be seen that as the diameter in the heart decreases, the wall shear stress increases drastically, since downstream flowrate is conserved. This observation is important since it predicts that at the constricted regions within the heart such as the AVC, atrial inlet, and ventricular outlet, the wall shear stress is dramatically greater than in the middle of the chambers [55]. This difference in shear stress is important as it is likely involved in signaling that contributes to the development of the endocardial “cushions” and later on, valves that form at the constrictions as opposed to within the chambers.

Fluid vorticity is another parameter of the mechanical environment of intracardiac flow that also likely plays an important contribution in heart development. Vorticity is defined as local rotation within a fluid, and can be quantified by the curl of the velocity field. Vorticity is understood to be vital for proper functionality in various biological systems, such as in the adult aortic sinus, where a vortex structure aids in valve closure, in preventing regurgitation, and regulating coronary flow [62, 63]. In the embryonic chick and zebrafish, vortical flow patterns have been observed around the chamber

constrictions, and it has been hypothesized that these vorticities may be involved in regulating developmental expansion of the chamber [9, 62, 64]. The presence of vorticity causes a significant change in shear stress on the endocardium, therefore it could operate as a key parameter in differentiation of signaling between various regions of the interior heart [9].

2.4 Relationship of Mechanics to Heart Development

The vast majority of research addressing the role that intracardiac flow mechanics have in regulating heart development has focused on methods to alter flow in order to observe the heart's developmental response. Because removal of blood from the embryo could contribute to off-target effects impeding other non-cardiac physiological regulators of development, the majority of experiments with wildtype embryos have focused on altering the cardiac preload, or the pressure required to fill the atrium. In chick embryos, two typical methods to reduce preload have consisted of either full or partial ligation, or intentional closure, of either the chambers of the heart or the vitelline veins preceding flow into the atrium [17, 65]. Full ligation of select vitelline veins has resulted in a vast array of malformations later in development, including effects on the ventricular septum, pharyngeal arch artery, and the semilunar and atrioventricular valves [17, 66]. Partial ligation of the left atrium has resulted in irregular orientation of myofibers as well as in dysfunction of the His-Purkinje System responsible for coordinating contraction between cardiomyocytes [65, 67]. To increase cardiac loading, partial ligation of the conotruncus just downstream of the chick embryo's left ventricle is

used to force the heart to pump harder in order to eject through a smaller area [65]. Interestingly, conotruncal ligation results in dysfunction of the same systems as left-atrial ligation, though with the complete opposite effect, such as equal but opposite myofiber angle orientation [65, 67].

Because of the miniscule size of the zebrafish embryo, ligation is not possible as with the chick embryo and therefore alternative methods are used to alter cardiac preload. One method has consisted of the use of implanted glass beads inserted at the atrial inlet and ventricular outlet in order to decrease and increase preload, respectively [9]. A wide range of defects have been observed in zebrafish embryos as a result of this method just as with the chick embryo, including blocked formation of the bulbus arteriosus (a “third chamber” that functions as a capacitor), diminished cardiac looping, abnormal valve formation, as well as notably impaired glomerular development [9, 68]. Perhaps the simplest method of altering flow in the zebrafish is achieved by altering the heart rate. By simply decreasing or increasing incubation temperature below or above the standard 28 °C, heart rate can be decreased or increased, respectively, though this also has significant effect on the overall rate of embryonic development [69, 70]. Tricaine methanesulfonate, the standard anesthetic for fish, can also be used to decrease heart rate as well as induce hypertension, and the effects can be temporary [71, 72]. Of all methods used to alter flow in the embryonic zebrafish heart, one of the less-invasive methods that results in few off-target developmental defects is centrifugation [50]. Centrifugation can be performed inside an incubator with the embryos contained in embryo media-filled plastic tubes in order to maintain exposure to

the required osmotic environment [50]. Centrifugation can also be used to reduce the cardiac preload at precise intervals in order to study the time-dependent role of flow mechanics in cardiac development [50].

It is expected that the primary cause of these morphological impairments resulting from altered loading is due to changes in the characteristic cyclical shear stress experienced by the endothelial cells. Mechanical stress on an endothelial cell, whether due to elastic tension or compression or shear stress, is known to alter the cytoskeletal structure of the cell as well as the configuration of ion channels, caveolae, pumps and various other receptors on the apical membrane [73, 74]. These changes in configuration result in changes to intracellular signaling cascades that regulate gene expression [74].

Additionally, shear stress has been shown to alter the arrangement and organization of endothelial cells in culture (Figure 2.7), which has significant effects on intercellular signaling that can also contribute to gene expression [73, 75].

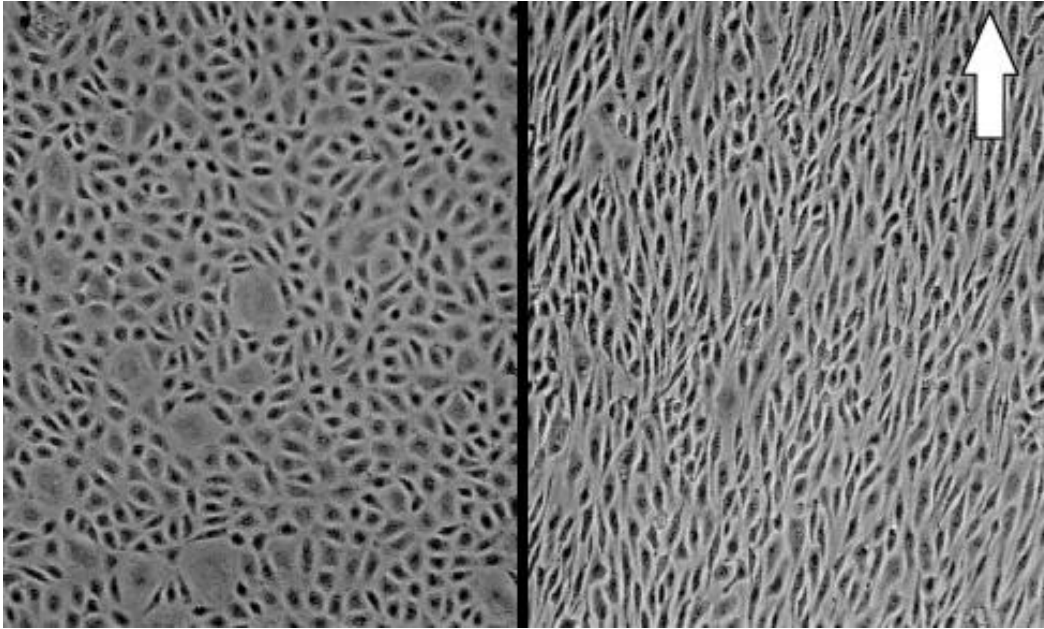


Figure 2.7: Effect of Flow-Induced Shear Stress on Cultured Endothelial Cells

Left: Endothelial cells cultured under static conditions. **Right:** Endothelia cultured under 24 hours of steady, laminar flow at 7.5 μmHg pressure. Image taken from Topper and Gimbrone, 1999 [73].

Several mechanisms are responsible for signal transduction on the membrane surface of endothelial cells. Certain potassium ion channels have been shown to require elastic stretch of the membrane in order to open, and shear stress is necessary to expose calcium ion channels by essentially pushing them open via the movement of adjoined membranous cilia [36, 76]. One of the more important transducers of shear stress is the extracellular protein framework of the glycocalyx [77]. When shear stress acts on the glycocalyx, it produces a torque, which causes deformation of the underlying hexagonal lattice-structured, actin cortical web (ACW) [77]. Deformation of the ACW is necessary for the formation and opening of caveolae, large membranous invaginations responsible for an array of signaling functions [77]. The presence of shear stress during endothelial differentiation has been shown to be necessary for the formation of this actin web as well [78].

Though multiple endothelial extracellular mechanotransducers have been discovered, in many cases the signaling pathways that they activate to modulate downstream gene expression have not been revealed, or still require the discovery of various kinases, receptors, or genes to “fill the gaps.” One well-understood pathway involves the activation of extracellular signal-regulated kinase 1/2, or ERK 1/2, through cascades originating with Tyrosine kinase and G-protein coupled receptors on the apical membrane (Figure 2.7) [79]. ERK 1/2 is known to mediate phosphorylation of key transcription factors, as well as stimulate sustained production of nitric oxide [79, 80].

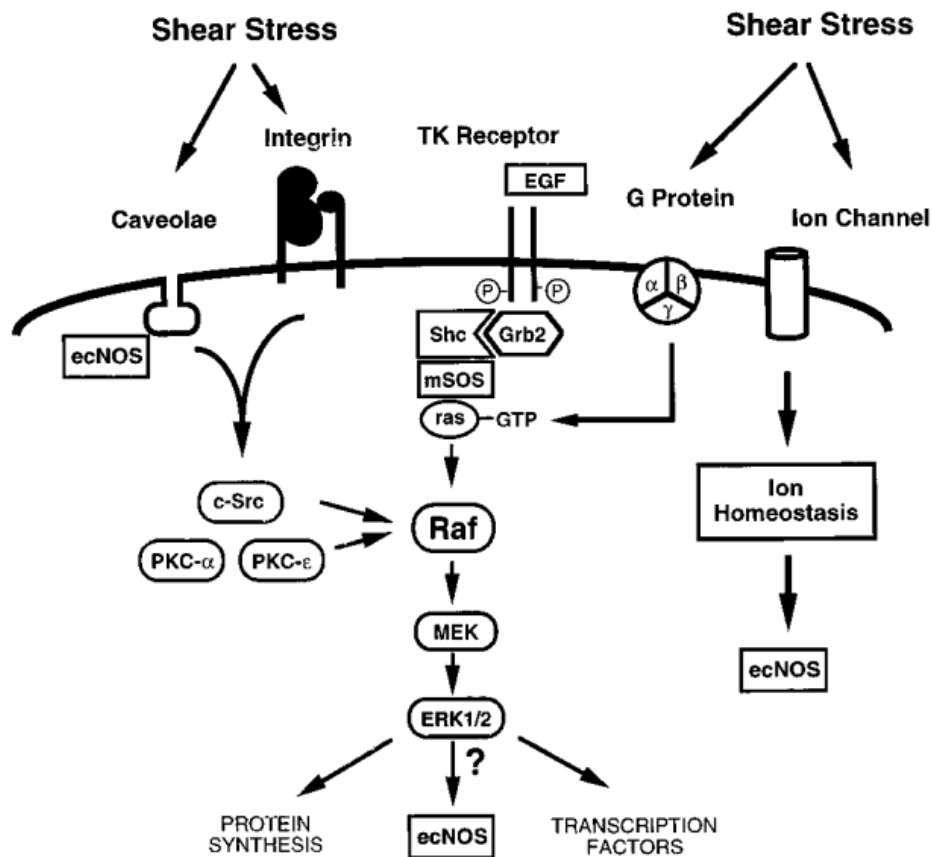


Figure 2.8: Model of Shear Stress-Mediated Mechanotransduction in Endothelial Cells
 Model of receptors and signaling cascades involved in activation of ERK 1/2 in response to shear stress. Figure taken from Traub and Berk, 1998 [80].

Despite the fact that most stress-mediated signaling pathways controlling gene expression have yet to be discovered, several key genes in the embryonic heart have been determined to be flow and/or stress-responsive. Three of the most studied of these genes have been GATA-binding protein 4 (GATA4), Filamin-C (FLNC), and Kruppel-like Factor 2 (KLF-2) [79, 81, 82]. GATA4 is a heart development-regulating transcription factor that has been shown to be necessary for mediation of cardiac remodeling in response to changes in cardiac loading, as expression has been shown to be highly responsive to ventricular swelling [79]. Along with the gene SMAD4, GATA4 has also been shown to be involved in regulating septum and atrioventricular valve formation [79, 83]. Filamin C is a cytoskeletal protein that controls the alignment of myocardial cells and formation of myofibrils at myotendinous junctions in order to maintain structural integrity of the myocardium and thus, efficiency of contractility [81, 84]. Mutations in FLNC have been shown to cause a thickening of the myocardial tissue, resulting in hypertrophic cardiomyopathy, though it is still unclear whether these mutations would be induced by altered flow [85]. Finally, KLF-2, a transcription factor which is expressed strongly in regions of high shear, is necessary for formation of an atrioventricular valve and for erythropoiesis, or RBC generation [36, 82, 86-88]. By knocking down KLF-2, an abnormal decrease in the size of the vessels occurs, which results in severe hemorrhaging throughout the cardiovascular system [36]. Though various important phenotypes have been found to be highly correlated with the expression of these genes, it is expected that these phenotypes are linked to the expression of a network of pathways combining other key developmental genes as well.

It is probable that any mutation that affects embryonic cardiac morphology will affect flow, so the response of aspects of flow involved in mechanotransduction to changes in many developmentally-related genes must also be understood. A few other important genes associated with heart development are c-Myc, EGFR, ET-1, NOS-3, and HERG [82, 86, 89-91]. C-Myc is necessary for the proliferation of cardiomyocytes, and is also likely involved in signaling of later key cardiogenesis-related genes [89]. EGFR is another precursor gene necessary to develop receptors needed for ERK $\frac{1}{2}$ signaling, and inhibition of EGFR causes severe chamber dilation with greater narrowing of the constrictions at the AVC and ventricular outlet [79, 80, 90]. ET-1 and NOS-3 are both important shear-responsive genes similar to KLF-2, though whereas NOS-3 and KLF-2 are expressed in response to high shear stress, ET-1 is expressed in response to low shear [82, 86]. Knockdown of NOS-3 results in impaired endothelial nitric oxide reception and septal defects, and knockdown of ET-1 results in similar defects to vitelline vein ligation in chick embryos [36]. HERG, or the human homologue gene in the zebrafish, ZERG, is necessary for coordinating contraction between the atrium and ventricle [91]. Mutations in ZERG cause prolonged chamber relaxation in addition to arrhythmia between contractions of the atrium and ventricle, indicating that ZERG is necessary for the activation of a conductive ion channel between the chambers in the zebrafish [91].

Of particular importance to this research are the genes involved in valve development at the AVC. In addition to KLF-2, Hyaluronic Synthase 2 (HAS2), the “Cardiofunk gene” (CFK), and Notch-1b are all necessary for the formation of the endocardial cushions

preceding valvulogenesis at the AVC [87, 92-94]. MicroRNA-23 is important in endocardial cushion formation as well, as it is needed to limit the expression of HAS2, which induces unlimited endocardial cushion growth in the absence of microRNA-23 [92]. Vermot et al. tested the expression of three genes known to be involved in valve development in response to changes in flow in embryonic zebrafish and discovered a transcription factor of the KLF family, KLF2a, was responsive to retrograde flow in the AVC [87]. GATA1 and GATA2 morphants were used to manipulate the blood viscosity by reducing the hematocrit count in order to alter the wall shear stress [87]. What was discovered was that induced consistent forward flow would result in a malformed atrioventricular valve, however wildtype embryos with a normal period of retrograde flow that would produce the same theoretical magnitude of shear stress would develop normally [87]. The absence or existence of reverse flow did not solely dictate normal valvulogenesis, though [87]. Instead, a combination of an acceptable range in magnitude and cyclical direction of shear stress are needed for normal differentiation of the endocardial cushions [87]. Not only did KLF2a become misexpressed under the absence of normal retrograde flow conditions, but by knocking out KLF2a, the same valve malformations occurred, making KLF2a an important link between retrograde flow and valvulogenesis [87].

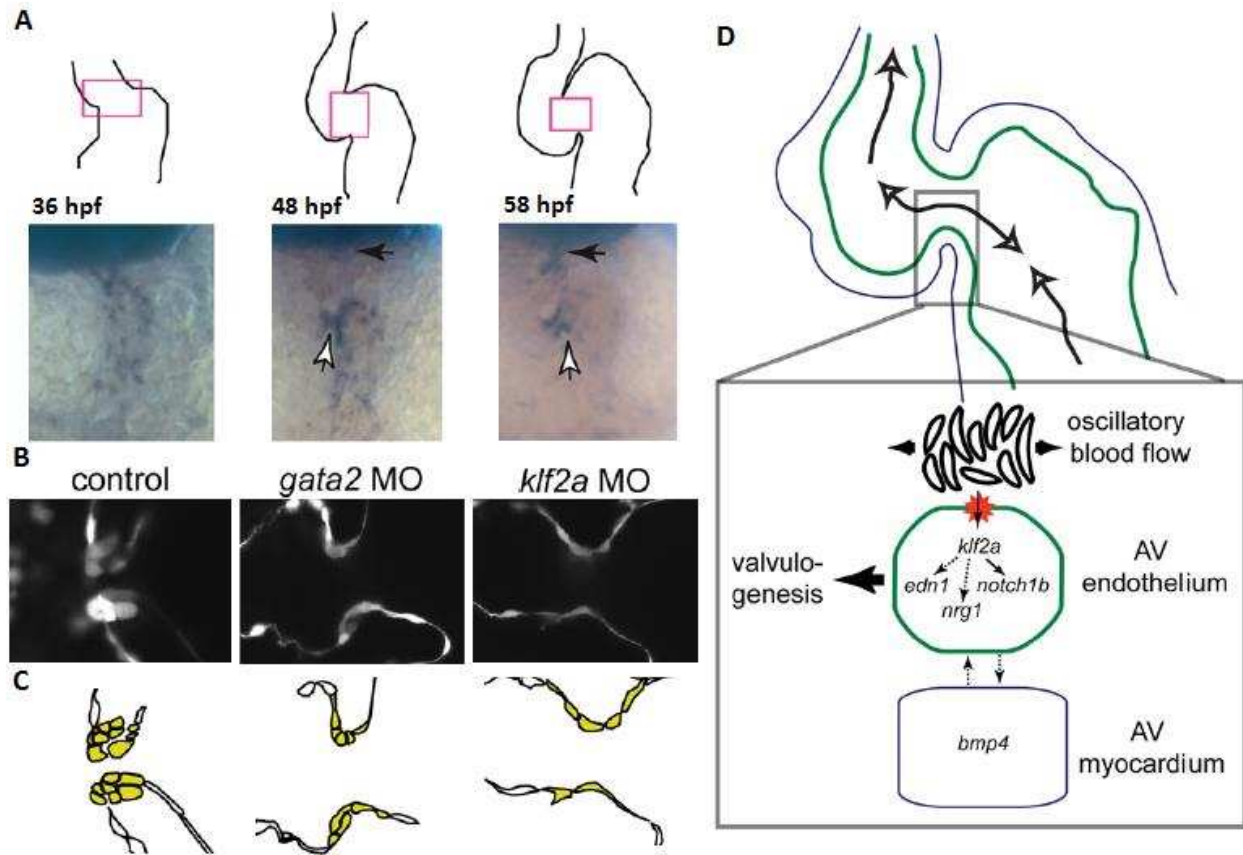


Figure 2.9: Relationship Between Retrograde Flow, KLF2a, and Valvulogenesis

A: As the embryo develops from 36 hpf to 58 hpf, KLF2a expression (darkened regions) becomes localized and condenses at the AVC (pink box, white arrow) and ventricular outlet (black arrow). **B-C:** Endothelial cells at the AVC in controls (WT), GATA2 MOs (low shear stress, reduced retrograde flow), and KLF2a MOs at 72 hpf. GATA2 and KLF2a MOs lack sufficient endocardial cushions for valve formation. **D:** Summary diagram of KLF2a function. Figure taken from Vermot, et al., 2009 [87].

Calculations of shear stress made by Vermot et al. were limited in accuracy because they failed to address the dynamic change in diameter of the AVC, only using an average estimated diameter in equation 2.4 [87]. Though retrograde flow was identified as necessary for KLF2a expression, the shear stresses associated with this flow necessary to induce expression remain unknown. Since retrograde flow only occurs during a specific period of the cardiac cycle, particular pumping mechanics conditions must be present to induce such a flow characteristic. Aim 1 of this thesis is focused on these mechanical influences driving the occurrence of retrograde flow through the AVC.

2.5 Methods for Analyzing Embryonic Heart Function

In order to quantify intracardiac flow parameters within the embryonic heart, imaging techniques must have the capacity to acquire the spatial and temporal resolution necessary to perform various computational flow-measurement methods. Due to the microscopic scale of the embryonic heart, standard medical imaging modalities such as ultrasound, MRI, and CT cannot attain such a scale of resolution [55]. One method used in chick embryos is optical coherence tomography (OCT), which consists of the emission of laser light and subsequent absorption of the reflected laser to develop a 2D image [16, 55]. OCT has a penetration depth of up to 2 mm and a resolution of approximately 10 μm , which is not ideal for measurements in the embryonic zebrafish, though is excellent for the chick embryo heart [16, 18, 95]. This low spatial resolution has prompted the development of cross-correlation algorithms that perform 3D-image restructuring of the embryonic heart in order to create finite element models which are then used to determine the elastic properties of the myocardial tissue [18, 95]. After the development of a laser gating method by Jenkins et al. in 2006, OCT images were able to be captured at a rate fast enough to perform microscopic particle image velocimetry (PIV) using red blood cells as tracer particles [96-98]. OCT has been used to study the velocity profile and strain rates at the ventricular outlet in the chick embryo heart, though the accuracy of this method is hindered by the imaging angle [16, 18, 95]. Velocity measurements can encounter significant noise if prone to interference from the heart wall, and blood cell velocities perpendicular to the OCT laser often go unmeasured [16].

Two other imaging modalities used to analyze embryonic heart function are confocal and bright-field microscopy. Confocal microscopy requires the use of fluorescence labeling to view internal features of a semi-transparent specimen by exciting fluorophores [41]. The focal plane thickness of confocal microscopy is very low, so it has been used to generate accurate 3-D reconstructions of the embryonic zebrafish heart [41, 45, 99]. Unfortunately, confocal microscopy lacks the temporal resolution necessary to analyze the intracardiac flow environment of the embryonic heart [41]. Bright-field microscopy on the other hand, does have that capability. Bright-field microscopy is the simplest imaging modality, though it requires the use of a transparent sample, so spatial resolution is simply dictated by the lighting intensity [55]. Fortunately, zebrafish embryos are transparent, making this imaging modality one of the most widely-used in embryonic zebrafish research. The focal plane thickness of bright-field microscopy is much greater than that of confocal microscopy, rendering it an inadequate method for 3-D image reconstruction; however unlike confocal microscopy, the temporal resolution is more than adequate for acquiring computational flow measurements of the intracardiac flow. Because of these advantages, experiments performed as part of the research comprising this thesis utilized bright-field microscopy.

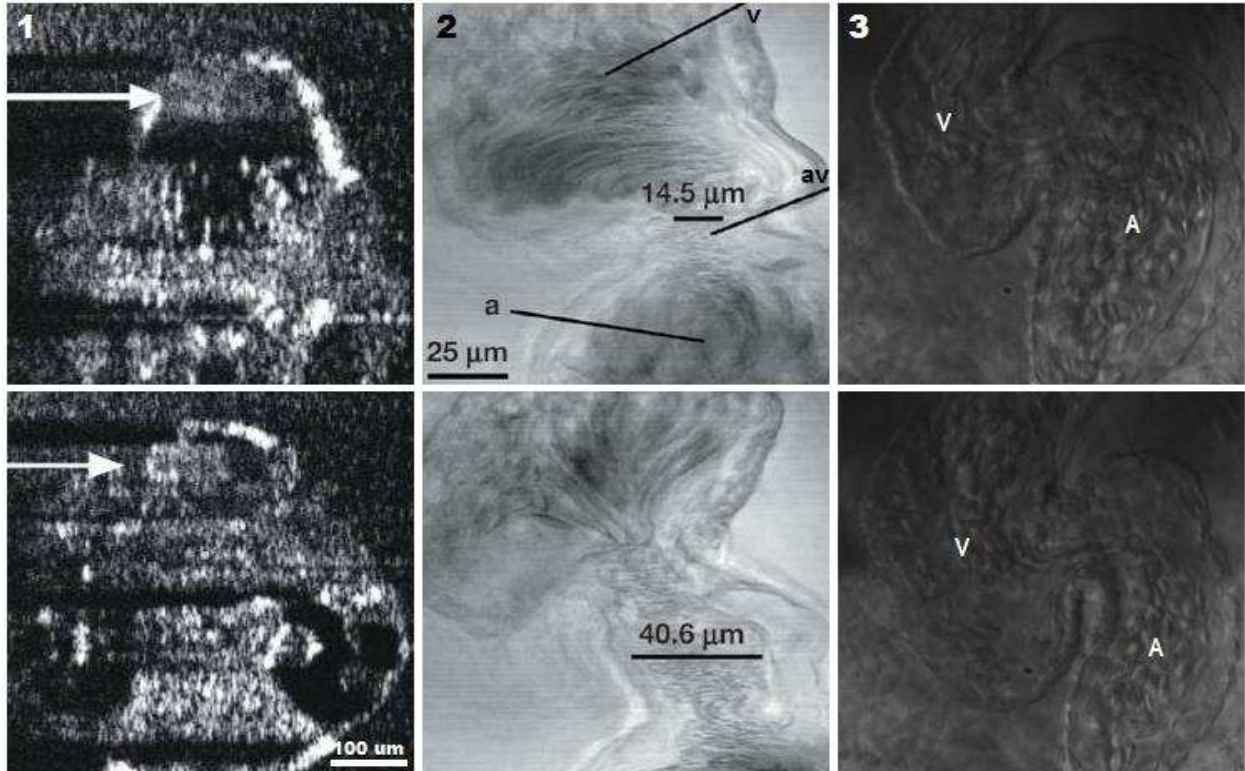


Figure 2.10: Embryonic Zebrafish Heart Imaged Under OCT (1), Confocal (2), and Bright-Field Microscopy (3)

1: Ventral-Cranial view of the zebrafish embryo under Optical Coherence Tomography at 72 hpf (top) and 120 hpf (bottom). Bright regions are created by blood flow and the white arrow points out the location of the heart. Image taken from Kagemann, et al., 2008 [100]. **2:** Embryonic heart under confocal microscopy at two cardiac cycle time points imaged at 108 hpf. “a” is the atrium, “v” is the ventricle, and “av” is the AVC. Image taken from Hove, et al., 2003 [9]. **3:** Embryonic heart under bright-field microscopy at two cardiac cycle time points imaged at 48 hpf. “A” is the atrium and “V” is the ventricle. Image taken using Olympus SZX12 bright-field stereomicroscope.

Particle Image Velocimetry (PIV) is a computational flow-measurement method that generates a velocity vector field from either 2D or 3D image sequences of a fluid consisting of tracer particles of an intensity contrasting that of the background. In experimental flow loops such as those used for studying turbulence, tracer particles are typically seeded into the fluid and intensity contrast is generated via illumination by a laser sheet [101]. When imaging the embryonic hearts of chicks and zebrafish however, red blood cells are used as tracer particles [101, 102]. Each frame of an image sequence of a fluid is divided into a grid, and a cross-correlation algorithm is

used to find the displacement of grid segments of similar particle orientation [103]. A velocity vector is then generated for each grid segment by dividing the time between frames by the grid segment displacement [103]. Velocities in between these grid segments are able to be calculated through interpolation, making PIV an excellent method for analyzing velocity profile. Methods utilizing PIV have been developed to calculate further parameters such as pressure, wall shear stress, and vorticity [9, 104, 105].

Because bright-field microscopy can be used to generate such high-resolution images of the embryonic zebrafish heart (Figure 2.10), it would seem that the intensity contrast of the individual red blood cells would make PIV an optimal method to analyze the flow mechanics. However, the scale of the red blood cells compared to the overall size of the heart is significantly large at the developmental stages analyzed in this thesis, thus the number of tracer particles in the overall fluid domain is relatively low. This is not ideal for PIV, as more accurate results are able to be attained with a greater number of smaller particles [106]. The size of the RBCs also affects how close they flow to the wall, so flows adjacent to the endocardium that only consist of plasma go undetected [106]. Because PIV measures velocity vectors by finding correlating pixel arrangements within grid segments, deformation in the RBCs caused by pressure changes can prevent the software from recognizing the RBC displacement, causing further error. Endothelial cells are also of the same size as red blood cells, so PIV software recognizes the walls of the heart as moving particles within the fluid [106]. When the endothelial cells move in the opposite direction of the RBCs, vortices are calculated

along the heart walls which severely disrupt intracardiac velocity calculations [55].

These limitations have not completely rendered PIV as an ineffective tool for analyzing intracardiac flows, but they have forced accurate analysis to be confined to only large-scale flow regions within the chambers [9, 104, 105].

Because PIV is such a powerful tool for visualizing the intracardiac flow environment, several attempts have been made to remove the heart walls from velocity calculations. The first attempt was through the development of a manual mask-drawing algorithm to eliminate the background signal, though PIV software would often still incorporate the dynamic background mask into velocity calculations [55]. A second method developed was to incorporate fluorescence labeling of red blood cells so that PIV software could be manipulated to only recognize fluorescent pixels [71, 107, 108]. Unfortunately, the fluorescence signal was unable to be captured accurately when imaging at the high frame rates needed to perform PIV calculations [107]. Lastly, the most promising method developed by Jamison et al. consists of the use of cardiac phase filtering to remove patterns that repeat over multiple cardiac cycles, leaving only the RBCs in the image [108]. Pixel patterns often do not correlate with that of subsequent cardiac cycles however because cardiomyocytes do not move in the exact same motion with each heartbeat, because heart rate often exhibits slight fluctuations over time, and because microscopes are often subject to some vibration [108]. This method is therefore still prone to significant error, though due to the prominence of ongoing research on the role of intracardiac flow mechanics in heart development, it is likely that a highly accurate method of PIV will be developed in the near future.

The flow-measurement method used for the research composing this thesis was inspired by an imaging modality referred to as 'laser scanning microscopy' (LSM). Rather than capture 2-D image sequences of an internal region of interest within the heart, LSM consists of the rapid reflection and absorption of a single laser linescan in one dimension [71]. The result is a spatiotemporal (ST) plot, or a kymograph, consisting of pixel data generated from the laser displayed along the vertical axis with respect to its change in time along the horizontal axis [71]. Laser scans can be captured as fast as 2,050 lines per second, making this method ideal for measuring blood cell velocity [71]. When the laser is directed parallel to the blood flow, red blood cells flowing along the beam produce streaks in the resultant spatiotemporal plot with an angle corresponding to the blood cell's velocity [71]. By combining this spatiotemporal velocity data with dynamic diameter-change data collected by orienting the laser perpendicular to the flow direction, accurate calculations of flowrate, stroke volume, and cardiac output have been made in the zebrafish dorsal aorta [71].

Though successful in the dorsal aorta, it is far more difficult to orient an LSM laser in-line with blood flow within the much less uniformly-shaped heart, especially at a region of selected interest [71]. Fortunately, because of the excellent spatial resolution of bright-field microscopy, the quantitative method of spatiotemporal analysis used for LSM scans has been applied to image sequences captured with a bright-field microscope. This allows for one-dimensional regions of interest, or "reference lines" to be manually selected from 2-D image sequences of the heart in order to generate ST plots. Computational software that utilizes spatiotemporal analysis of bright-field-

acquired, high-speed image sequences of the embryonic zebrafish heart was developed in 2013 by Johnson, et al., called the “Kymograph Analyzation Tool,” or KAT [109]. Due to the access to bright-field microscopy, KAT was determined to be the most accurate flow-measurement method available for measuring intracardiac flow as part of this research.

After image sequences of the embryonic heart are uploaded into KAT, they must undergo several preprocessing steps in order to enhance the accuracy of analysis. First, any vibration that may have caused shake in the image sequence is removed by shifting each frame such that the intensity of pixels in a static, manually-selected region align to the pixels of that region in the first frame. Fluctuations in lighting intensity could also severely affect velocity calculations, so intensity is then normalized across the image sequence using another manually-selected static region. This is done by calculating the average intensity of the pixels in that region so that all pixels in the rest of the image sequence are multiplied by a factor such that the pixels within that region retain the same average intensity [109]. Finally, since calculated parameters are averaged across cardiac cycles, the number of frames per cycle, or the heart rate, is calculated in order to generate a separate ST plot for each cycle. To do this, a reference line is selected over any region overlapping the heart. The variance between the pixels on the line in the first frame and each subsequent frame is then calculated and the frame with the least variance is determined [55]. The number of frames between the frame with least variance to the first is divided from the frame rate of the high-speed camera to determine the heart rate [55].

After preprocessing, spatiotemporal analysis of flow parameters begins with calculation of the lumen diameter by positioning a reference line perpendicular to the flow. Though the atrial inlet remains approximately static relative to the rest of the heart, most other regions of the heart exhibit considerable movement throughout each cardiac cycle. Because it is typically necessary to analyze regions other than the inlet, a feature of the KAT software allows for the location of the reference line to migrate with the movement of the heart throughout the cardiac cycle through the selection of “key frames” so that the position of the reference line between each key frame is interpolated. On the resultant ST plot, lumen diameter is then measured simply by manual selection of points along the inner edge of the endocardium as shown in Figure 2.11 [109].

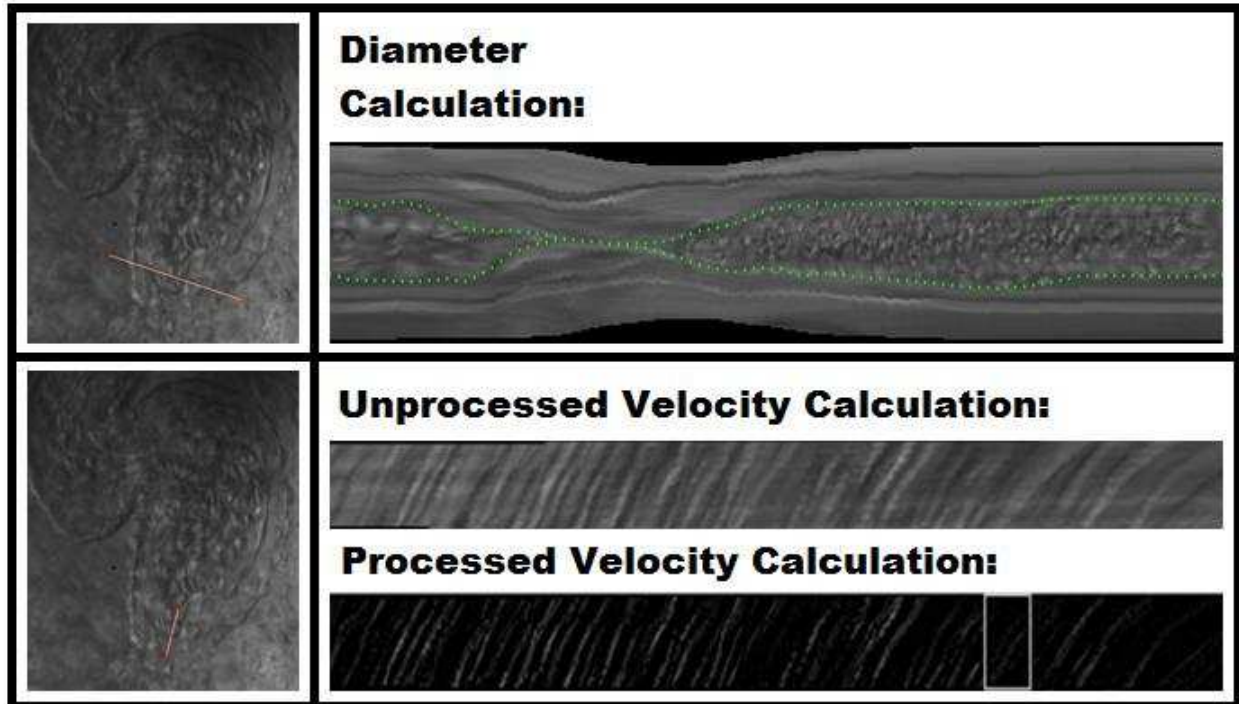


Figure 2.11: Example Spatiotemporal Plots of Diameter and Velocity Generated with KAT
Top: Location of reference line (left) and resultant spatiotemporal plot (right) to calculate lumen diameter at the atrial inlet of a 48 hpf WT zebrafish embryo. Manually-selected points on the endocardial edge are indicated in green. **Bottom:** Location of reference line (left) and resultant spatiotemporal plots (right) to calculate velocity from the streak angle. The sliding average of the pixel intensity was subtracted in the processed spatiotemporal plot. The white square in the processed plot indicates a bin undergoing radon transform.

To calculate velocity, a reference line is oriented parallel to the flow at the center of the flow profile to produce the unprocessed, streaked ST plot shown in Figure 2.11. In order to strengthen the signal-to-noise ratio of the streak angles corresponding to the RBC velocities, the sliding average of the pixel intensity of the image sequence is subtracted from the pixel intensity of each frame [109]. Therefore, all static portions of the image sequence are removed so that only the heart appears over a black background, resulting in the processed ST plot in Figure 2.11. Velocity measurements are made at 100 evenly-spaced time points along the cardiac cycle by measuring the streak angle across “bins” of 21-frame-width about each point. To calculate the streak angle, radon transforms were performed on each bin as illustrated in an example bin

shown in Figure 2.12 [109]. A radon transform is generated by projecting lines across the bin at angles ranging from 0° to 180° that generate a plot of the bin pixels along the projected line on the vertical axis versus the angle of projection along the horizontal axis (Figure 2.12) [109]. The variance is then calculated from the derivative of the radon transform, or more specifically, the pixel intensities along the line at each angle, and the angle with the greatest variance is used as the velocity streak angle [109]. A bin length of 21 was determined to result in minimum error when calculating the variance of these radon transforms [109].

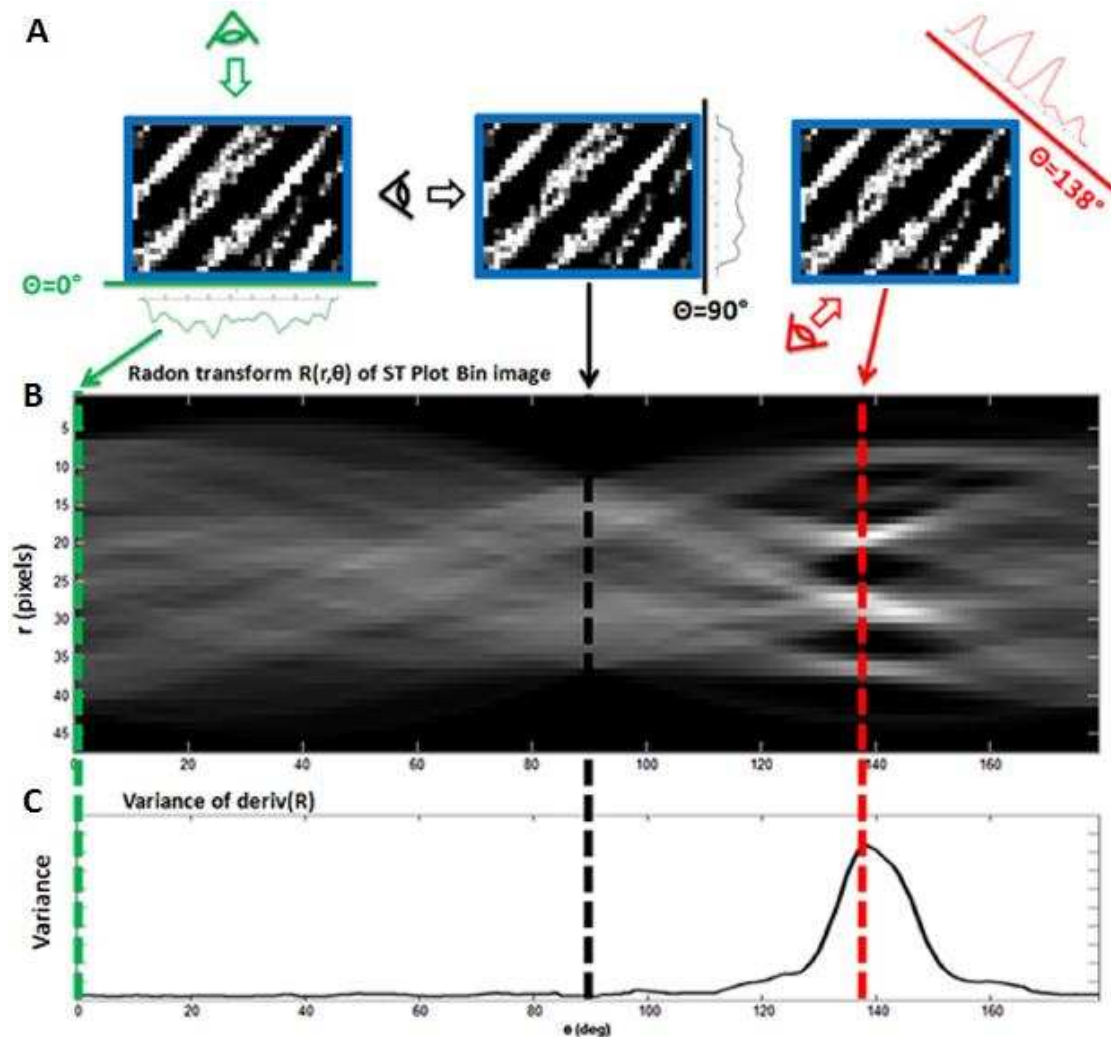


Figure 2.12: Velocity Calculation of an Example ST Plot Bin via Radon Transform

A: Orientation of example radon transform at projection angles of 0° , 90° , and 138° . **B:** The projected line at each angle ranging from 0° to 180° produces the radon transform plot shown. **C:** Plot of the variance of the derivative of the radon transform plot in (B) at each projection angle. A projection angle of 138° induces maximum variance, therefore the velocity of this bin is $v = \tan(138^\circ - 90^\circ) = 1.11$ pixels/frame. Figure taken from Johnson, et al., 2013 [109].

The set of 100 velocity measurements calculated across each cardiac cycle is averaged with the velocities of the subsequent cardiac cycles, and velocities outside of a variance threshold are then eliminated to remove noise [109]. By performing several velocity measurements across the velocity profile of the atrial inlet in several 48 hpf WTs, it was determined that the average velocity of the profile was equal to 74% of the center velocity [55]. The flow rate at each of the 100 time points is estimated by taking the

product of the average velocity and the lumen area, assuming that the area is a circular profile of the calculated lumen diameter, as shown in equation 2.5 where $Q(t)$ is flowrate, $v(t)$ is velocity, and $D(t)$ is diameter [109]:

$$Q(t) = 0.74 \frac{\pi}{4} v(t) D(t)^2 \quad (2.5)$$

Accumulated Volume is then calculated at each 100th of the cycle through the sum of the previous differential volumes, which are calculated by the product of the time corresponding to 1/100th of the cycle (Δt) and the instantaneous flow rate, $Q(t)$ as shown in equation 2.6, where V_{ac} is the accumulated volume [109]:

$$V_{ac}(t) = \sum_{i=0}^{i=t} Q(t)_i \Delta t \quad (2.6)$$

The accumulated volume at the end of the cardiac cycle corresponds to the stroke volume of the heart, and the cardiac output is equal to the product of the stroke volume and heart rate [109]. The retrograde flow fraction (RF), or the fraction of the volume of blood moving in reverse across the measured region of interest, is calculated as shown in equation 2.7 by taking the ratio of the sum of the negative differential volumes over the sum of the positive differential volumes [109]:

$$RF = \frac{\|\sum Q(t)_i \Delta t < 0\|}{\sum Q(t)_i \Delta t > 0} \quad (2.7)$$

Because blood is pushed ahead of the contractile wave in the embryonic zebrafish heart tube and atrium prior to valve formation, the instantaneous heart volume cannot accurately be used to predict stroke volume [45, 109]. Therefore, previous methods to calculate stroke volume and cardiac output, which measured the difference in end-diastolic and end-systolic volumes (EDV, ESV), would result in considerable underestimation in comparison to this method [109]. Spatiotemporal analysis with KAT is an exceedingly accurate method of measurement with respect to diameter and

velocity calculations. The error in diameter measurement is ± 1 pixel, so with a resolution ranging between 1024 - 1310 pixels/mm of the bright-field microscope used for the research in this thesis, the error in diameter ranges as low as ± 0.76 - ± 0.98 μm [109]. Error in streak angle is $\pm 1.5^\circ$, so with frame rates used in this research ranging between 1000 - 1500 frames/s, the error in velocity ranges between ± 0.020 - ± 0.038 mm/s [109].

Despite the advantages that spatiotemporal analysis holds in analyzing embryonic zebrafish intracardiac flow, several limitations inhibit its accuracy in quantifying flow rates and overall heart function parameters. The first and most obvious limitation lies in the assumption that the lumen area is of a circular profile, which drastically affects the accuracy of flowrate calculations [109]. Since an imaging modality that can accurately measure intracardiac flow in the embryonic zebrafish in three dimensions has yet to be developed, the circular-profile assumption has been used in the majority of previous research consisting of the measurement of similar parameters [9, 110]. Another prominent limitation arises from the assumption that mean velocity is equal to 74% of the centerline velocity. Because the velocity ratio of 0.74 was determined via multiple velocity measurements across a profile of the heart, and because velocities near the endocardial wall are unmeasurable due to a lack of RBC flow near the wall, the mean velocity may be underestimated. Also, since this velocity ratio was calculated at the atrial inlet in just a few wildtype zebrafish, this ratio could potentially not hold in other regions of the heart or in experimentally-treated embryos [109]. The purpose of Aim 2 of this thesis was to develop methodology to address these limitations by analyzing

image sequences of the embryonic zebrafish heart on multiple focal planes. By calculating lumen thicknesses and velocities of image sequences in each x-y plane at multiple z-axis locations, a more accurate estimation of lumen area and velocity profile is able to be obtained.

3. AIM 1

Since it has been illustrated that retrograde flow at the atrioventricular canal (AVC) in the post-tube/pre-valve embryonic heart is necessary for valvulogenesis [87], the purpose of aim 1 was to investigate the pumping mechanics influencing the induction of this retrograde flow. By non-invasively altering the cardiac preload in an experimental group of embryos, retrograde flow was able to be inhibited such that pumping mechanics could be compared with a control group of wildtype (WT) embryos exhibiting normal retrograde flow. Image sequences of the embryonic zebrafish heart were computationally analyzed using spatiotemporal analysis at both 48 and 55 hours post-fertilization (hpf), two key developmental time points in which the retrograde flow required for normal valve formation is prevalent [87]. Descriptive parameters of the pumping mechanics were then statistically compared between groups to determine those necessary for the presence of retrograde flow. Threshold ranges of two parameters: pressure associated with expansion and contraction of the atrium and ventricle, and resistance due to contractile closure of the atrium and AVC were determined to be mechanistically associated with the presence of retrograde flow.

3.1 Methods: Experimental Groups

Retrograde flow through the AVC begins at the onset of cardiac looping and continues until the formation of a valve around 105-111 hpf [34, 40, 41, 43]. During looping, retrograde flow is less prominent, so the analysis time point of 48 hpf was chosen

because it marks the end of cardiac looping, when the fraction of flow moving in retrograde becomes much more significant and occurs for a greater duration of the cardiac cycle [30, 34]. Though the retrograde flow involved in valve formation maintains prominence beyond 55 hpf, the second analysis time point of 55 hpf was chosen because it marks the beginning of obstruction of the heart under bright-field microscopy caused by the onset of pigmentation [22, 23]. These time points were also chosen for analysis to enable comparison with previous studies [40, 50, 87, 111].

After centrifugation was used to alter the cardiac preload in an experimental group of embryos, embryos with consistent retrograde flow were qualitatively separated from those without. Centrifugation has been shown to cause increase in variation in multiple flow parameters depending on the range of development time points that centrifugation is performed across [50]. Therefore, only embryos without noticeable morphological defects other than the absence of retrograde flow were used in the experimental group (N=17). Of the control group of wildtype embryos, approximately 5% either exhibited an absence of retrograde flow or did not experience retrograde flow to the extent of the other wildtypes. Because this study is only concerned with the influence of pumping mechanics on the presence of retrograde flow, rather than incidence of retrograde flow absence, these embryos were not included in the control group (N=20), and instead included in the experimental group. Thus, of the experimental group of embryos not experiencing retrograde flow, 8 were wildtype embryos exhibiting a sporadic phenotype, and 9 were centrifuged embryos.

3.2 Methods: Zebrafish Breeding and Embryo Preparation

Wildtype zebrafish (*Danio rerio*) were raised and bred in accordance with Westerfield [112] at a zebrafish handling facility located on the main campus of Colorado State University. Though these fish are considered to be wildtype, inbreeding has occurred for many generations. Fate-mapping experiments have been performed to determine the effect of zebrafish inbreeding in comparison to wild isolates, however it is unclear whether or not they have displayed any genetic variation that would affect the outcome of studies related to cardiac development [113]. In fact, the use of inbred strains is advantageous in that by reducing genetic variability of the parent fish, random variability in embryonic development of the offspring is minimized so that experimental outliers can be avoided [55].

Lighting in the zebrafish handling facility is automated to coordinate with the fish's circadian rhythm, therefore matings were set up prior to when lights turn on at 7:00 am, the time at which the fish are most susceptible to breed. To prepare for breeding, parent zebrafish were placed in breeding tanks the night prior with a transparent barrier used to separate the males and females overnight. In order to increase the probability of yielding a large number of eggs, two females were placed in each tank opposite one male. The barrier was removed to initiate breeding, and a sieve at the bottom of the breeding tank allowed the fertilized eggs to fall through, preventing from being consumed by the parent fish. Eggs were then collected after one hour of breeding to

limit the error in developmental stage determination to the timed age \pm 30 minutes post-fertilization.

After eggs were collected, they were stored in petri-dishes of E3 media, or embryo water, in an incubator at the standard temperature of 28°C [112]. Embryos removed from their chorion, or egg sac, require additional calcium for survival, so E3 media is used to provide this needed calcium, as well as solutions of various other nutrients to optimize the embryos' nutritional exposure [112]. A stock solution of 0.5 g/L of methylene blue trihydrate (Acros Organics) was diluted into the E3 media just after collection to act as an antimicrobial agent and prevent the invasion of paramecium. Embryo media was also replaced daily to ensure the prevention of mold growth inside the petri dish. Since some experimental embryos began centrifugation regimes at 24 hpf (\pm 0.5 hpf), all embryos were dechorionated (Figure 3.1) just prior to this time using tweezers and forceps by carefully peeling off the chorion in order to easily position the embryos at optimal viewing angles during imaging.

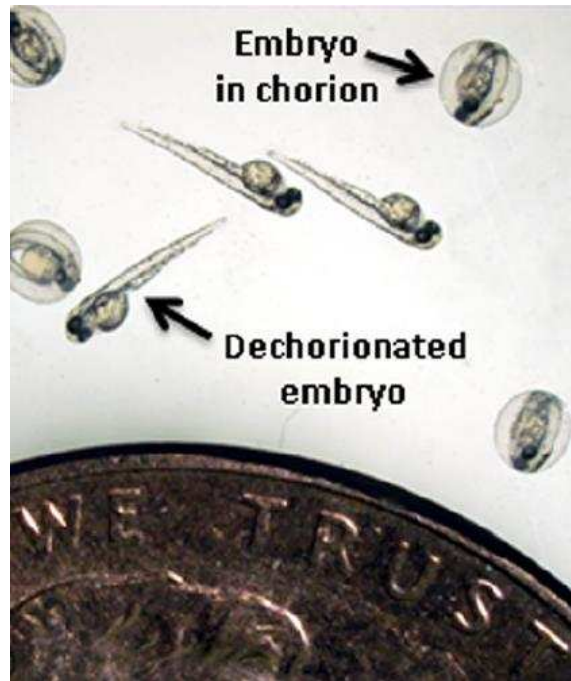


Figure 3.1: Scale of Chorionated and Dechorionated Zebrafish Embryos

Embryos at 55 hours post-fertilization (hpf) with and without a surrounding chorion are shown next to a U.S. penny for scale. Image taken from Johnson, et al., 2013 [109], 2015 [50].

3.3 Methods: Centrifugation

Since alternative methods to alter cardiac preload are invasive and/or result in various irreversible off-target developmental defects that would be detrimental to the experimental methodology of this study, centrifugation was chosen as the optimal option to alter the biomechanical environment in timed increments [9, 68-72]. Centrifugation causes a decrease in cardiac preload by effectively removing the amount of blood that returns to the heart by inducing “pooling” of the blood to the embryo’s extremities [55]. Embryos were centrifuged during one of four six-hour increments determined by key developmental stages defined by Kimmel as shown in Table 3.1 [30, 50]. Centrifuging at these different stages was determined by Johnson, et al. to have a significantly different and more variable effect on heart morphology and function depending on the

period of induced centrifugation [50]. By centrifuging at earlier stages (24-36 hpf), longer-lasting changes in heart morphology and function result, whereas centrifuging at later stages (36-48 hpf) results in temporary alterations from which embryos often recover by 55 hpf [50]. The effect of centrifugation on retrograde flow has not been studied at the AVC, though it has been studied at the atrial inlet. In Johnson's study, regardless of the period of centrifugation used, a group of embryos will experience an increase in the variance of observed retrograde flow fraction (RF) at the atrial inlet, rather than an overall increase or decrease in RF [50]. Therefore, in the current study, all four increments of centrifugation were further evaluated and only embryos exhibiting an absence of observable retrograde flow at the AVC were selected for analysis as part of the experimentally 'affected' group. Though it was visibly apparent based on the number of red blood cells (RBCs) flowing across the AVC that these experimental embryos lacked retrograde flow, it is highly probable however that there still remains a small amount of plasma flowing in reverse each cardiac cycle. The number of embryos centrifuged during each developmental stage is shown in Table 3.1:

Table 3.1: Periods of Centrifugation and Associated Developmental Stages

Group #	Time Period	Developmental Stage	Amount
1	24 hpf → 30 hpf	Onset of Circulation	3
2	30 hpf → 36 hpf	Early Cardiac Looping	3
3	36 hpf → 42 hpf	Mid-Cardiac Looping	2
4	42 hpf → 48 hpf	Late Cardiac Looping	1

To load embryos into the centrifuge, they were first inserted into small pieces of polymer tubing (Cole-Parmer, FEP tubing) of 1/32" inner diameter by attaching the tubing to the

end of a pipette. This tubing size was selected because it is just greater than the average width of the embryo so that any movement during the process of centrifuging would be limited. The small polymer tube containing the embryo was then inserted into a larger centrifuge tube partially filled with low-melting agarose gel (Sigma Aldrich, Type VII-A, A0701) to prevent the embryo from falling out of the inner tube as shown in Figure 3.2. The agarose gel was prepared by mixing a solution of 1.5% agarose powder heated in 20-second increments until suspended particles were no longer visible and then allowed to cool and increase in viscosity. The polymer tube was then inserted into the centrifuge tube such that the embryo was oriented head-down to ensure that the effect of blood pooling would be consistent across embryos. The tubes were then filled with E3 media so that the embryo was kept alive and subject to the same nutritional environment throughout the process.

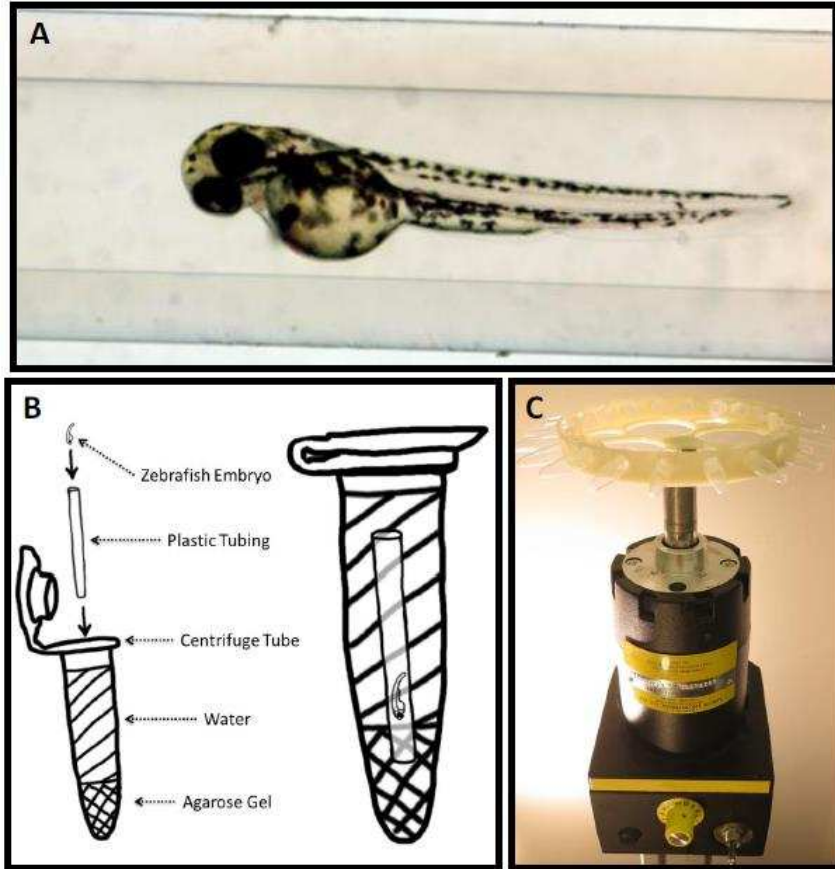


Figure 3.2: Centrifugation Experimental Setup

A: Embryos were inserted into plastic polymer FEP tubing of 1/32" inner diameter via pipette to constrain the embryo. **B:** Plastic polymer tubes were then inserted into a larger centrifuge tube partially-filled with low-melting agarose gel to prevent the embryo from sliding out of the inner tube. **C:** 24 centrifuge tubes were then loaded onto the centrifuge apparatus such that embryo's heads were oriented radially-outward. Images taken from Johnson, et al., 2015 [50].

The centrifuge tubes were affixed to a centrifuge apparatus consisting of a variable-speed motor that holds up to 24 embryos (Figure 3.2). The rotation speed was set to 15 Hz based on estimates that indicated that this frequency would reduce the cardiac preload by an order of magnitude of the pressure within the heart, without causing rupture or severe damage to embryo bodies [50]. Because of the high rotation speed, it was crucial to fully fill the centrifuge tubes, otherwise pressure differentials caused by centrifugally-induced loading would greatly exceed this order of magnitude and crush the embryo. The standard incubation temperature of 28 °C was also maintained during

centrifugation, except when inserting and removing embryos into and from the centrifuge tubes. Upon removal of the embryos from the centrifuge tubes, they were incubated in E3 media-filled petri dishes until reaching the selected time point of analysis.

For the most part, the width of the embryo was not exactly equal that of the inner diameter of the polymer tubing (Figure 3.2), often resulting in a stunted head-trunk angle due to compression of the embryo against the agarose gel [55]. This change in overall embryo morphology is apparent at 48 hpf, though embryos always recovered by 55 hpf; therefore, this deformation likely has little influence on sustained cardiac defects [55]. Despite this, the orientation of the embryo within the tube exhibits variability that could inhibit the consistency of blood pooling between embryos. Johnson et al. performed experiments to evaluate the effect of orienting the embryo in various intra-tubular positions by applying fluorescent markers to red blood cells to evaluate the intensity associated with regions of pooling [55]. Fortunately, neither fluorescence intensity nor location of intensity within the embryo exhibited any significant difference between orientations, indicating that blood pooling occurs to the same extent regardless of slight variation in positioning of the embryo within the polymer tube [55].

3.4 Methods: Imaging the Embryonic Heart

The viewing angle of the zebrafish embryonic heart used in previous research has nearly always been with the ventral-side directly upward, such that the atrium appears

in front of the ventricle and slightly to the left side of the embryo at the stages analyzed in this study [9, 34, 50, 87, 109]. When floating in the E3 media, embryos tended to twitch and rotate to a position of dorsal side-up, making it difficult to image them directly from the petri dish. Some embryos naturally moved into the desired position, in which imaging from the petri dish would occur, however for most embryos, it was not possible to orient them this way. Therefore, a second, smaller petri dish was prepared with a layer of melted agarose gel allowed to settle and solidify so that it would create a smooth surface along the bottom of the petri dish. A dissecting razor was then used to create two slices in the top of the agarose gel at approximately 45° angles such that they would converge at a depth into the gel not greater than the width of an embryo. Since the dorsal side of the embryo is much narrower than the bulbous yolk sac of the ventral side, the dorsal side falls into the created divot easily so that the embryo can be held in place with its ventral side up. After the divots in the agarose were made, a thin layer of E3 media was poured over the agarose and embryos were transferred from the larger petri dish via a pipette. Forceps were then used to gently guide an individual embryo into the divot. This technique of positioning the embryo has benefits over methods used in previous studies that would position the embryos within warm, melted agarose, which could slightly increase heart rate [55].

As stated in the literature review, bright-field microscopy was selected as the most applicable imaging modality to this research because of its excellent spatial resolution when applied to the transparent zebrafish embryo. Image sequences were captured using a Photron FASTCAM SA3 high-speed camera taken at 1,500 frames per second.

The camera was mounted atop an Olympus SZX12 bright-field stereomicroscope with an SZX-AL20X lens attachment that would yield spatial resolutions ranging between 1,050 to 1,310 pixels per millimeter. Software to control the high-speed camera was manipulated from a nearby computer in which the contrast and brightness were adjusted so that the interior edge of the endocardium and exterior edge of the myocardium would be clearly visible from the atrial inlet to past the center of the ventricle throughout the duration of a cardiac cycle. After recording at least six cardiac cycles, embryos were transferred via pipette into a Tricaine solution to be anesthetized. After at least 5 minutes of anesthetization, embryos were euthanized in a bleach solution according to protocol as required by the Institutional Animal Care and Use Committee (IACUC).

3.5 Estimating Pressure due to Chamber Contraction and Expansion

It was hypothesized that retrograde flow across the AVC was caused by a pressure differential generated due to expansion and contraction of the atrium and ventricle, respectively, therefore a method to derive these pressures from parameters measured through spatiotelemetric analysis was calculated. First, to calculate the pressure due to expansion or contraction of just one chamber, an equation for the balance of momentum in a differential cylindrical control volume of blood within the chamber (Figure 3.3) is established as shown:

$$\begin{aligned} & \rho \frac{\partial u}{\partial t} r \Delta r \Delta \theta \Delta z + \rho u r_{z+\Delta z} \Delta r \Delta \theta - \rho u r_z \Delta r \Delta \theta \\ = & -P r_{z+\Delta z} \Delta r \Delta \theta + P r_z \Delta r \Delta \theta + r \tau_{zz}|_{z+\Delta z} \Delta r \Delta \theta - r \tau_{zz}|_z \Delta r \Delta \theta - \tau_{rz} r \Delta \theta \Delta z \end{aligned} \quad (3.1)$$

where P is pressure, ρ is density, u is velocity, and τ is shear stress. This equation is then derived accordingly to account for the total chamber diameter:

$$\begin{aligned} \rho \frac{\partial u}{\partial t} r \Delta r + \rho \frac{ur_{z+\Delta z} - ur_z}{\Delta z} u \Delta r &= \frac{Pr_z - Pr_{z+\Delta z}}{\Delta z} \Delta r + \frac{r\tau_{zz}|_{z+\Delta z} - r\tau_{zz}|_z}{\Delta z} \Delta r - \tau_{rz} r \\ \rho \frac{\partial u}{\partial t} R^2 + \rho \frac{\partial u^2 R^2}{\partial z} &= -\frac{\partial PR^2}{\partial z} + \frac{\partial \tau_{zz} R^2}{\partial z} - 2\tau_{rz} R \\ \frac{\partial u}{\partial t} D^2 + \rho \frac{\partial u^2 D^2}{\partial z} &= -\frac{\partial PD^2}{\partial z} + \mu \frac{\partial^2 u D^2}{\partial z^2} - 4\tau_{rz} D \\ \frac{\partial u}{\partial t} D^2 + \rho \frac{\partial u^2 D^2}{\partial z} &= -\frac{\partial PD^2}{\partial z} + \mu \frac{\partial^2 u D^2}{\partial z^2} - \mu C u \end{aligned} \quad (3.2)$$

where D is diameter, R is radius, μ is viscosity, and C is a constant accounting for the wall shear stress.

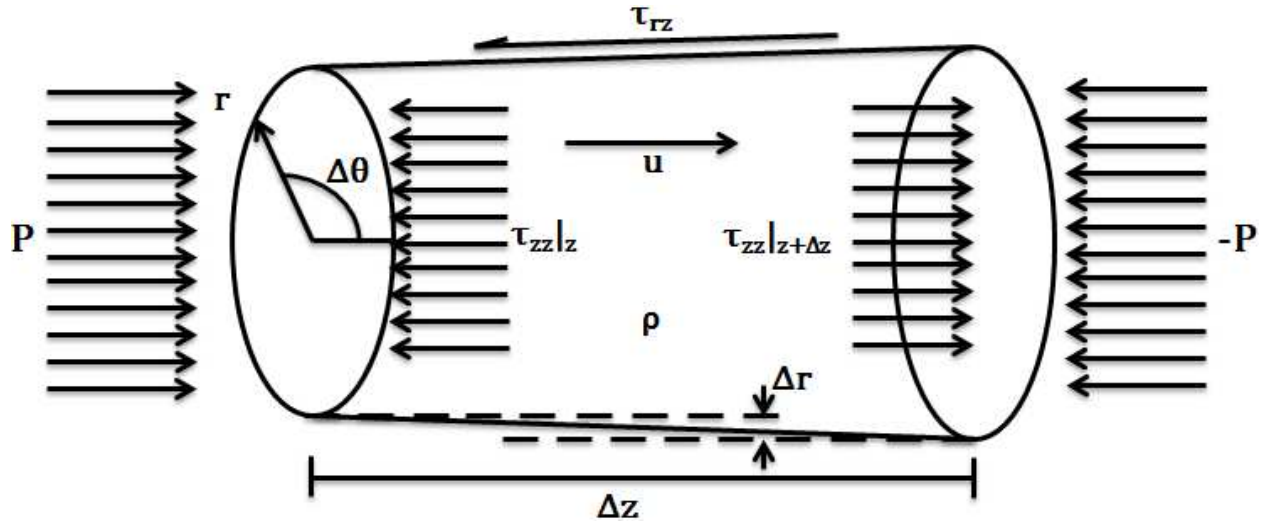


Figure 3.3: Differential Cylindrical Control Volume to Estimate Pressures due to Chamber Diameter Change

A diagram outlining the differential cylindrical control volume within the heart used to estimate pressure associated with expansion and contraction of the atrium and ventricle through the balance of mass and momentum is shown, where P is pressure, u is velocity, ρ is density, and τ is shear stress.

As stated in the literature review, the scale of the embryonic heart is miniscule enough such that Reynold's and Womersley numbers can be considered to be negligible.

Through rearrangement of variables, it can be seen that the terms on the left side of

equation 3.2 are proportional to these characteristic parameters, and therefore can be canceled out of the equation, resulting in the simplified balance of momentum equation 3.3:

$$\frac{\partial PD^2}{\partial z} = \mu \frac{\partial^2 u D^2}{\partial z^2} - \mu C u \quad (3.3)$$

Next, an equation for the balance of mass is established in the same differential cylindrical control volume within the chamber, assuming uniform blood density:

$$\frac{\partial}{\partial t} (r \Delta r \Delta \theta \Delta z) + r u_{z+\Delta z} \Delta r \Delta \theta - r u_z \Delta r \Delta \theta = 0 \quad (3.4)$$

This equation, also referred to as the continuity equation, is then simplified in order to reduce the equation to that consisting of similar variables as that of equation 3.3, resulting in the simplified continuity equation 3.5:

$$\begin{aligned} \frac{r u_{z+\Delta z} - r u_z}{\Delta z} \Delta r + \frac{\partial}{\partial t} r \Delta r &= 0 \\ \frac{\partial u D^2}{\partial z} &= - \frac{\partial D^2}{\partial t} \end{aligned} \quad (3.5)$$

Finally, equation 3.5 is substituted into equation 3.3 to yield:

$$\frac{\partial PD^2}{\partial z} = -\mu \frac{\partial}{\partial z} \left(\frac{\partial D^2}{\partial t} \right) - \mu C u \quad (3.6)$$

Since the hypothesis of this study requires analysis only of pressures associated with expansion and contraction of the chamber, only pressures generated through change in volume, as opposed to velocity changes are analyzed. Diametrical contraction or expansion alone can dictate the sign of the pressure gradient that regulates flow direction; therefore a simplified model is used in which the wall shear stress term is ignored. Upon integration along z , the desired resultant pressure is obtained as a function of diameter, a parameter that is easily measureable through spatiotemporal analysis:

$$PD^2 = -\mu \frac{\partial D^2}{\partial t}$$

$$P = -2 \frac{\mu}{D} \frac{\partial D}{\partial t} \quad (3.7)$$

In previous zebrafish intracardiac flow studies, the viscosity, μ , has either been ignored by measuring shear rate, or has been simply guessed based on a range of viscosities observed in humans, and with considerable variability [8, 9, 107]. Therefore, a unitless pressure was calculated by non-dimensionalizing the pressure to the viscosity and heart rate in cycles per second:

$$P_{norm} = \frac{P}{\mu * HR} = -\frac{2}{D} \frac{\partial D}{\partial \bar{t}} \quad (3.8)$$

where HR is heart rate and $\partial \bar{t}$ is the time differential normalized to the heart rate. By calculating the difference in these pressures between the atrium and ventricle across a cardiac cycle, the pressure difference across the AVC was able to be analyzed and compared with the presence of retrograde flow.

3.6 Methods: Diameter Measurement

The diameters and rates of diameter change used in equation 3.8 to estimate pressure due to expansion and contraction of the atrium and ventricle were measured through spatiotemporal analysis using KAT (kymograph analyzation tool) software described in the literature review section 2.5. The reference lines to measure the diameter were positioned at the center of the chambers (Figure 3.4) and adjusted so as to line up with the same endocardial cells throughout the cardiac cycle. Manual selection of diameter points in the resultant spatiotemporal (ST) plot was performed at 40 evenly-spaced time

points across the cardiac cycle, and sixty additional intermediate points were calculated through interpolation. To calculate the rate of diameter change at each time-point, the difference between the diameter values before and after that time-point were calculated and divided by the time corresponding to 3% of the cardiac cycle.

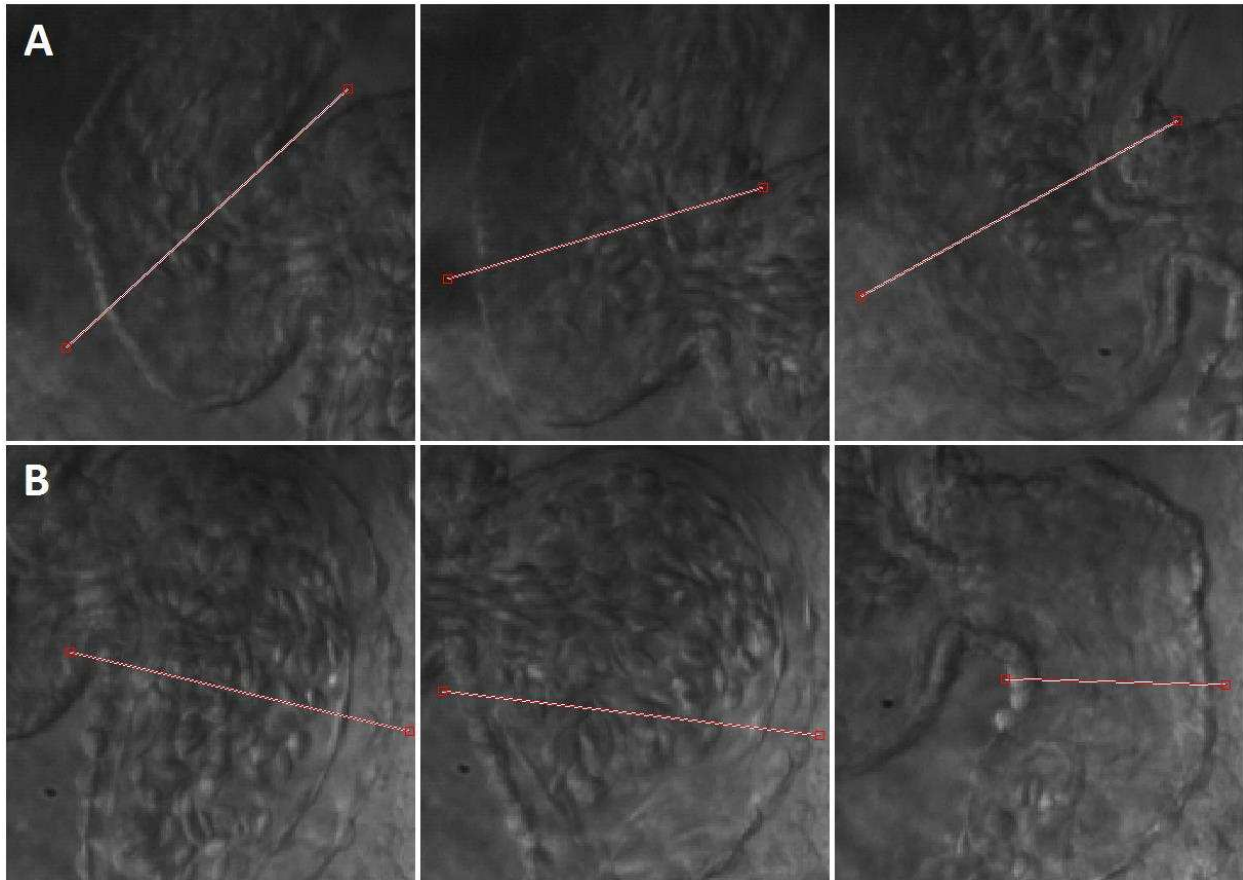


Figure 3.4: Locations of Diameter Measurement in the Atrium and Ventricle

A: Positioning of the reference line used to generate spatiotemporal (ST) plots for diameter measurement of the center of the ventricle is shown at three time points throughout the cardiac cycle in an example embryo at 48 hpf. **B:** Positioning of the reference line at the center of the atrium is shown at three time points throughout the cardiac cycle.

When comparing diameter change across a cardiac cycle between embryos with retrograde flow across the AVC (control group) and without (experimental group), it was necessary to normalize the chamber diameters to account for variation in the size of the

heart associated with allometric scaling to the overall size of the embryo. Johnson et al. compared stroke volume in wildtype embryos, which is understood to be directly related to body surface area, to various scaling parameters within the heart and found that the maximum diameter of the atrial inlet was significantly correlated with the overall size of the embryo ($p < 0.001$) [50]. Therefore, diameters of the atrium and ventricle were normalized to their maximum atrial inlet diameter. The diameters were also normalized across their cardiac cycle and aligned so that the end of atrial diastole would occur at 51% of the cycle. This was done in order to calculate ensemble averages across both the control and experimental group embryos.

3.7 Methods: Length of Closure Measurement

In addition to examining pressure differences associated with expansion of the atrium and contraction of the ventricle as a driving mechanism of retrograde flow, resistance was examined as an inhibiting mechanism. Though contacting endothelial cells within the atrium and AVC during systole often appear to be fully closed, red blood cells moving in retrograde can often be seen flowing behind the contacting endothelium in a separate focal plane. Therefore, a thin channel is likely always present during atrial systole. Assuming this channel is of a circular profile, the resistance in this channel could be calculated through the simplified Hagen-Poiseuille equation:

$$R = L \frac{128\mu}{\pi D^4} \quad (3.9)$$

where R is resistance, L is the closure length (described further below), D is the diameter of the channel formed by contraction, and μ is the viscosity. Because red

blood cells can be seen in a separate focal plane from the contacting endothelia, this channel is however not of a circular profile. In the embryonic chick, OCT has been used to show that contraction of the heart tube induces eccentric deformation of the endocardium due to uneven distribution of the cardiac jelly (Figure 3.5A), which is most likely also the case in the zebrafish heart tube as well as the atrium at the stages examined here [114]. Therefore, calculation of the resistance in the contracted channel via measurement of diameter would exacerbate error by a power of four based on equation 3.5, so only the length of closure, L , was measured as a proportional parameter.

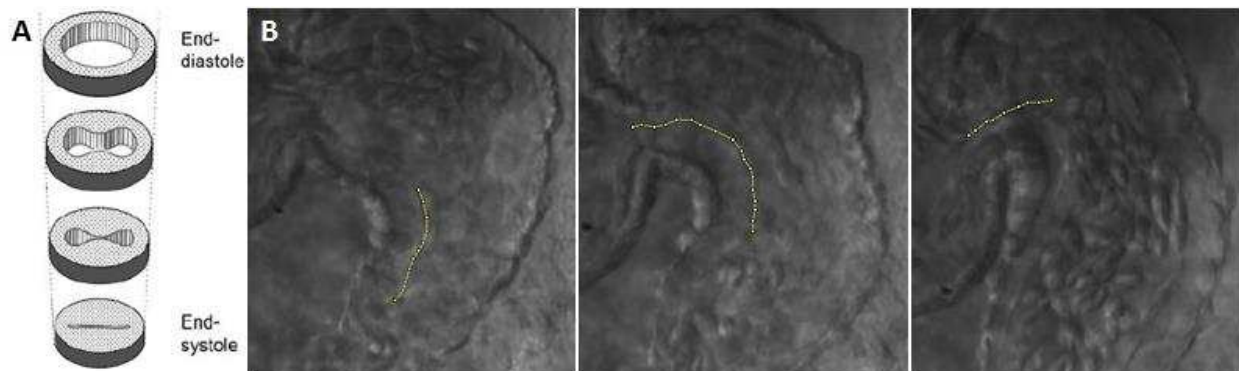


Figure 3.5: Eccentric Deformation and Contractile Closure Length Measurement in the Atrium/AVC
A: A cross-sectional diagram illustrating eccentric deformation of the chick endocardial heart tube during systole resulting in a non-circular flow profile. Figure taken from Manner, et al. 2008 [114]. **B:** Images of the zebrafish embryo atrium and AVC are shown at three time points during the cardiac cycle with segmented lines drawn along the length of endothelial closure. Segmented lines were drawn and measured using imageJ software.

The closure length was measured manually by drawing segmented lines along the contacting endocardial lining of the atrium and AVC as shown in Figure 3.5B. These segmented lines were drawn using imageJ software that would output the number of pixels along the line and then convert according to the spatial resolution of the image sequence. Closure lengths were measured at twelve evenly-spaced time points across

a cardiac cycle and curve-fitting was implemented to estimate intermediate closure length values. The closure lengths were then normalized to the maximum atrial inlet diameter as with the chamber diameters in order to account for allometric scaling.

3.8 Results: Pressure due to Chamber Expansion/Contraction

Since negative pressure differentials drive flow in the forward (positive) direction, retrograde flow was hypothesized to be induced by a positive pressure difference across the AVC. Therefore, atrial pressures calculated through the simplified model would be negative, and ventricular pressures would be positive. Based on equation 3.7/3.8, retrograde flow was thus expected to occur in conjunction with expanding atrial diameters, and contracting ventricular diameters. Of the control group embryos, the percentage exhibiting retrograde flow, atrial expansion, and ventricular contraction were therefore compared across the cardiac cycle at 5%-increments as shown in Figure 3.6A. Between 60% and 80% of the cardiac cycle, no embryos experience retrograde flow, though atrial expansion and ventricular contraction are initiated at approximately 75%. As the atrium and ventricle continue to expand and contract, less than half of the embryos experience retrograde flow between 85% and 15% of the cycle. A majority of embryos then exhibit retrograde flow from 15% to 45% of the cycle, which coincides with a majority of embryos experiencing atrial expansion and ventricular contraction.

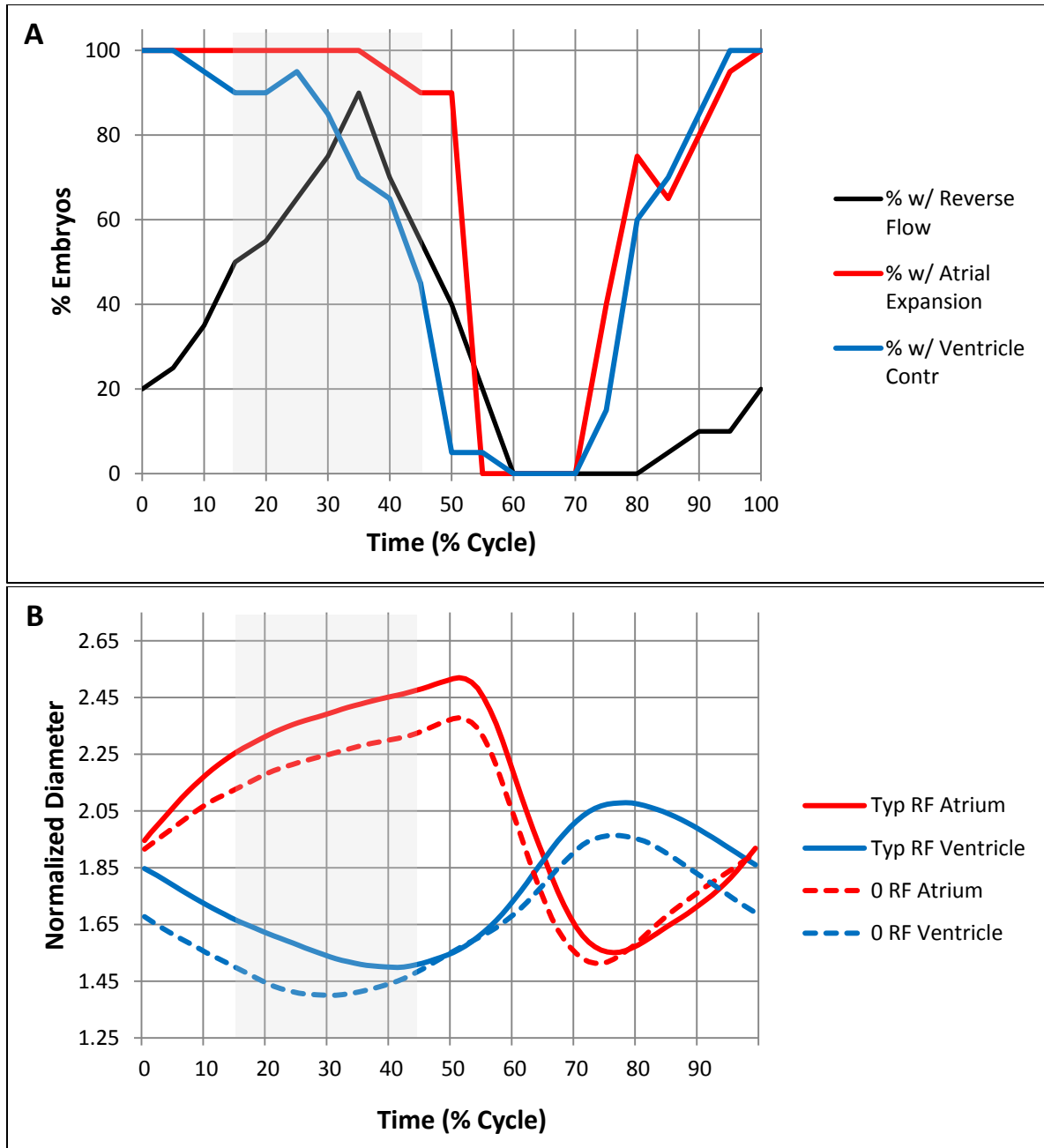


Figure 3.6: Timing of Retrograde Flow at the AVC Relative to Chamber Expansion and Contraction

A: The fraction of control group embryos with typical retrograde flow across the AVC at 5% increments of the cardiac cycle is shown (black) as well as the fraction of embryos undergoing atrial expansion (red) and ventricular contraction (blue). **B:** The ensemble average of the normalized diameter at the center of the atrium (red) and ventricle (blue) is shown in embryos with typical retrograde flow (Typ RF, solid line) (N=20) and without retrograde flow (0 RF, dotted line) (N=17) with respect to the percentage of time across a cardiac cycle. Diameters were normalized to the maximum diameter of the atrial inlet. The cardiac cycle is temporally aligned between figures A and B and with that of figures 3.7 and 3.8. Shaded regions correspond to the period in which over 50% of control-group embryos experience retrograde flow along the AVC.

The difference in some important characteristics of the pumping mechanics between embryos with and without retrograde flow can be observed through the ensemble averages of the normalized chamber diameters (Figure 3.6B). Though it appears that the atria of embryos in the experimental group exhibit a lower overall normalized diameter, the variance in these diameters is great enough that a significant difference in atrial pumping between the control and experimental group cannot be interpreted from this data alone. This difference in overall normalized diameters appears to be the case for the ventricle as well. The timing in the cardiac cycle of the ventricular diameter change reveals a major difference between embryos with and without retrograde flow, however. In the control group, the average ventricular diameter reaches a minimum, or the end of systole, at approximately 10% of the cardiac cycle prior to the point at which the atrial diameter reaches its maximum, or the end of diastole. In contrast, ventricular diameters of embryos in the experimental group reach the end of systole at least 20% of the cardiac cycle prior to the end of atrial diastole. They then expand to nearly 50% of their maximum diameter by the time the atrium reaches the end of diastole, whereas in the control group, the ventricle has just begun to expand at the end of atrial diastole. This timing between ventricular end-systole and atrial end-diastole supports differences in ventricular pumping mechanics as the primary factor affecting the incidence of retrograde flow.

Upon estimating pressures from the rates of diameter change across the cardiac cycle as described in equation 3.8, further contrast in pumping mechanics between the experimental and control groups are revealed (Figure 3.7A). The error in the ensemble

average of the normalized atrium diameters is too great to notice any major differences, however more apparent distinctions emerge from the pressure results in which the error is more constrained. Between approximately 95% and 12% of the cardiac cycle, it is now evident that the atrium exhibits faster expansion in embryos with retrograde flow than in embryos without. When a majority of embryos experience retrograde flow (15%-45%) however, pressures due to atrial expansion are relatively the same between both groups. Starting at about 20% of the cardiac cycle, the rate of contraction of the ventricle becomes much greater in embryos with retrograde flow than in those without. This difference is maintained beyond the point in which a majority of control-group embryos experience retrograde flow, though the pressure difference between both chambers in embryos lacking retrograde flow reaches zero prior to 35% of the cycle. In contrast, this does not occur in control group embryos with normal retrograde flow until about just before 45% of the cardiac cycle.

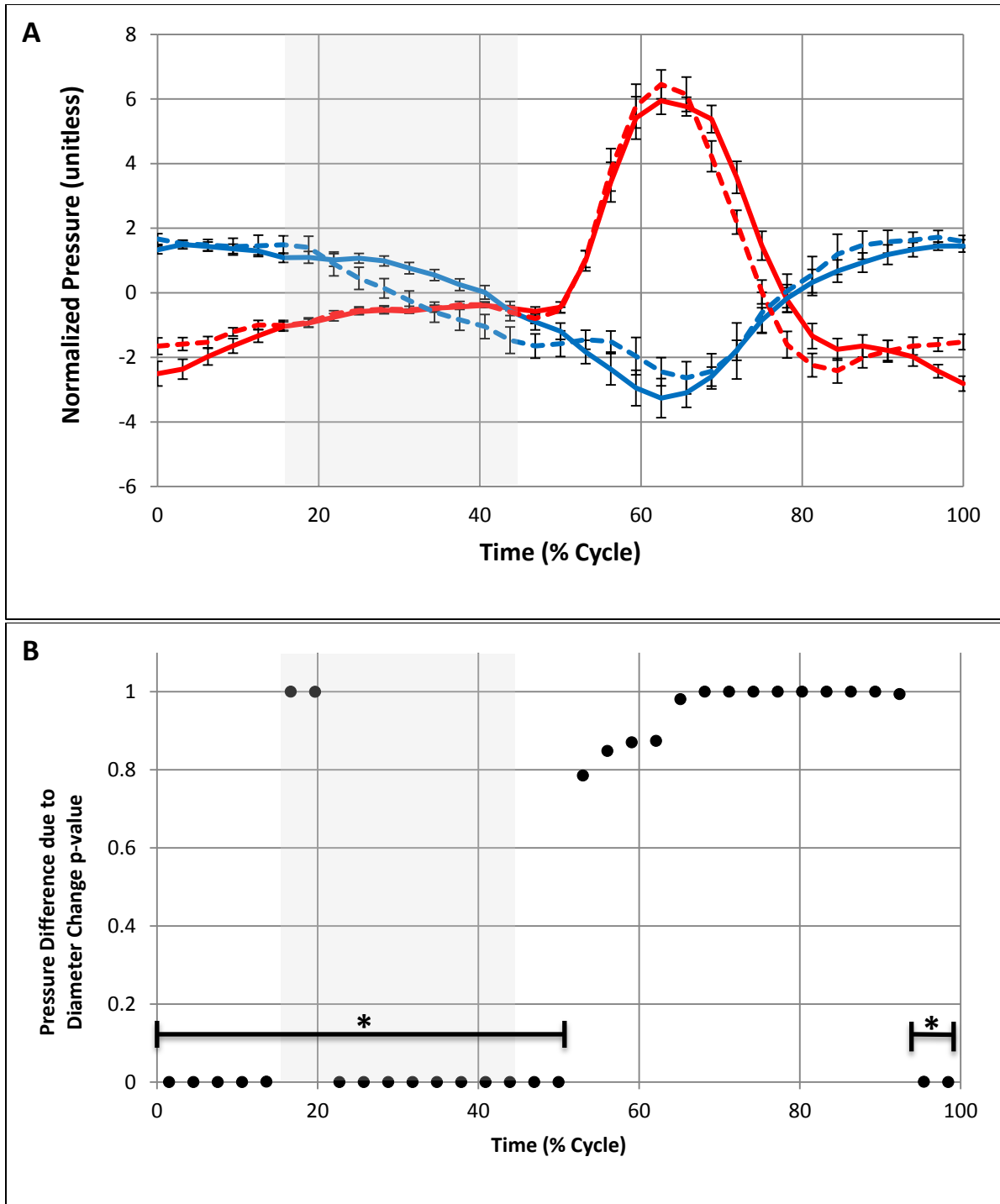


Figure 3.7: Pressure Differences due to Chamber Expansion and Contraction in Relation to Retrograde Flow

A: The ensemble average normalized pressures associated with expansion (negative pressures) and contraction (positive pressures) of the atrium (red) and ventricle (blue) were calculated from the change in diameters of the center of the chambers in embryos with typical retrograde flow (solid line) (N=20), and without retrograde flow (dotted line) (N=17). Pressures were normalized to the viscosity and heart rate according to equation 3.8. Error bars indicate standard error. **B:** P-values are shown across a cardiac cycle to test statistical significance of the pressure difference due to diameter change between the center of the atrium and ventricle. An asterisk indicates the region of the cycle that this pressure is significantly

less in embryos lacking retrograde flow compared to control group embryos. (* $p < 0.01$) Shaded regions correspond to the period in which over 50% of control-group embryos experience retrograde flow along the AVC.

Statistical significance was tested between the control and experimental groups by calculating p-values at 3%-intervals across the cardiac cycle to determine at which periods that the pressure difference in embryos lacking retrograde flow was significantly less than that of control group embryos with normal retrograde flow (Figure 3.7B). Except for a brief period between 16-20% of the cardiac cycle, the pressure difference was significantly less ($p < 0.01$) in embryos lacking retrograde flow during nearly the entire period of the cardiac cycle that retrograde flow occurred in all control-group embryos (90% to 50%). Between 25% and 40% of the cycle, pressure differences were also extremely significantly different ($p < 0.0001$). Though the pressure difference is much less in embryos without retrograde flow, it still does not fully explain why control-group embryos typically do not experience retrograde flow prior to 15% of the cardiac cycle. Further analysis of resistance is required to determine whether it functions as a mechanism to constrain retrograde flow to the period of the cardiac cycle observed.

3.9 Results: Length of Endothelial Closure

Since resistance to flow can increase with endothelial closure based on equation 3.9, closure length was calculated along the atrium and AVC to investigate the extent to which it was restricting retrograde flow when retrograde flow-driving pressures were present. The ensemble averages of the endothelial length of closure across embryos with and without retrograde flow are provided in Figure 3.8A.

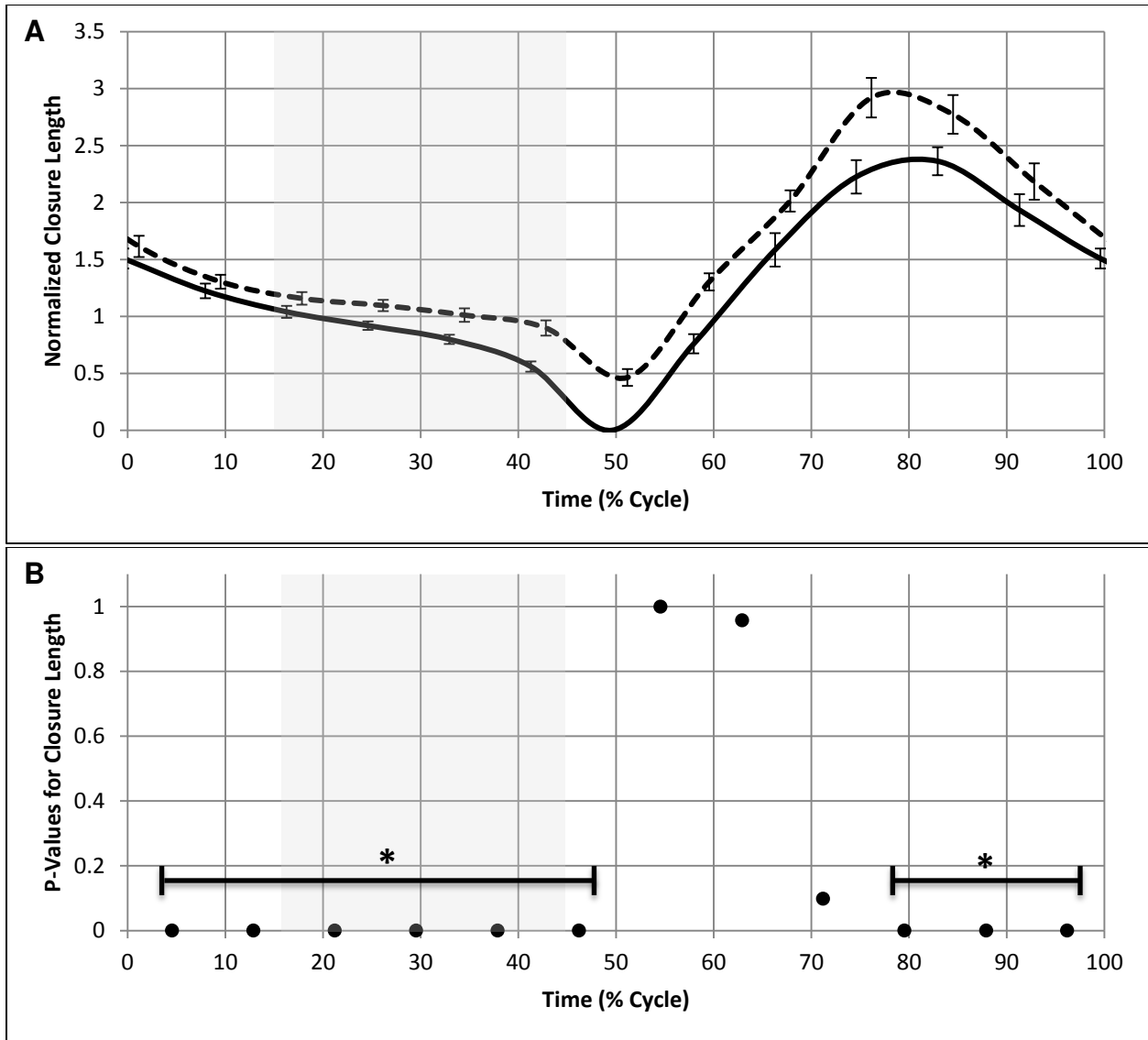


Figure 3.8: Atrial and AVC Endothelial Closure Length in Relation to Retrograde Flow

A: The ensemble average of the closure lengths (normalized to the max atrial inlet diameter) along the atrium and AVC are shown in control-group embryos with retrograde flow (solid line) and experimental-group embryos lacking retrograde flow (dotted line) with respect to time across a cardiac cycle. Error bars indicate standard error. **B:** P-values are shown across a cardiac cycle to test statistical significance of the length of endothelial closure along the atrium and AVC. An asterisk indicates the region of the cycle that closure lengths are significantly greater in embryos lacking retrograde flow compared to control group embryos ($* p < 0.0001$). Shaded regions correspond to the period of the cardiac cycle in which over 50% of control-group embryos experience retrograde flow along the AVC.

All control-group embryos with normal retrograde flow would undergo a point of zero closure at around 50% of the cardiac cycle, just after the end of atrial diastole and just before ejection into the ventricle. This point of zero closure, that is, when no contact

was observed between endothelial cells, would occur after the AVC would begin to open, but just prior to when the atrial inlet would begin to contract. Of experimental group embryos lacking retrograde flow, nearly all exhibited no period of zero-closure at any point in the cardiac cycle. At least some portion of the atrium would thus remain closed at all times in these embryos, as the atrial inlet would typically always contract either just as the AVC would open, or well before.

Over the period of the cardiac cycle in which a majority of control-group embryos experienced retrograde flow (15%-45%), it can be seen that the difference in closure lengths between embryos with and without retrograde flow exhibits a nearly five-fold increase as the cardiac cycle moves from 15% to 45% (Figure 3.8A). Though this difference is less than that seen when the closure lengths are increasing during ejection, the variability in closure lengths, especially that of control group embryos with retrograde flow, is particularly low during this 15%-45% period. Statistical significance was thus analyzed along the cardiac cycle to determine at which points that the closure length of embryos lacking retrograde flow was significantly greater than that of control-group embryos with normal retrograde flow (Figure 3.8B). Except for during ejection between approximately 55% and 72% of the cardiac cycle, embryos lacking retrograde flow exhibited significantly greater ($p < 0.0001$) closure lengths than control-group embryos. Therefore, these embryos lacking retrograde flow also experienced significantly greater resistance to retrograde flow than control-group embryos at all times that retrograde was observed to occur. These data support resistance due to

endothelial closure as a mechanism contributing to the absence of retrograde flow in the experimental group.

3.10 Discussion

The combination of the two mechanisms: 1. Pressure difference due to simultaneous atrial expansion and ventricular contraction, and 2. Resistance due to contractile closure of the atrium and AVC, together provide an adequate explanation of the mechanisms driving the occurrence of retrograde flow. The adverse pressure drop across the AVC that appears to drive retrograde flow is influenced by both the timing and rate of ventricular contraction relative to atrial expansion. The influence of the timing between ventricular end-systole and atrial end-diastole on retrograde flow was clarified by the difference in diameter change between embryos with and without retrograde flow seen in Figure 3.6B. In embryos without retrograde flow, there appeared to be a significant discordance between chambers, as ventricles would reach end-systole far earlier than control-group embryos with retrograde flow. This discordance in ventricular contraction also occurred during the period of the cardiac cycle that retrograde flow was potentially most likely to occur (15%-45% of the cycle). Because ventricular expansion induces a negative pressure, by initiating ventricular diastole earlier in the cardiac cycle with respect to atrial end-diastole, the retrograde-flow driving pressure in experimental group embryos generated by atrial expansion during this period (30%-45% of the cycle) is inhibited.

The estimated pressures, which were calculated through the rates of chamber diameter change, reveal details of the pumping mechanics that further support the generation of retrograde flow. When retrograde flow is most likely to occur (15%-45% of the cycle), rates and associated pressures of ventricular contraction are far greater in control-group embryos with retrograde flow than those without. When embryos lacking retrograde flow reach end-systole at approximately 30% of the cardiac cycle, control-group embryos with retrograde flow continue to exhibit significant pressures associated with ventricular contraction. The pressure due to ventricular expansion reaches the same pressure as due to atrial expansion at about 35% of the cardiac cycle in experimental embryos without retrograde flow, so the difference in pressure across the AVC becomes negative and reverses to a forward-flow driving pressure at this point. This is in stark contrast to control-group embryos, in which ventricular pressures would not reach the end of systole and begin relaxation until around 40% of the cardiac cycle. Pressure differences between chambers across the AVC would also not become negative until 45% of the cycle in embryos with retrograde flow, the point at which retrograde flow ceases in a majority of those embryos. Though this cross-over in the control group embryos occurred after the point at which the ventricle began to expand, the pressure due to passive atrial expansion continued to be great enough that a pressure difference sufficient to drive retrograde flow was maintained.

If the primary reason for the presence of retrograde flow was due to the pressure difference across the AVC caused by simultaneous atrial expansion and ventricular contraction, then one would expect to see retrograde flow occur in a majority of

embryos when they were also experiencing atrial expansion and ventricular contraction. The fact that this was did not occur (Figure 3.6A) suggested that this pressure difference must have not been the only factor influencing the occurrence of retrograde flow. Since retrograde flow often initiates during a period when the AVC appears closed from the focal plane in-view, analysis of resistance due to endothelial closure indicates this mechanism was able to sufficiently explain the restriction of retrograde flow to only the period of the cardiac cycle observed (15%-45% in a majority of control-group embryos). Prior to ejection, the atrial inlet begins to contract, and the length of contractile closure increases along the atrium in a direction from the inlet to the AVC such that blood is forced out of the chamber and into the ventricle. Upon conclusion of ejection, the length of closure in which endocardial cells are in contact progresses up towards the top of the atrium and AVC such that blood enters the atrium and initiates diastole. As the atrium expands, the length of closure decreases and becomes restricted to the AVC, limiting the resistance to the pressure difference generated across the AVC due to atrial expansion and ventricular contraction. Once the length of closure is small enough, its associated resistance can no longer prevent the flow of blood from the ventricle to the atrium, allowing retrograde flow to occur.

A diagram illustrating the effect of the combination of the two defining parameters of pressure and resistance that regulate retrograde flow across the AVC is shown in Figure 3.9. The model in this diagram simplifies the system driving retrograde flow by implementing two 'balloons' filled with some general Newtonian fluid to represent the chambers and a variable resistor to represent resistance due to endothelial closure. As

the balloon representing the ventricle expands, and the atrium contracts, fluid inside is forced from the contracting balloon towards the expanding balloon. When this first occurs, the resistance of the variable resistor is great enough however that the flow is prevented from crossing into the expanding balloon. Once the resistance of the variable resistor decreases past a certain threshold representative of the decreasing length of endothelial closure, the fluid is able to pass into the expanding balloon, thus driving retrograde flow.

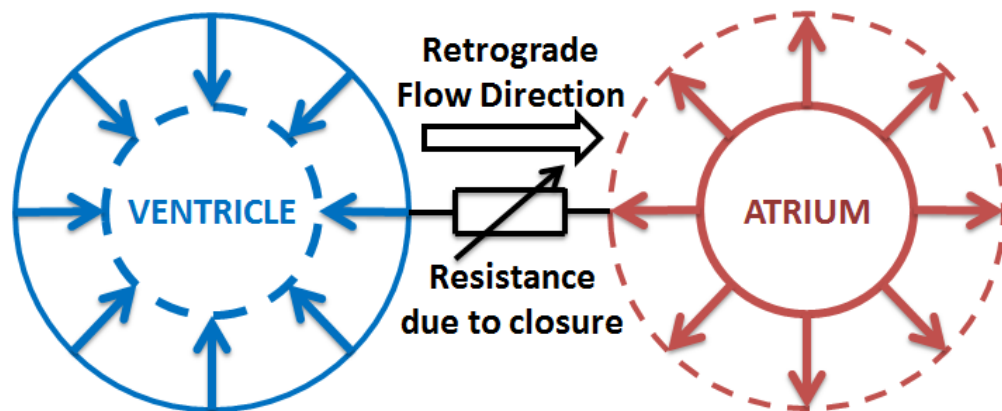


Figure 3.9: Model Illustrating the Dual Mechanisms Regulating Retrograde Flow

Two 'balloons' are used to represent the dynamic volume change due to expansion and contraction of the atrium and ventricle, respectively. A variable resistor is used to represent the change in resistance due to changing length of endothelial closure along the atrium and AVC.

If retrograde flow were to occur in an example embryo based on the ensemble average when a majority of embryos experienced retrograde flow (15%-45% of the cycle), then at 15%, retrograde flow would initiate at a non-dimensionalized pressure difference across the AVC of 2.23 and when the length of endothelial closure decreases past a factor of 1.07 of the maximum atrial inlet diameter. At 45% of the cardiac cycle, retrograde flow would be terminated by a pressure difference across the AVC of zero, when pressures become negative and drive flow forward. The length of endothelial

closure would have decreased to a factor of 0.31 of the maximum atrial inlet diameter at this point. Using an estimated viscosity of 4 cP (based on an average estimated in previous embryonic zebrafish intracardiac flow studies) [8, 9, 107], the pressure at the time retrograde flow would be initiated would translate to 0.152 μmHg .

One major limitation of this study was that flow could not be measured at the AVC, which would have allowed for calculation of resistance due to closure and shear stress on the endocardial cushions. Because the AVC is constricted for a majority of the cardiac cycle, the diameter on the focal plane in-view is only on the order of a few pixels and thus too low to measure accurately. Since spatiotemporal analysis of the flow through KAT software assumes a circular profile, which squares diameter values, and because resistance calculations are derived from the diameter to the fourth power, flow rates at the AVC cannot be measured with any accuracy. The use of proportional parameters such as the length of endothelial closure provide an understanding of the mechanisms influencing retrograde flow, though to determine exact values of parameters necessary to generate retrograde flow would require further analysis using more resolute imaging modalities.

The circular-profile assumption of the KAT software also limits the accuracy of pressure calculations in the chambers. A cylindrical control volume within the heart was used to estimate chamber volume due to its compatibility with the circular-profile assumption of the software. Not only are the chambers not of a circular profile, which will be further discussed in Aim 2 of this thesis, but during contraction, the chambers likely undergo

eccentric deformation to an even more irregular profile (Figure 3.5). Additionally, the chambers do not exhibit constant diameter in the axial direction, so the center diameter used does not provide an accurate representation of the overall change in volume. By integrating diameter measurements from image sequences of the same heart on multiple focal planes, and at multiple points along the heart, a more accurate chamber volume could be calculated. Though it would be beneficial to calculate highly accurate, non-normalized pressures and resistances, this study was only focused on explaining the mechanistic influence driving retrograde flow, which was achieved through the proportional parameters used. Therefore, although the development of a method to integrate spatiotemporal analysis results on multiple focal planes is the focus of the study in Aim 2, it was determined that implementation of that method in Aim 1 would only increase the time of analysis without affecting the overall outcome of the study.

Though cyclic retrograde flow in the AVC has been shown to be a regulator of valve formation, until now, the mechanical environment within the embryonic heart driving the occurrence of this retrograde flow had not been understood. In zebrafish embryos without retrograde flow, significant difference in pressure across the AVC compared with WT embryos during the period of the cardiac cycle that a majority experienced retrograde flow was shown to be due to a decreased ventricular pressure, which is typically the result of a reduced cardiac preload. Because pumping efficiency increases as the heart develops, it is likely that this cyclic retrograde flow observed in zebrafish also occurs between chambers in human embryos as the chambers contract and ultimately expand with increasing pressure throughout cardiogenesis. If this presence

of retrograde flow does in fact exist in human embryos and is involved in valve formation similarly to in zebrafish, then this methodology applied to analysis of pressures due to expansion and contraction of the chambers as well as endothelial closure length can be applied to human embryos as a diagnostic tool to both identify and provide intervention for congenital valve defects, however only once imaging modalities are developed that can acquire image sequences of the heart *in-utero* with adequate spatial and temporal resolution.

4. AIM 2

Although spatiotemporal analysis of high-speed image sequences of the embryonic zebrafish heart has proved to be one of the most efficient currently available methods for analyzing intracardiac flow, its accuracy is limited due to the fact that image sequences are only captured in two dimensions. As described in the literature review, analysis on only one focal plane that bisects the middle of the heart must therefore be performed based on two key assumptions: The first is that the flowrate is calculated based on the assumption that the intracardiac flow profile is circular with a diameter as observed on the focal plane in-view. The second limitation is that velocities are only calculated at the center of the profile, which relies on the assumption that the mean velocity is always proportional to the center velocity by the same constant parameter at all locations within the heart. When analyzing the change of various flow parameters and their relationship to observed developmental changes of the heart, this method is typically sufficient enough to explain those relationships. However, if attempting to determine exact threshold values of specific flow parameters necessary for certain development-related conditions to occur, this method would fail to provide the necessary accuracy.

Since both of these limitations arise because analysis of flow is performed on only one focal plane, these limitations were able to be accounted for by performing spatiotemporal analysis on multiple focal planes. The purpose of Aim 2 was to develop methodology that would address these limitations by integrating spatiotemporal data

from multiple focal planes into more accurate intracardiac flow data. A complementary algorithm to the KAT (Kymograph Analyzation Tool) software developed by Johnson, et al. [109] as described in the literature review was created in MATLAB (Mathworks, Inc.) that uses diameter and velocity data on each focal plane to recalculate both the profile area, and velocity profile across a cardiac cycle. By recalculating these two parameters, flow rate as well as additional parameters descriptive of cardiac function were able to be estimated with reduced error in comparison to the previous methodology.

4.1 Methods: Zebrafish Embryo Preparation and Imaging

Wildtype zebrafish were raised and bred in accordance with Westerfield [112] in the same manner as described in the methods section for Aim 1 (Chapter 3.2). Embryos were stored at the same temperature and in the same solution of E3 media with methylene blue trihydrate (0.5 g/L) until imaging was performed at 55 hpf. In order to maximize the number of focal planes used for analysis of intracardiac flow, the time point of 55 hpf was used because at this point, the heart has increased to its maximum girth prior to the onset of pigmentation. Since an experimental group with altered cardiac preload was not required as in Aim 1, dechoriation was not conducted on the embryos until imaging at 55 hpf. Between 48 hpf and 55 hpf, most embryos “hatch” from their chorion independently, so it was however only necessary for a few embryos to be dechorionated. Dechoriation was again performed manually using forceps and tweezers.

In order to capture high-speed image sequences of the heart on multiple focal planes, each image sequence was taken independently of one another in consecutive order using the same Photron FASTCAM SA3 high-speed camera used in Aim 1. In Aim 1 as well as in previous studies [50], a frame rate of 1500 frames per second was used, which would result in download times ranging between 15 and 20 minutes. Since embryos needed to remain perfectly still throughout the process of capturing each image sequence, this download time was far too long, as embryos would twitch before being able to capture image sequences on only the first few focal planes. Fortunately, this temporal resolution was far greater than necessary in order to accurately calculate velocity based on radon transforms across ST plots as described in the literature review. By reducing the frame rate to 1000 frames per second, the download time was reduced to just over 2 minutes, which allowed for all embryos to be analyzed on each focal plane before any movement would occur. This frame rate was determined to be the best option for analysis, as it could have been further reduced before any detrimental effect on the velocity calculations would be induced. Also, the same Olympus SZX12 bright-field stereomicroscope was used as in Aim 1, though with a spatial resolution of 1,024 pixels per millimeter.

One primary method to determine the accuracy of any computational flow-measurement software is through calculating the difference in downstream flowrate. Due to the cyclical nature of intracardiac flow, the difference in downstream stroke volume (ΔSV) was thus compared between the multi-focal plane and circular-profile methods of spatiotemporal analysis:

$$\Delta SV = \|SV_{Atrium} - SV_{Ventricle}\| \quad (4.1)$$

In order to capture flow using the most focal planes possible to increase accuracy, downstream stroke volume was evaluated by analyzing flow at both the center of the atrium and center of the ventricle. Because of this, it was critical that the center focal plane of analysis would bisect approximately through the center of both chambers. Since the standard orientation of ventral-side up results in the atrium becoming positioned on a higher focal plane than the ventricle, this orientation could not be used for this analysis. In order for both chambers to be aligned on the same focal plane, the embryo had to be slightly rotated by less than 45° counter-clockwise about the anteroposterior axis as shown in Figure 4.1:

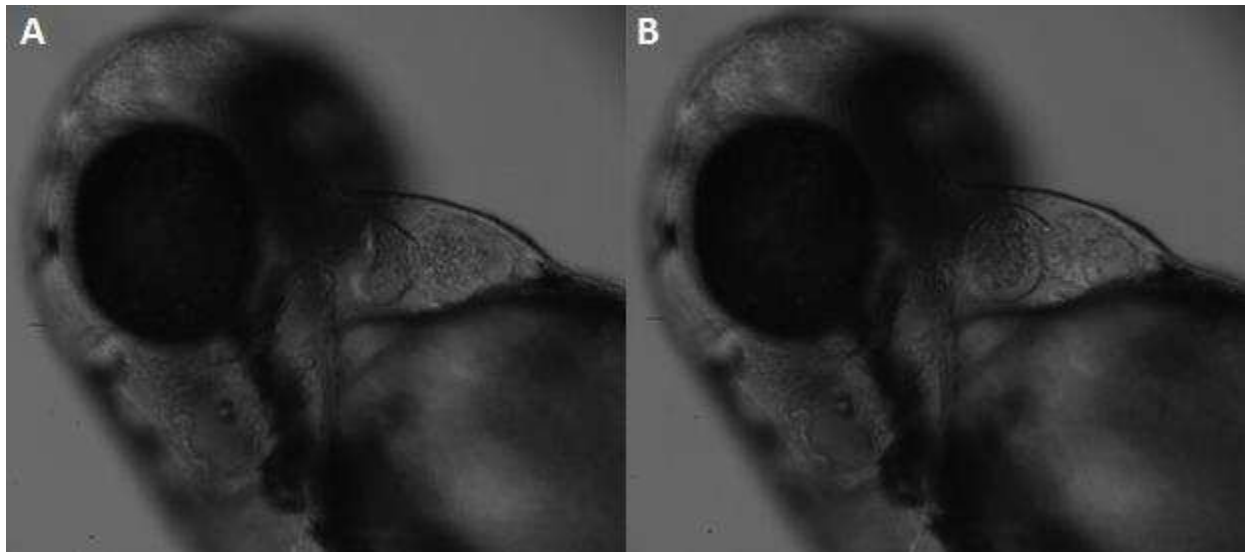


Figure 4.1: Orientation of Embryo for Approximate Alignment of Chambers

An example WT embryo imaged at 55 hpf positioned in the orientation necessary such that both the center of the atrium and ventricle lie in approximately the same focal plane. The embryo has been slightly rotated from the ventral side-up orientation by less than 45° counter-clockwise about the anteroposterior axis. Movement was inhibited through mild anesthetization using a 40 µg/mL solution of Tricaine methanesulfonate. **A:** at atrial end-diastole/ventricular end-systole, **B:** at atrial end-systole/ventricular end-diastole

Though it may have been possible to create a divot in a layer of agarose gel in order to position the embryo in the orientation described (Figure 4.1) as was the case in Aim 1, it would have been extremely difficult to shape the divot manually using a dissecting razor such that the embryo could easily fall into this orientation. Therefore, small drops of melted agarose gel were injected at various locations on the petri dish and allowed to solidify such that the embryo could lean up against the drops after being positioned next to them ventral side-up. Despite the induced reduction in image sequence download speed by lowering the frame rate, embryos would still have the tendency to twitch in this position before sequences on each focal plane could be acquired. To account for this, mild anesthetization was induced by applying a 40 $\mu\text{g}/\text{mL}$ solution of Tricaine methanesulfonate to the E3 media in which the embryos were stored in and imaged from. Because the purpose of this aim was merely to develop methodology to more accurately quantify heart function, rather than analyze heart function in wildtypes, it was not necessary for the embryos to maintain a normal heart rate [72], and thus the use of Tricaine was permissible. This orientation was only necessary in order to calculate the difference in stroke volume analyzed between the atrium and ventricle, so future use of this methodology would not be limited to using Tricaine to position the embryos, and could be used for analysis at many various orientations.

Based on the size of the chambers and depth of the focal plane, it was determined that the optimal number of focal planes used for analysis across the heart was 5. The average chamber diameter measured from image sequences of 42 wildtype embryos saved from previous studies was approximately 112 μm , which translated to a distance

of 18.7 μm between focal planes when evenly-spaced across the heart. If fewer focal planes of analysis were to be used, the estimated area of the intracardiac flow profile and velocity profile would be less accurate, however with a greater number of focal planes, the focal planes would begin to overlap due to the thickness of each plane. By placing a slide with a transparent slit at a known angle under the microscope, this focal plane thickness, or the focal depth, was calculated by analyzing the light intensity across the slit (Figure 4.2A). Using the widest aperture setting available on the Olympus bright-field microscope, which exhibited the thinnest focal depth, the focal depth from the intensity distribution along the slit was conservatively approximated to be about 36 μm (Figure 4.2B). At the edges of the focal plane, the features of the heart become distorted, therefore by using 18 μm as the distance between focal planes, the focal depth of each plane becomes distorted just at the position of the adjacent focal planes of analysis. If more focal planes were used, the focal depths would overlap, and features of the heart between different focal planes would become more difficult to distinguish, rendering diameter measurements on each plane more prone to human error.

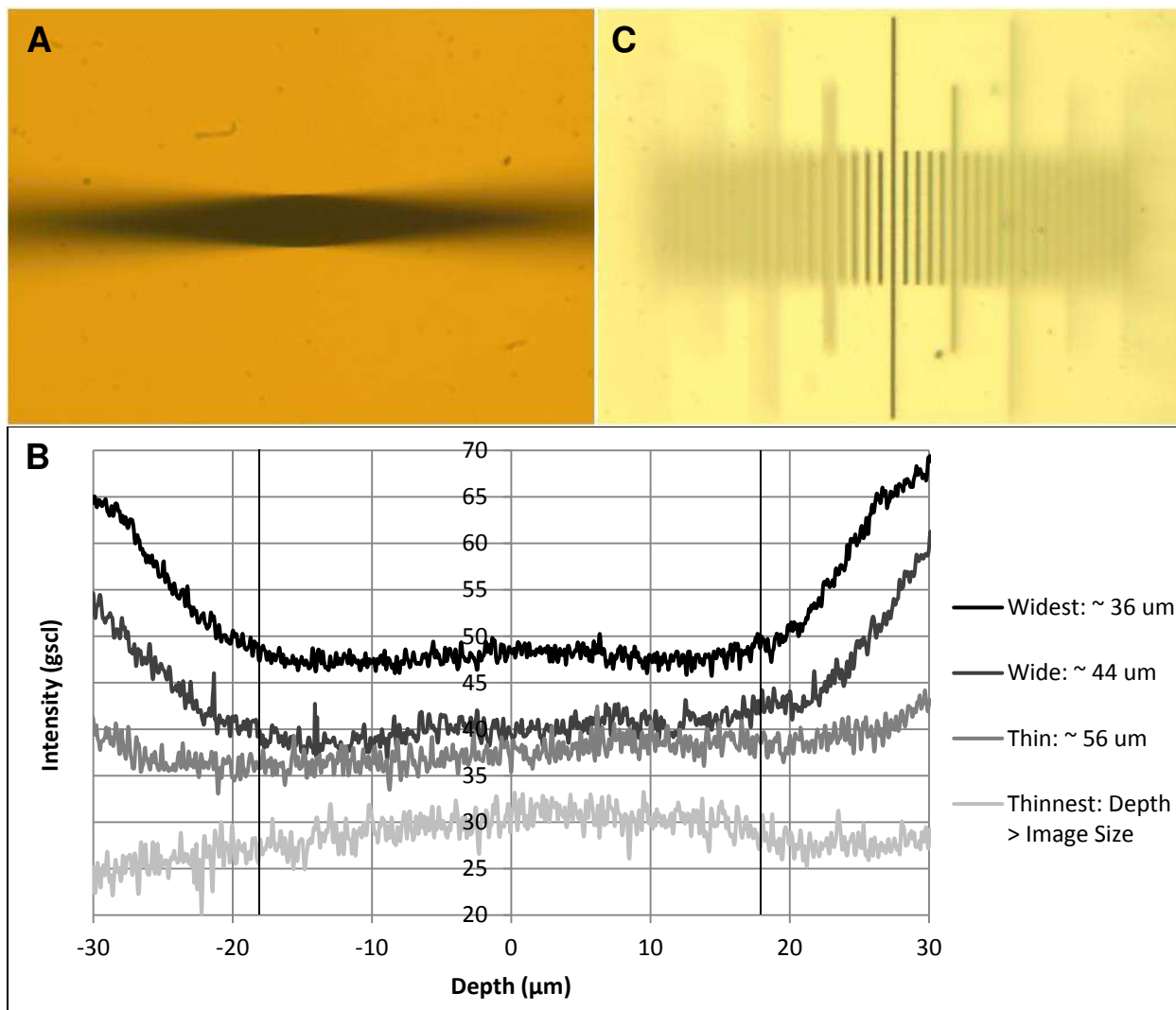


Figure 4.2: Focal Depth Determination and Z-Axis Calibration of the Olympus SZX12 Microscope
A: A black line over a transparent slide was positioned at a known angle under the Olympus SZX12 Bright-Field Stereomicroscope with an SZX-AL20X lens attachment and the intensity along that line was measured at each aperture setting in order to determine the approximate focal depth of each setting shown in (B). Here the line is shown under the widest aperture setting. **B:** The image intensity in the z-axis direction is shown under four aperture settings of the Olympus SZX12. The focal depth was conservatively approximated as the point at which the intensity begins to increase from the relatively constant mean intensity within the focal plane. The bounds of the approximated focal depth under the widest aperture setting used for experimentation are shown as vertical black lines. **C:** The calibration slide used to calibrate the fine-tuning focal knob of the microscope was placed at the same angle as in (A). The degrees of knob rotation corresponding to a shift in focus between two major gridlines (100 μm) was determined in order to calibrate the focal plane shift of the microscope.

With the desired distance between focal planes of analysis determined, it was then necessary to calibrate the fine-tuning knob on the microscope to the z-axis focal plane shift. To do this, a calibration slide was placed under the microscope at a known angle

as was done to determine the focal depth (Figure 4.2C). Once the microscope was zoomed in to the desired spatial resolution, one of the major gridlines on the calibration slide was brought into focus, and the position on the fine-tuning knob was noted. The fine tuning knob was then slowly turned until the next major gridline was brought into focus, and then the depth corresponding to the distance between gridlines was calculated from the angle of the slide. After multiple repetitions, it was determined that 8° of rotation on the fine-tuning focal knob corresponded to a $100\ \mu\text{m}$ shift in focal plane position, so the knob had to be rotated about 1.44° in order to achieve an $18\ \mu\text{m}$ shift. It is expected that in the near future, this methodology will be used with a microscope that incorporates a mechanically-automated stand such that movement between focal planes is more accurate. Due to the size of the fine-tuning knob used on the Olympus SZX12, however, the human error associated with knob adjustment was $\pm 0.25^\circ$, resulting in a z-axis error of $\pm 3.125\ \mu\text{m}$. This error was applied to data acquired from analysis of a test embryo so as to examine the error propagated by the developed algorithm in its output parameters descriptive of overall heart function. An analysis of the effect of this error on these parameters will be illustrated in the results section.

4.2 Methods: Estimating the Shape of the Intracardiac Flow Profile

The first limitation of two-dimensional spatiotemporal analysis lies in the assumption that the intracardiac flow profile is circular with a diameter visible on a single focal-plane. By measuring the diameter, or technically the width, of the interior heart on multiple bisecting focal planes, points along the edge of those diameters are able to be

integrated together into an estimated shape of the intracardiac flow profile. By collecting diameter data from each focal plane at each time step across the cardiac cycle, a profile area is able to be calculated at each time step to more accurately calculate flowrate across the cycle. After image sequences of the embryonic heart are captured on each focal plane, the region used to crop out the heart in the KAT software is saved so that the same region can be used to crop out the heart in the image sequences from the adjacent focal planes. The same is done with the reference lines used to measure diameter and velocity so the exact same region along the x-y plane is measured on every focal plane. When measuring diameter using KAT, careful attention is paid when selecting diameter points so that diameters from the outermost interior diameter are not selected when blurred and out-of-plane, and that only points on endothelial cells along the edge of the heart that are clearly visible are selected.

When diameter data is integrated together, the orientation of the points along the edge of the diameters with respect to each other is not saved from the original KAT analysis. Therefore, the diameters points are oriented such that their centers are aligned on the z-axis, producing a parallel shape. Though this affects the estimated shape of the edge of the profile, it does not affect the estimated area due to Cavalieri's Principle. Cavalieri's Principle states that if two regions in a plane are bisected by line segments of equal length, then the regions have equal areas [115]. Therefore, since the measured diameters can be treated as line segments and the intracardiac flow profile the plane, the estimated area between the diameters will be unaffected by their orientation with respect to each other. By generating an estimated curvature around the

line segments bisecting those two regions, the estimated area within the curvature may not be the same. However, because the difference in those areas is based on an estimate, that difference would be negligible, and therefore an aligned-diameter orientation is used to generate the least error in curvature estimation.

The first method of curvature estimation attempted was through the use of Cartesian spline segments. The radii of each of the diameters were oriented on the y-axis and separated by the distance between focal planes along the x-axis such that a third-degree polynomial could be fit through each of the points. Six separate third-degree polynomial spline segments were used between each of the five radii points and two estimated endpoints that were to be intersected by an infinite slope. The use of third-degree for the order of each spline segment was determined to result in the most accurate estimation because it allows for both the slope and curvature of adjacent spline segments to be matched at each point, unlike with lower-degree polynomials. Additionally, higher-degree polynomials generate more noise within each segment. The use of Cartesian spline segments ended up proving to be unsuccessful when applied to test data, as the use of infinite slopes at the estimated endpoints resulted in drastically unnatural curvature between radii points. By converting the Cartesian diameter points to a polar coordinate system (Figure 4.3), polar spline segments using third-degree polynomials of radius, r with respect to angle, θ with the origin at center of the diameter on the middle focal plane resulted in little error. Using polar spline segments also allows for endpoints on the z-axis to be estimated by simply calculating the radius of the generated spline segments at the points passing through $\theta=\pi/2$ and $3\pi/2$ radians.

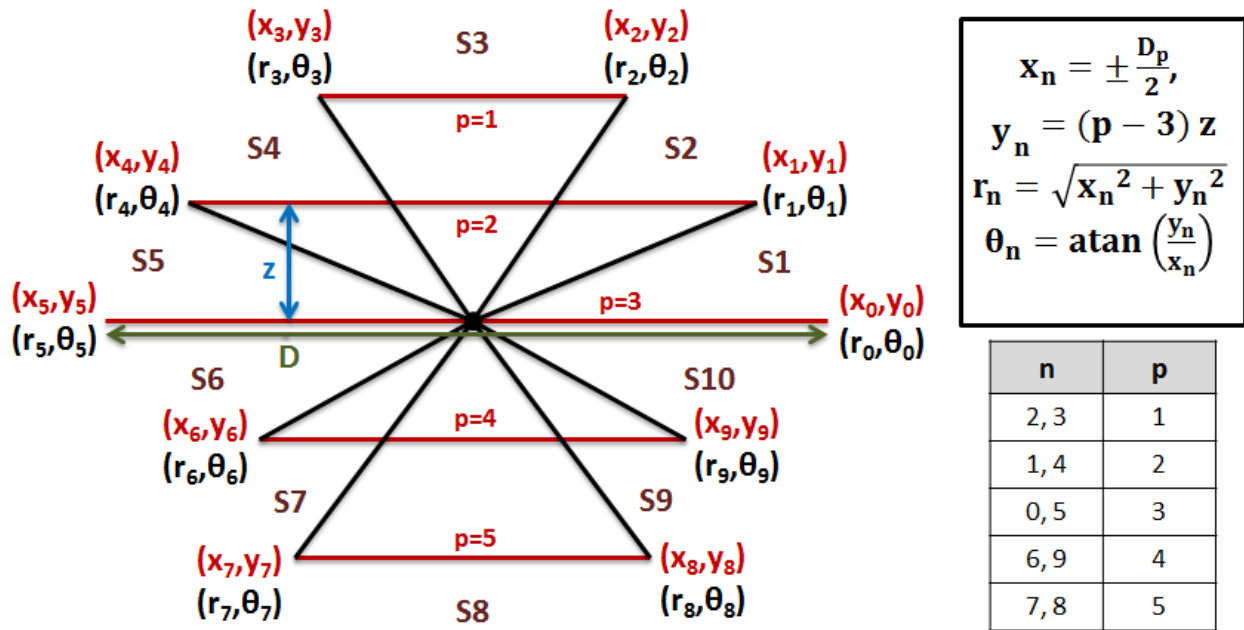


Figure 4.3: Generation of Polar Points about the Intracardiac Flow Profile from “Diameters” Measured on Separate Focal Planes through Spatiotemporal Analysis

Polar coordinates of (r_n, θ_n) are generated from Cartesian coordinates of (x_n, y_n) where values of x_n are generated from radii of the measured “diameters” (red lines) on each focal plane using KAT software and values of y_n are generated from the distance between focal planes. S1-S10 designates the location in which each polar spline segment will be generated to connect each of the polar points.

Before generating polar coordinates from diameter data at each time step in the cardiac cycle, the number of diameters used to generate points for which to connect spline segments is first determined. If no region within the interior of the heart is visible along a reference line in a particular focal plane, which is often the case during systole on the outermost focal planes, then diameter points are positioned directly over each other to achieve a zero diameter. Since human error limits accuracy in diameter measurements to ± 1 pixel, which corresponds to $\pm 0.98 \mu\text{m}$, points generated from diameters less than $1 \mu\text{m}$ are excluded from the intracardiac flow profile so that spline segments do not pass through them. When a diameter on only one focal plane is greater than or equal to $1 \mu\text{m}$, and if that diameter is not greater than the distance between adjacent focal planes (as is typical during systolic contraction), then the circular-profile assumption is again

used. In the case that all diameters are less than 1 μm at a single time step, the largest of those diameters is used in the circular-profile assumption.

After the number of spline segments to be generated, m , is determined, each spline segment polynomial, S_m is created with the coefficients, a_m , b_m , c_m , and d_m (equation 4.1) such that the polar points, (r_n, θ_n) on either end of the spline segment are intersected (equations 4.3, 4.4):

$$S_m = a_m \theta^3 + b_m \theta^2 + c_m \theta + d_m \quad (4.2)$$

$$r_{m-1} = a_m \theta_{m-1}^3 + b_m \theta_{m-1}^2 + c_m \theta_{m-1} + d_m \quad (4.3)$$

$$r_m = a_m \theta_m^3 + b_m \theta_m^2 + c_m \theta_m + d_m \quad (4.4)$$

In order for the slope at each point, $\partial r_n / \partial \theta_n$, to be continuous, the derivative of S_m and S_{m+1} are also set equal at the point (r_m, θ_m) :

$$3a_m \theta_m^2 + 2b_m \theta_m + c_m - 3a_{m+1} \theta_m^2 - 2b_{m+1} \theta_m - c_{m+1} = 0 \quad (4.5)$$

In order for the curvature at each point, $\partial^2 r_n / \partial \theta_n^2$, to be continuous, the second derivative of S_m and S_{m+1} are also set equal at the point (r_m, θ_m) :

$$6a_m \theta_m + 2b_m - 6a_{m+1} \theta_m - 2b_{m+1} = 0 \quad (4.6)$$

Once both the derivative and second derivative of the final polar spline segment are set equal to the first segment, four equations (4.3-4.6) are obtained for each spline segment with which to solve for the four unknown coefficients of each spline segment polynomial. By generating a $4m$ -by- $4m$ matrix, " Θ " and a vector of length $4m$, " R " from the four equations, a vector of the four coefficients for each spline segment polynomial, " S " is able to be calculated through basic matrix operations:

$$\Theta * S = R \quad (4.7)$$

With each spline segment polynomial generated, the area of the intracardiac profile, $A(t)$ is then able to be calculated by taking the definite integral of each spline segment polynomial, S_m between the points θ_{m-1} and θ_m :

$$A(t) = \sum_{i=1}^m \int_{\theta_{i-1}}^{\theta_i} [a_i \varphi^3 + b_i \varphi^2 + c_i \varphi + d_i] \partial \varphi \quad (4.8)$$

The result of generating polar spline segments to calculate area from a set of five test diameters based on the set of polar spline segments in Figure 4.3 is shown below in Figure 4.4.

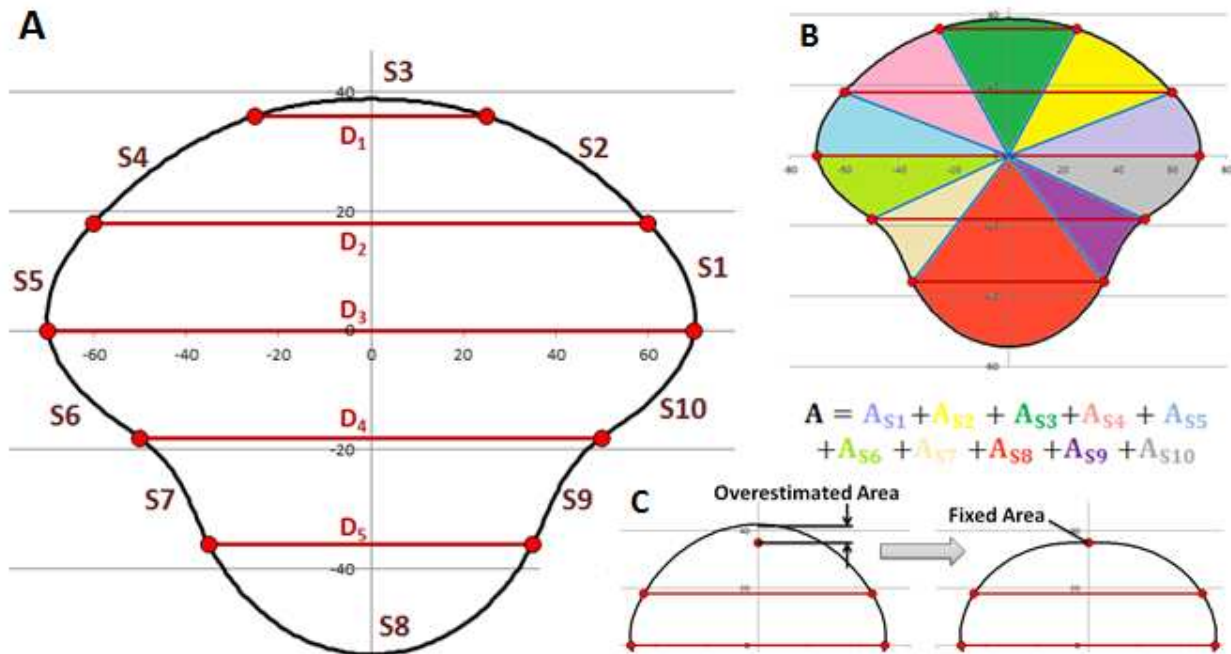


Figure 4.4: Area Calculation of the Intracardiac Flow Profile and Associated Error Resolution
A: Ten polar spline segments (black, S1-S10) were generated from points on the outer edge of the five test diameters (red, D₁-D₅) from Figure 4.3. **B:** Area calculation using definite integrals of the polar spline segment polynomials is illustrated using different colored regions representing the area calculated across each individual segment. Blue lines are used to represent the limits of each definite integral. **C:** When a point is excluded from polar spline segment generation, occasionally the spline segment will pass beyond that point, resulting in an overestimated area. By forcing the spline segments to pass through that point, a more accurate area estimation is obtained.

Occasionally, when diameters less than 1 μm are excluded from polar spline segment generation, the spline segments will pass beyond that focal plane, resulting in an

overestimated area calculation (Figure 4.4C). Therefore at each time step in the cardiac cycle, if any diameters are excluded, two to three sets of spline segments are generated and mutually compared to account for this error: The first is the normal set of spline segments generated as if the diameters are excluded. The second and third set of spline segments are generated as if they are forced to pass through the points of zero diameter along the z-axis on either side of the focal planes to those of diameters greater than 1 μm . If the area calculated within the set of spline segments generated by forcing them through the points on the z axis is less than that of when those points are excluded, then the former area is used as the intracardiac profile area at that time step.

Once the intracardiac flow profile area is calculated at each time step across a cardiac cycle, gaps in the data at various time points are often output as NaN (not a number). This output is due to a calculated infinite area as a result of one of the polar spline segments essentially failing to close the loop and resulting in error. These gaps are replaced by interpolating between area values at the next closest time points in the cardiac cycle in which real areas are measured. The interpolated values create sharp angles in the otherwise smooth area curve over the cardiac cycle, so curve smoothing is performed by averaging contiguous area values together at each time step.

4.3 Methods: Estimating Mean Velocity, Flowrate, and Further Parameters

Through calculating velocities at the center of the flow profile in image sequences on multiple focal planes, the second critical limitation of two-dimensional spatiotemporal

analysis is addressed. As discussed in the literature review, the mean velocity was determined to be proportional to the measured center velocity by a factor of 0.74, which was determined through analysis of the flow profile at only one region of the heart [55]. This may not be the case at all regions of the heart, and during all times throughout the cardiac cycle, therefore by using multiple velocities on multiple focal planes, the mean velocity can be generated through an estimated velocity profile at each time point across the cardiac cycle. To generate a velocity profile, a Riemann sum is taken of the velocities along the z axis across focal planes (Figure 4.5).

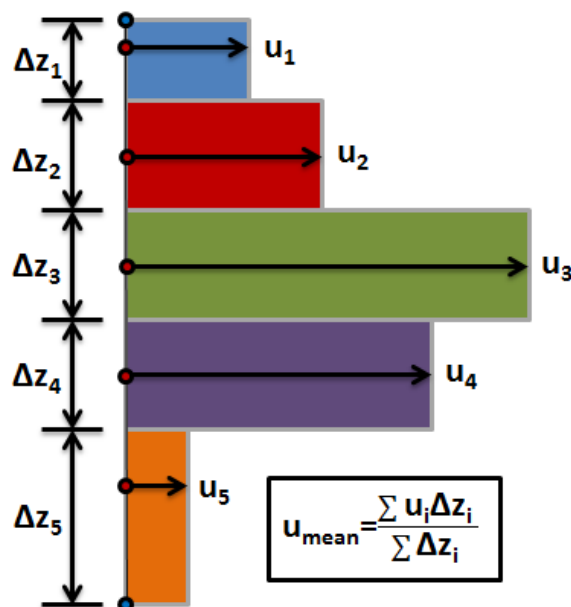


Figure 4.5: Mean Velocity Calculation of the Intracardiac Flow Profile through Riemann Sums

To calculate mean velocity at each time step across the cardiac cycle, rectangles are generated with an area equivalent to the product of the velocity at the z-axis position within that rectangle and the width of the rectangle along the z-axis. Endpoints of each rectangle on the z-axis are set at the midpoints between the z-axis positions of the focal planes of each velocity (red dots), and the outermost endpoints of rectangles 1 and 5 (blue dots) are determined from the position of the radius of the generated polar spline segments (Figure 4.4). The distance between the outermost endpoints is divided from the sum of the rectangles to estimate the mean velocity of the flow profile.

The endpoints of each rectangle along the z axis are at the midpoints between each focal plane of analysis, and the outer endpoints of the outermost rectangles are

determined by calculating the radius of the polar spline segment polynomials at $\theta = \pi/2$ and $3\pi/2$ radians. As with the area data, when a polar spline segment is unable to be generated between two diameter points, gaps in the edge data also result across the cardiac cycle. Therefore, the same methods of interpolation and curve smoothing are applied to the outermost edge data. The total distance between the outermost edge data is then divided from the Riemann sum of the velocities to calculate the mean velocity at each time point as shown in Figure 4.5.

The flowrate across the cardiac cycle is calculated from the product of the area and the mean velocity at each time point. The accumulated volume is then calculated through the same method used in two-dimensional spatiotemporal analysis as shown in Equation 2.6. In between capturing image sequences on each focal plane, the embryo's heart rate experiences minor fluctuations during the ~2-minute download period. Therefore, the heart rate used to calculate the time step corresponding to $1/100^{\text{th}}$ of the cardiac cycle is calculated from the average of the heart rates measured on each focal plane. The stroke volume (SV), cardiac output (CO), and retrograde flow fraction (RF, Equation 2.7) are then calculated through the same process as with two-dimensional spatiotemporal analysis as described in the literature review, in which parameters are ensemble averaged across all cardiac cycles. The results of the analysis are automatically output to an Excel file in the same format as is output by the KAT software, except diameter data across a cardiac cycle is replaced with area data. Parameters across a cardiac cycle are then adjusted so as to align atrial end-diastole at 51% of the cardiac cycle as in Aim 1.

4.4 Results of Multi-Focal Plane Spatiotemporal Analysis on a Test Embryo

Image sequences were captured across approximately six cardiac cycles in a test embryo aged 55 hpf on focal planes bisecting the heart separated by a z-axis distance of $18 \pm 3.125 \mu\text{m}$ (Figure 4.6). The embryo was aligned so that the center of the atrium and ventricle were nearly aligned on the center focal plane, defined by the position $z = 0 \mu\text{m}$. Alignment was not perfect, as the atrium would only cross the furthest focal plane on the ventral side ($z = 36 \mu\text{m}$), and the ventricle would only cross the furthest focal plane on the dorsal side ($z = -36 \mu\text{m}$) for a short duration of each cardiac cycle. All regions of the heart were clearly visible at all times in the cardiac cycle in image sequences taken on focal planes at $z = 0 \mu\text{m}$ and $z = 18 \mu\text{m}$. On the focal plane at $z = -18 \mu\text{m}$, the ventricle was entirely visible during diastole, though not systole, and only about half of the atrium would cross the focal plane during diastole. Only a portion of each chamber would cross the focal plane for a brief period of each cardiac cycle on the outermost planes ($z = \pm 36 \mu\text{m}$). On the focal plane at $z = 36 \mu\text{m}$, cells on the outlying pericardial sac would come into view, which presented some interference for velocity calculations since these cells are static and do not follow the motion of the rest of the heart.

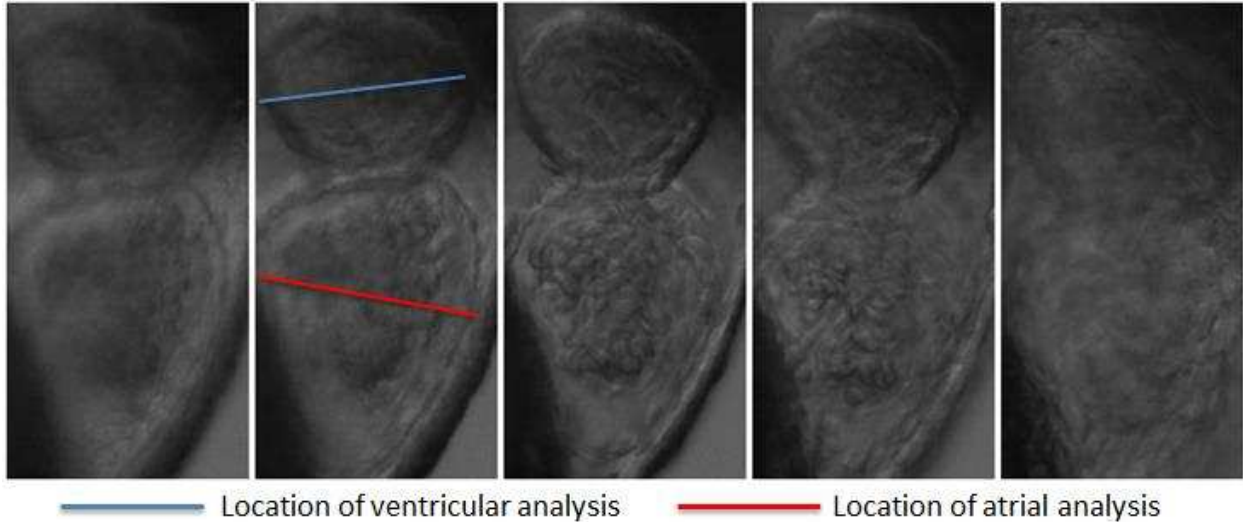
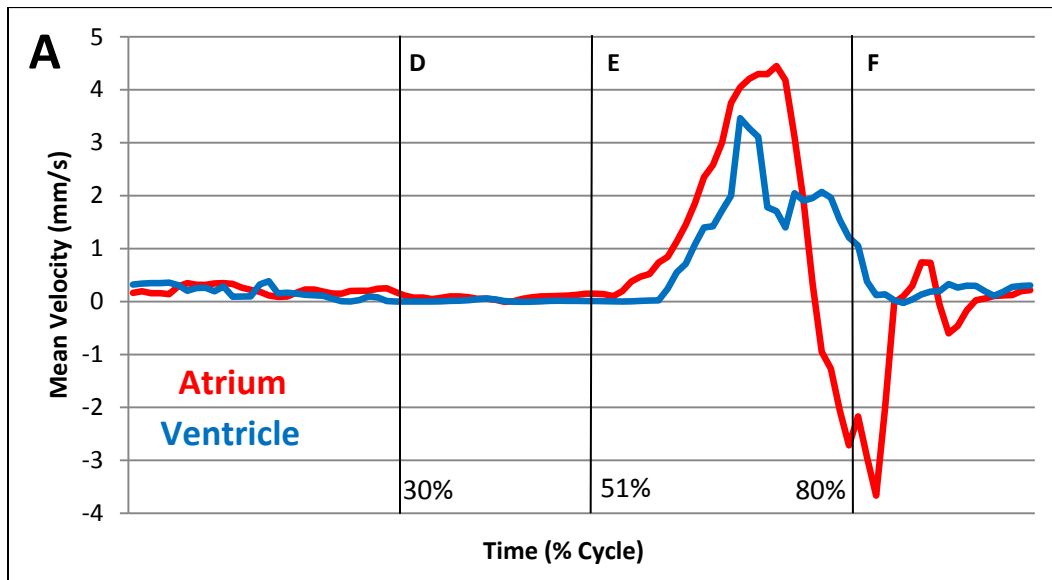


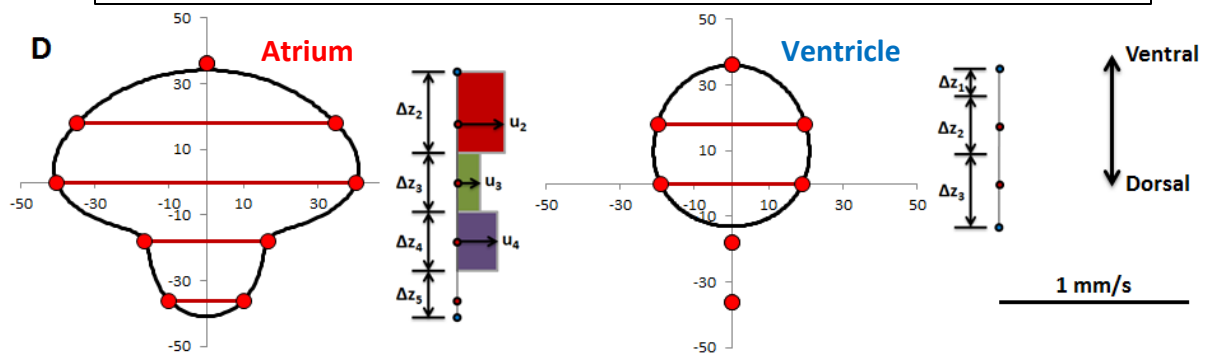
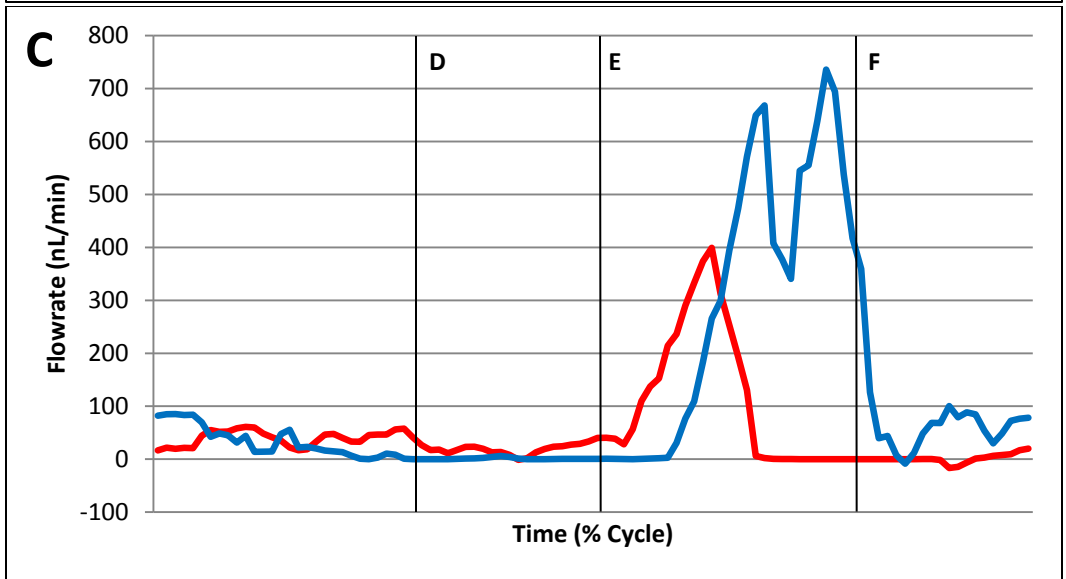
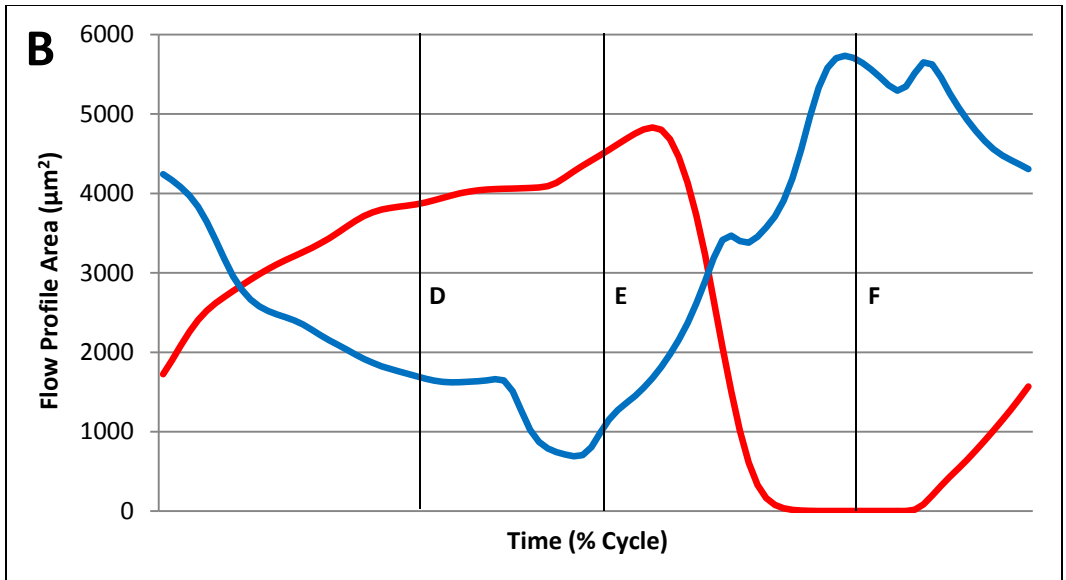
Figure 4.6: Snapshots of the Embryonic Zebrafish Heart on Separate Focal Planes

Images of the heart in a test WT zebrafish embryo at 55 hpf on multiple focal planes separated by a focal plane distance of $18 \pm 3.125 \mu\text{m}$ are displayed. Focal plane positions are defined as along the z axis at (from left to right) $z = -36 \mu\text{m}$, $z = -18 \mu\text{m}$, $z = 0 \mu\text{m}$, $z = 18 \mu\text{m}$, and $z = 36 \mu\text{m}$ where negative positions correspond to more dorsally-oriented planes and positive positions correspond to more ventrally-oriented planes. The upper chamber is the ventricle and the lower chamber is the atrium, and blue and red lines correspond to the locations of reference lines used for spatiotemporal analysis within those chambers.

After the test embryo was analyzed on each focal plane in KAT and the results of the KAT analysis on each focal plane were integrated together using the developed algorithm, the output of the estimated mean velocity, profile area, and flowrate across the cardiac cycle appeared as expected (Figure 4.7A-C, pages 95-96). Regions of area and velocity analysis were likely closer to the anterior and posterior end of the atrium and ventricle, respectively, than the exact center of the chambers, which likely explains the reason that chamber velocities appear nearly in-sync, as will be discussed in greater detail in the following discussion section. The end-diastolic area of the ventricle in this embryo appeared greater than that of the atrium, which was not apparent under two-dimensional spatiotemporal analysis when the embryo was oriented as in Aim 1 and in previous research. Though the order of magnitude in profile area of the ventricle was greater than expected, the change in profile area across the cardiac cycle exhibited the

same characteristics to that previously observed for both chambers. When the flowrates are examined, there is significant discrepancy between chambers in the magnitude of the overall flowrate across the cardiac cycle, as the maximum ventricular flowrates seen during ventricular diastole are far greater than the maximum atrial flowrates seen during the onset of atrial ejection. At three time points in the cardiac cycle, atrial mid-diastole/ventricular mid-systole (30% of the cycle), atrial end-diastole/ventricular end-systole (51% of the cycle), and atrial end-systole/ventricular end-diastole (80% of the cycle), the estimated shape of the intracardiac flow profile and Riemann sum of the velocity profile were observed to better understand the output of the estimated parameters and examine any associated error (Figure 4.7D-F, pages 96-97).





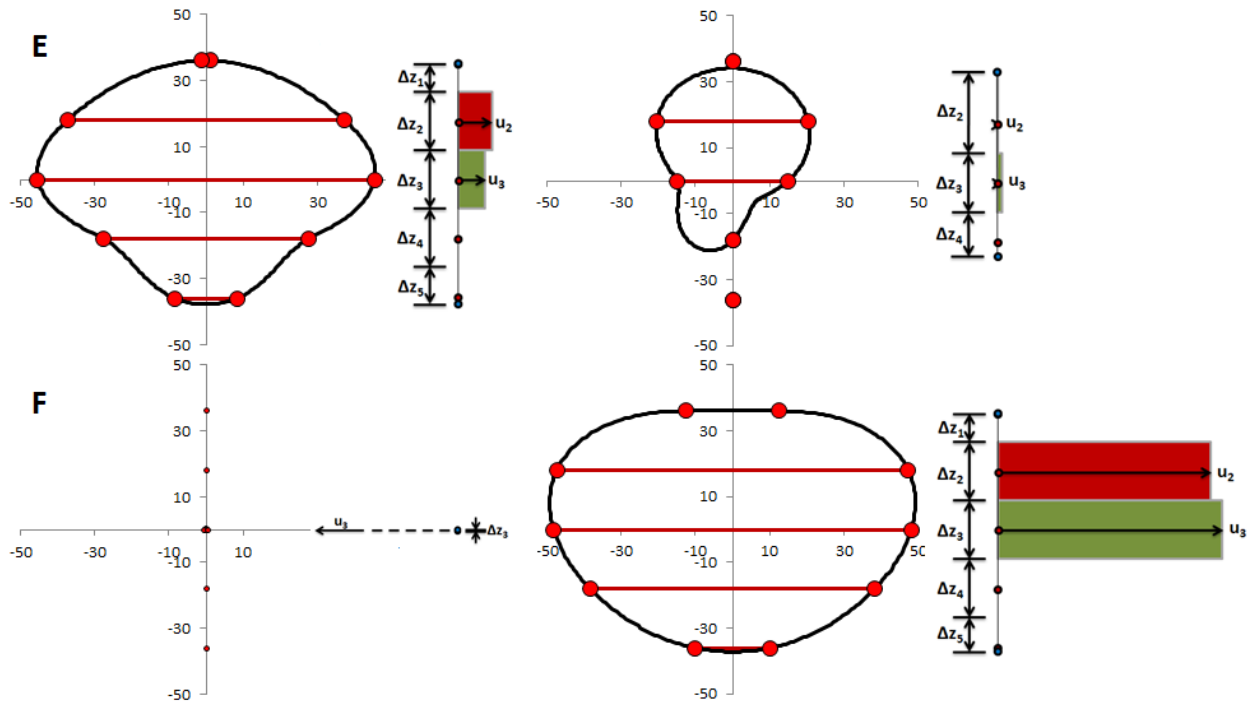


Figure 4.7: Output Parameters Across a Cardiac Cycle using Multi-Focal Plane Spatiotemporal Analysis on a Test Embryo

A: The estimated mean velocity across a cardiac cycle in a test WT embryo at 55 hpf measured through Riemann sums of the velocity profile is shown. The mean velocity at the center of the atrium is shown in red, and at the center of the ventricle is shown in blue. **B:** The estimated profile area in a test embryo across a cardiac cycle calculated through the definite integral of generated polar spline segment polynomials is shown in the atrium (red) and ventricle (blue). **C:** The estimated flowrate in a test embryo across a cardiac cycle calculated through the product of the mean velocity in (A) and the profile area in (B) is shown in the atrium (red) and ventricle (blue). **D:** The estimated shape of the intracardiac flow profile generated through polar spline segments (black lines) intersecting the endpoints of measured “diameters” (red lines) and the associated Riemann sums of the velocities on each focal plane in a test embryo at atrial mid-diastole (left) and ventricular mid-systole (right) (30% of the cardiac cycle) are shown. **E:** at atrial end-diastole (left) and ventricular end-systole (right) (51% of the cardiac cycle). **F:** at atrial end-systole (left) and ventricular end-diastole (right) (80% of the cardiac cycle). The scale of figures **D-F** are equivalent, units of length are in μm and units of velocity are in mm/s . Locations of analysis within the heart are shown in Figure 4.6.

The output of the parameters descriptive of overall heart function under multi-focal plane spatiotemporal analysis were compared with that of under the original two-dimensional analysis method on each focal plane in Table 4.1. To determine the accuracy of any method of flow-measurement in a continuous flow system, the difference in downstream flowrate is examined since flow must be conserved. Because flow in the embryonic heart undergoes cyclic change over a cardiac cycle, the difference

in stroke volume between chambers was measured to calculate the downstream error in stroke volume. When using the original two-dimensional spatiotemporal analysis method, the focal plane of analysis would be positioned across the heart subjectively, so downstream stroke volume difference using the multi-focal plane method was compared with that of the original method on all of the focal planes as well. Though downstream stroke volume difference was as high as 0.47 nL using the multi-focal plane method, it was nearly half the downstream difference measured using the original method on the image sequence acquired from the center focal plane. It is also important to note that despite the fact that the stroke volume difference was less on focal planes further from the center of the chamber, the ratio of this difference to the average measured stroke volume was as high as 200%, indicating significant error when applying 2-D spatiotemporal analysis to images captured on these focal planes.

Table 4.1: Output Parameters Descriptive of Overall Heart Function using both Multi-Focal Plane Spatiotemporal Analysis and Two-Dimensional Spatiotemporal Analysis on a Test Embryo

The cardiac output (CO), retrograde flow fraction (RF), and stroke volume (SV) measured in a test WT embryo at 55 hpf using two-dimensional spatiotemporal analysis on five separate focal planes is shown compared with that of the same embryo using multi-focal plane spatiotemporal analysis in both the atrium and ventricle. The downstream stroke volume difference is the magnitude of the difference in stroke volume measured between the atrium and the ventricle.

Parameter:	Atrium CO (nL/min)	Ventricle CO (nL/min)	Atrium RF	Ventricle RF	Atrium SV (nL)	Ventricle SV (nL)	Downstream SV Difference (nL)
Multi-Focal Plane:	49.8	115.8	0.008	0.001	0.352	0.819	0.467
2-D @ z = 36 μm	1.4	0.0	0.000	0.439	0.01	0.00	0.01
2-D @ z = 18 μm	46.0	5.6	0.000	0.000	0.33	0.04	0.29
2-D @ z = 0 μm	44.4	160.4	0.019	0.001	0.31	1.12	0.81
2-D @ z = -18 μm	2.3	145.4	0.023	0.000	0.15	0.13	0.78
2-D @ z = -36 μm	0.0	0.0	0.000	0.000	0.00	0.00	0.00

As stated in the methods section, because the fine-tuning knob in which to set the position of the focal plane of analysis was adjusted manually, the error associated with the z-axis distance between focal planes was $\pm 3.125 \mu\text{m}$. In order to determine how this error affected the overall accuracy of the analysis used on the test embryo, propagation of error was calculated from the diameter and velocity data measured from the test embryo. Because area was calculated through definite integration of polar spline segment polynomials that were generated conditionally based on the number of “diameters” greater than $1 \mu\text{m}$, the error in area estimation was determined using the test embryo such that the focal plane distances were set at its error bounds, and the diameters and velocities were set at their error bounds of $\pm 0.98 \mu\text{m}$ and $\pm 0.0256 \text{ mm/s}$, respectively. The maximum difference in each parameter output by the multi-focal plane algorithm using each error bound was determined to be the approximate error of that parameter. The approximate propagated error associated with each parameter has been presented below in table 4.2:

Table 4.2: Error in Diameter, Velocity, and Distance Between Focal Planes and Associated Propagated Error of Estimated Parameters

The propagated error in each parameter calculated through the multi-focal plane method of spatiotemporal analysis was calculated from both the human error associated with the diameter and distance between focal planes, and the error in the center velocity associated with the capacity of the Radon transforms under the spatial and temporal resolution of 1024 pixels/mm and 1000 frames/s, respectively. Because area was calculated conditionally based on the number of nonzero “diameters,” at each time point, the error bounds were applied to the test embryo data and error was calculated from the difference in parameter outputs, rather than derived.

Parameter	Symbol	Error
Diameter	D	$\pm 0.98 \mu\text{m}$
Distance Between Focal Planes	Δz	$\pm 3.125 \mu\text{m}$
Velocity (center)	u	$\pm 0.0256 \text{ mm/s}$
Mean Velocity	u_{mean}	$\pm 0.0314 \text{ mm/s}$
Profile Area	A	$\pm 913.27 \mu\text{m}^2$
Flowrate	Q	$\pm 91.14 \text{ nL/min}$
Stroke Volume	SV	$\pm 0.319 \text{ nL}$
Cardiac Output	CO	$\pm 45.04 \text{ nL/min}$
Retrograde Flow Fraction	RF	± 0.0377

4.5 Discussion

The results of multi-focal plane spatiotemporal analysis applied to a test embryo revealed that this method drastically improved upon the downstream stroke volume accuracy measured using two-dimensional analysis (Table 4.1), though this error was still relatively significant. Mean velocities measured at the center of the atrium and ventricle appeared as expected, though a significant difference between chambers in the overall stroke volume and profile areas across a cardiac cycle revealed the most probable source of this error (Figure 4.7A-C). Upon examination of the intracardiac profile areas at various points in the cardiac cycle (Figure 4.7D-F), an irregular and

underestimated atrial profile area was seen due to distortion presented by the limitation of bright-field microscopy. The thickness of the focal planes of analysis also showed to present further error when estimating the profile area of either of the chambers during systole. Fortunately, error propagation analysis (Table 4.2) revealed that errors presented by limitations of the employed imaging modality could account entirely for the difference observed in downstream stroke volume, so it is likely that little downstream stroke volume difference would be observed when other modalities are used with this method.

The atrial inlet and ventricular outlet were positioned nearer to the outermost focal planes of analysis and distorted by the yolk sac and head of the embryo, respectively, therefore the location of the center of the chambers in which areas and velocities were analyzed were actually closer to the AVC than both the inlet and outlet. This is likely the reason that atrial and ventricular pressures appear nearly in-sync during the cardiac cycle. As the atrium ejects, the velocity within the anterior end of the chamber increases as blood is forced into the ventricle. Blood then enters the posterior end of the ventricle at high velocity, which is observed only a few time points after those same velocities are measured in the atrium. When the atrium nears end-systole, high retrograde velocities are observed, as expected, coinciding with decreased forward velocities in the ventricle as the ventricle undergoes diastole. Because retrograde velocities measured in the atrium during systole are typically the product of single RBCs rapidly squeezing through a small orifice of miniscule profile area, these retrograde

velocities translated to retrograde flowrates only on the order of a few picoliters per minute.

The average ratio of the mean velocity to the maximum velocity was measured in order to compare with the ratio used to calculate mean velocity from the centerline velocity in 2-D spatiotemporal analysis of 0.74. In the test embryo, this ratio was calculated to be 0.528, which is much closer to the ratio of 0.5 typically observed in laminar flow-conditions. This is also what would be expected based on the observed shape of the intracardiac flow profile during diastole shown in Figures 4.7D, E, and F. At all time-points during diastole, the width along the z-axis of the intracardiac flow profile in each chamber was greater than the width observed along the x-y plane. Therefore, it makes sense that the ratio of mean velocities measured along the x-y plane to the centerline velocity was greater than the same ratio of mean velocities measured along the z-axis. Though a parabolic velocity profile is characteristic of flow under these conditions, velocities were observed to be significantly greater at the center of the chamber than on the outermost focal planes, which would often detect no velocity throughout the cardiac cycle. The velocity profile in the zebrafish embryo heart has not been analyzed using other flow-measurement methods, however the profile in the forming vessels has been shown to exhibit a blunted parabolic profile due to the low shear stress in the center of the vessel [116]. This is likely the case in the center of the chambers of the forming heart as well.

Since atrial expansion and ventricular contraction occurred over the majority of the cardiac cycle (Figure 4.6), the magnitude of pressures associated with rates of expansion and contraction as described in Aim 1 (Equation 3.7) were far less than that of atrial contraction and ventricular expansion. During atrial diastole and ventricular systole, the highest velocities and flowrates occurred nearer to the atrial inlet and ventricular outlet due to resistance caused by the constriction at the AVC, though retrograde velocities within the AVC can be relatively large when this resistance is overcome, therefore it makes sense that observed velocities and flowrates were lower during this period of the cardiac cycle (Figure 4.6).

As stated in the results, the end-diastolic area of the ventricle was estimated to be greater than that of the atrium, which was not the case when the embryo was analyzed using the previous methodology in the ventral side-up orientation. Despite this, the change in the profile area across the cardiac cycle was similar to that observed using previous methods. The atrial profile area underwent a steady increase during diastole in which the rate of expansion decreased prior to a rapid systolic contraction resulting in an end-systolic profile area of nearly complete closure. In contrast, the ventricular profile area exhibited a more erratic rate of systolic contraction and diastolic expansion, though neither was significantly different from the other in order of magnitude, as was also observed under 2-D spatiotemporal analysis. Additionally, the end-systolic profile area of the ventricle would never reach the nearly-complete closure exhibited by the atrium as well.

The overall magnitude of the estimated flowrate across the cardiac cycle was far greater in the ventricle than measured in the atrium, resulting in the 0.467 nL difference in stroke volume measured between chambers shown in Table 4.1. Because mean velocities in the atrium and ventricle were of relatively similar magnitude throughout the cardiac cycle, this discrepancy in flowrate was likely the result of error in the estimated profile area. Maximum flowrates in the ventricle occurred during ventricular diastole (since analysis of the ventricle was closer to the AVC than the center of the ventricle), however upon examination of the estimated flow profile at ventricular end-diastole (Figure 4.7F), it does not appear that an irregular profile shape was being generated that would result in a significantly overestimated area. Rather, it could be that profile areas of the atrium were underestimated during end-diastole and ejection, when maximum atrial velocities were observed and would have otherwise resulted in flowrates near that observed in the ventricle. The estimated profile area of the atrium at mid and end-diastole (Figure 4.7D-E) show that the measured “diameters” of the atrium on the dorsal side of the heart were much less than those of the center plane and on the ventral side, resulting in an irregular profile shape resembling a reflector light bulb. This was quite unlike the shape suggested by the bean-shaped outer myocardial morphology revealed by confocal images captured in previous studies [34]. Because of this irregular shape, it is likely that the “diameters” measured on those focal planes were underestimated due to some distortion of the heart on one side of the atrium that prevented red blood cells flowing across those planes from appearing in focus. Since careful detail was made to select only in-focus features of the heart as diameter points, these distorted features that were likely actually in-plane were assumed to be out-of-

plane. The shadow cast from the large yolk sac seen in bottom-left corner of the images shown in Figure 4.6 would most likely be responsible for this distortion.

Error in calculated profile area during systole is well represented by the estimated profile area of the ventricle at end-systole shown in Figure 4.7E. Diameters were measured on only two focal planes, which resulted in an overestimated area in which the spline segment on the dorsal side of the heart overlapped the z-axis position of the adjacent focal plane in which no diameter was observed. Therefore, the spline segment was forced through a point on that focal plane, which resulted in the skewed light-bulb shaped profile shown (Figure 4.7E). Despite the fact that the spline segments were forced to pass through that point, they still crossed over the adjacent focal plane, and thus still generated an overestimated area, though not to the extent as if the forced-point were not used.

Figure 4.7F (atrium) illustrates the effect that an estimated small profile area induces on a low retrograde flowrate despite a high retrograde velocity. The velocity at this time point was an order of magnitude greater than of the scale of the figure, though the measured diameter at this time point was an order of magnitude less than the distance between focal planes. Because of the low-measured diameter, the circular-profile assumption was used, despite the fact that profile areas during systole likely exhibit the eccentric deformation illustrated in Figure 3.5. This is primarily the result of the limitation presented by implementing bright-field stereomicroscopy: Though the spatial resolution in two dimensions on a single focal plane is highly accurate, the focal-depth

of this imaging modality is greater than the maximum width of the intracardiac flow profile during systolic contraction. In the future, it is expected that this method of multi-focal plane spatiotemporal analysis will be implemented on image sequences acquired from imaging modalities with a far more resolute focal depth. Therefore it should be possible to more accurately estimate the shape of the intracardiac flow profile at end-systole in further studies.

The improvement in accuracy of the multi-focal plane method of spatiotemporal analysis in comparison to the two-dimensional method is manifested when the output parameters descriptive of overall heart function are examined (Table 4.1). Though two-dimensional spatiotemporal analysis was previously the most accurate method of quantifying intracardiac flow in the embryonic zebrafish, downstream stroke volume difference was as high as 0.81 nL when based solely on data collected from analysis on the center focal plane. Since the positioning of the focal plane of analysis is subjective, if the center plane was assumed to lie along any of the other focal planes analyzed, the downstream stroke volume difference could increase to at least 200% of the average of the stroke volumes measured in both chambers. Though it was expected when using the multi-focal plane method that the difference in downstream stroke volume would be less than 0.47 nL, this turned out to be a significant improvement in comparison with the previous method.

Error associated with subjective positioning of the analysis plane under the two-dimensional method was shown to be further exacerbated in other parameters

descriptive of heart function, especially in retrograde flow fraction. On nearly all focal planes as well as with the multi-focal plane method, retrograde flow fractions never exceeded 3% except on the outermost focal plane on the ventral side of the heart. On this plane, the retrograde flow fraction was nearly as high as 44%, which likely was the result of interference in velocity measurements caused by cells on the pericardial sac. Since those cells do not follow the motion of the heart, it is likely that the movement of the heart in reference to these cells caused them to be analyzed as if they were red blood cells flowing in retrograde, resulting in erroneously large retrograde flowrates.

One limitation of the two-dimensional method of spatiotemporal analysis that has not been addressed in the multi-focal plane method is that only the in-plane component of the velocity on each plane is measured, as illustrated in Figure 4.8. Therefore, the mean velocity and flowrate are likely significantly underestimated since they do not take into account the out-of-plane component, which likely contributes to the overall downstream error in stroke volume. Methods have been developed to calculate out-of-plane velocities in PIV systems by measuring both the increase in diameter and decrease in intensity of particles as they move away from the focal plane [117, 118]. Unfortunately, the density of red blood cells in the embryonic zebrafish heart is too great for the change in size and intensity of each cell to be distinguishable as they move out-of-plane, as too many other RBCs would obstruct their view. Out-of-plane velocities could be measured by capturing image sequences on focal planes bisecting the heart at various different angles by simply rotating the embryo. Not only would this drastically

increase the analysis time however, but it would also be extremely difficult to accurately determine the change in orientation of the embryo between each image sequence.

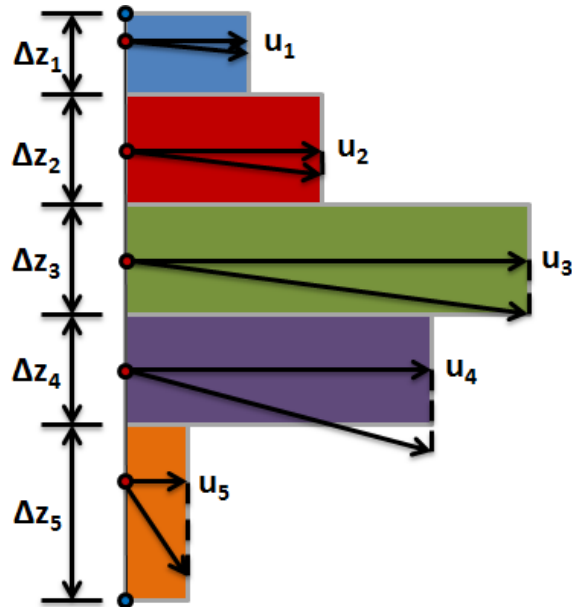


Figure 4.8: Diagram Illustrating the Limitation of Multi-Focal Plane Velocity Estimation

An example Riemann sum of the velocity profile is shown along with a representation of possible magnitudes of the velocity at the z-axis positions of each focal plane (red dots). The velocity measured on each focal plane only captures the in-plane component of that velocity, resulting in an underestimated output of the calculated mean velocity and flowrate.

Unfortunately, this study was limited to the use of a microscope with a manually adjustable knob that induced human error in positioning of the focal plane of analysis to $\pm 3.125 \mu\text{m}$. Though this did not inhibit the capability of developing the methodology, it however resulted in significant error in output parameters when applied to analysis of the test embryo. It is expected that this method of analysis will be implemented in future studies that acquire imaging modalities with a mechanically automated stage with which to shift across focal planes with precision, so the propagated error in each parameter provided in Table 4.2 would not be nearly as great when those modalities are applied.

Due to the spatial and temporal resolution used for analysis on the test embryo of 1024 pixels/mm and 1000 frames/s, respectively, the accuracy in the velocity measured on each focal plane was limited to ± 0.0256 mm/s based on the accuracy of the radon transform analysis as described in the literature review. The estimated output parameter that was affected the least by the significant error in focal plane distance was the mean velocity, which was only as high as ± 0.0314 mm/s, only slightly greater than the error associated with the capacity of the radon transforms. The error propagated in all other estimated parameters was however far more significant. The maximum error in the estimated profile area in the test embryo was $\pm 913.27 \mu\text{m}^2$, which was 21% of the calculated area. The maximum error in the flowrate, measured as the product of both the mean velocity and profile area, was thus ± 91.14 nL/min, which corresponded to 23% of the calculated flowrate. This contributed to an even greater propagation of error in the parameters descriptive of overall heart function. The stroke volume and cardiac output error was as great as 91% of that estimated in either of the chambers, and the retrograde flow fraction was over 3,700% (Table 4.2). Fortunately, this significant propagated error accounted for more than the discrepancy between the stroke volumes measured in each chamber. Therefore, it is likely that the downstream difference in stroke volume observed was the result of the propagation of error in measured diameter and velocity, though most especially the error in distance between focal planes. When the method of multi-focal plane spatiotemporal analysis is applied to imaging modalities with both a mechanically automated stand and smaller focal depth, it is expected that the bulk of the downstream error in stroke volume would be eliminated. As spatial and temporal resolution as well as download speed improves with the advancement of

technology and many focal planes can be analyzed rapidly, the only significant error that should theoretically result from application of this method should be due to out-of-plane velocity measurement which, again, could be reduced through analysis of focal planes oriented at different angles (Figure 4.8). Despite these limitations, this method is still likely the most accurate method to analyze intracardiac flow in embryonic zebrafish. Since the use of zebrafish has become commonplace as an animal model to study heart development in humans and thus the source of congenital heart diseases, this method will be highly beneficial to the field of cardiogenesis research.

5. CONCLUSION

The following chapter provides a summary of the motivation and results of the research conducted as part of this thesis described in chapters 3 and 4. Additionally, this chapter will also present a list of “original contributions,” consisting of all conference presentations, seminars, and articles in progress and in submission pertaining to the research described in this thesis. Finally, an overview of ongoing and potential future work related to the results of this thesis will be presented.

5.1 Summary of Results

The overarching hypothesis of this thesis, that both the pumping and intracardiac flow mechanics of the embryonic heart could be quantified to better understand the mechanical environment influencing heart development, was confirmed. Through gaining an understanding of the relationship of these mechanical influences to various aspects of heart development, the potential causes of congenital heart defects can be studied. Here, the pumping and flow mechanics driving one important mechanistic influence of cardiac development was investigated; that is the retrograde flow at the atrioventricular canal, or the AVC, that influences formation of a valve. Additionally, methodology was developed that allows for a more accurate estimation of various parameters descriptive of intracardiac flow and overall heart function.

In Aim 1, it was hypothesized that retrograde flow was driven by a pressure difference across the AVC associated with simultaneous expansion of the atrium and contraction

of the ventricle, and inhibited by resistance due to systolic closure of the atrium and AVC. This was tested by performing two-dimensional spatiotemporal analysis on high-speed image sequences of the heart in embryonic zebrafish and comparing the results between embryos with normal retrograde flow, and embryos lacking retrograde flow due to reduced cardiac preload induced via centrifugation. Analysis results confirmed this hypothesis as pressures associated with simultaneous expansion and contraction of the atrium and ventricle, respectively, were significantly reduced in embryos without retrograde flow during the period of the cardiac cycle in which retrograde flow would typically occur. These pressures were far greater in control-group embryos earlier in the cardiac cycle though, when retrograde flow would not occur. This inhibition of retrograde flow was thus sufficiently explained by the resistance generated due to the changing length of endocardial closure along the contracted atrium and AVC, which was significantly greater in embryos lacking retrograde flow. The susceptibility of the mechanical environment within the developing heart to minute alterations in the pumping mechanics was thus illuminated by this study. Additionally, since it is assumed that the relationship between retrograde flow and valve formation is the same in humans, once imaging modalities are developed to accurately analyze the mechanical environment within the human embryo heart *in-utero*, the mechanisms described in this aim can be implemented as a diagnostic tool to identify and provide interventional measures to congenital valve defects prior to birth.

In Aim 2, it was hypothesized that by spatiotemporally analyzing the velocity and width of the intracardiac flow profile on multiple focal planes bisecting the heart, that

parameters descriptive of flow and overall heart function could be more accurately quantified in comparison to previous methods. To do this, a complementary algorithm to software used for spatiotemporal analysis on a single focal plane was developed that would integrate together the results of analyses on multiple planes into a single output dataset. Based on the results generated from applying this method to a test embryo, the hypothesis was confirmed, as downstream difference in stroke volume between the center of the atrium and center of the ventricle was reduced by nearly 50%. Though augmentation of the methodology was not hindered, the accuracy of the results when applied to the test embryo were significantly inhibited by the imaging modality implemented for analysis. Fortunately, upon examination of the propagated error in parameters output by the algorithm arising from the limitations in the acquired imaging modality, the difference in downstream stroke volume was sufficiently accounted for. In the future, it is expected that this method of multi-focal plane spatiotemporal analysis will be used with imaging modalities that do not present these limitations, which should increase its accuracy further. Given that the application of embryonic zebrafish as an animal model in the field of embryonic heart development has expanded considerably in recent years, this method will be substantially beneficial.

5.2 Original Contributions

Listed on the following page are the conference presentations, seminars, and articles in submission related to the research described in this thesis:

Conference Presentations

Summer Biomechanics, Bioengineering, and Biotransport Conference, June 2015,

Snowbird, UT (poster presentation):

Bulk, A., Bark Jr., D., Johnson, B., Garrity, D., Dasi, L.P. *Quantitative Analysis Of Heart Function In Embryonic Zebrafish: Retrograde Flow In The Atrioventricular Junction*. Summer Biomechanics, Bioengineering, and Biotransport Conference, June 2015, Snowbird, Utah. Unpublished conference presentation, 2015. Colorado State University, Dept. of Mechanical Engineering.

Rocky Mountain Fluid Mechanics Research Symposium, August 2015, Boulder, CO

(poster presentation):

Bulk, A., Bark Jr., D., Johnson, B., Garrity, D., Dasi, L.P. *Mechanisms Influencing Retrograde Flow Through the Atrioventricular Canal During Embryonic Cardiogenesis*. Rocky Mountain Fluid Mechanics Research Symposium, August 2015, Boulder, Colorado. Unpublished conference presentation, 2015. Colorado State University, Dept. of Mechanical Engineering.

Seminars Given

Cardiovascular Seminar Series, October 21, 2015, Colorado State University College of Veterinary Medicine, Cardiovascular Research Center, Fort Collins, CO:

Bulk, Alexander. "Aspects of Mechanical Flow and Its Relationship to Cardiac Development." Cardiovascular Seminar Series. Colorado State University College of Veterinary Medicine, Cardiovascular Research Center, Fort Collins, CO. 21 Oct. 2015. Lecture.

Articles

In submission: "Mechanisms Influencing Retrograde Flow in the Atrioventricular Canal During Embryonic Cardiogenesis," by Alexander Bulk, David Bark Jr., Brennan Johnson, Deborah Garrity, and Lakshmi Prasad Dasi. This article is based on the research described in Aim 1 in Chapter 3.

5.3 Future Work

Though the results of the experiments in Aim 1 were able to sufficiently explain the mechanics driving the occurrence of retrograde flow in the AVC, these results provide only a single link in the overall regulatory system of valvulogenesis. The mechanotransductive signaling processes linking retrograde flow to expression of the gene, KLF2a, and KLF2a to normal valvulogenesis, are still poorly understood. Ongoing gene expression studies using zebrafish embryos are currently implementing the methods of centrifugation described in Chapter 3 to inhibit retrograde flow and examine its relationship to KLF2a expression using in-situ hybridization. The computational method described in Aim 2 is also being used in these studies to more accurately quantify the parameters of the pumping and intracardiac flow mechanics related to retrograde flow in order to determine how they respond to changes in KLF2a expression. There are likely many other flow-responsive genes other than KLF2a linking valvulogenesis to retrograde flow, so additional studies have begun to apply RNA sequencing to identify any altered flow-responsive genes at the AVC as well as other regions of the heart susceptible to the reduction in preload induced by centrifugation.

It is highly likely that even more future experiments will make use of the methodology of multi-focal plane spatiotemporal analysis, especially those that obtain highly resolute and mechanically-advanced imaging modalities. As stated in chapter 4, when using an imaging modality with a lower focal depth, and a mechanically-automated stand with

which to accurately shift across focal planes, the error in the measured parameters of intracardiac flow could be drastically minimized. If an imaging modality is developed that allows for the microscope to rotate about the specimen similar to the motion of CT or MRI, out-of-plane velocities could be estimated and the accuracy of all parameters could be drastically increased depending on the density of image sequences captured about the heart. Eventually, it is the hope that imaging technology will evolve to the point that non-invasive analysis of human embryos during pregnancy will be possible and that error in computational analysis of intracardiac flow will be negligible. By that point, it is anticipated that this research will have contributed to a more complete understanding of the relationship between various aspects of the mechanical environment in the embryonic heart and cardiac development such that abnormal conditions preceding the formation of congenital heart defects can be diagnosed and treated before birth.

REFERENCES

1. Mitchell, S., S. Korones, and H. Berendes, *Congenital heart disease in 56,109 births incidence and natural history*. *Circulation*, 1971. **43**(3): p. 323-332.
2. Hoffman, J.I. and S. Kaplan, *The incidence of congenital heart disease*. *Journal of the American College of Cardiology*, 2002. **39**(12): p. 1890-1900.
3. Nishimura, R.A., et al., *ACC/AHA 2008 Guideline update on valvular heart disease: focused update on infective endocarditis: a report of the American College of Cardiology/American Heart Association Task Force on Practice Guidelines endorsed by the Society of Cardiovascular Anesthesiologists, Society for Cardiovascular Angiography and Interventions, and Society of Thoracic Surgeons*. *Journal of the American College of Cardiology*, 2008. **52**(8): p. 676-685.
4. Blue, G.M., et al., *Congenital heart disease: current knowledge about causes and inheritance*. *The Medical journal of Australia*, 2012. **197**(3): p. 155-159.
5. Pierpont, M.E., et al., *Genetic basis for congenital heart defects: Current knowledge a scientific statement from the american heart association congenital cardiac defects committee, council on cardiovascular disease in the young: Endorsed by the american academy of pediatrics*. *Circulation*, 2007. **115**(23): p. 3015-3038.
6. McCain, M.L. and K.K. Parker, *Mechanotransduction: the role of mechanical stress, myocyte shape, and cytoskeletal architecture on cardiac function*. *Pflügers Archiv-European Journal of Physiology*, 2011. **462**(1): p. 89-104.
7. Granados-Riveron, J.T. and J.D. Brook, *The impact of mechanical forces in heart morphogenesis*. *Circulation: Cardiovascular Genetics*, 2012. **5**(1): p. 132-142.
8. Santhanakrishnan, A. and L.A. Miller, *Fluid dynamics of heart development*. *Cell biochemistry and biophysics*, 2011. **61**(1): p. 1-22.
9. Hove, J.R., et al., *Intracardiac fluid forces are an essential epigenetic factor for embryonic cardiogenesis*. *Nature*, 2003. **421**(6919): p. 172-177.
10. Jones, E., et al., *Measuring hemodynamic changes during mammalian development*. *American Journal of Physiology-Heart and Circulatory Physiology*, 2004. **287**(4): p. H1561-H1569.
11. Gluckman, P.D., et al., *Effect of in utero and early-life conditions on adult health and disease*. *New England Journal of Medicine*, 2008. **359**(1): p. 61-73.

12. Al Naieb, S., C.M. Happel, and T.M. Yelbuz, *A detailed atlas of chick heart development in vivo*. *Annals of Anatomy-Anatomischer Anzeiger*, 2013. **195**(4): p. 324-341.
13. Zhou, Y., et al., *Applications for multifrequency ultrasound biomicroscopy in mice from implantation to adulthood*. *Physiological Genomics*, 2002. **10**(2): p. 113-126.
14. Stainier, D., R.K. Lee, and M.C. Fishman, *Cardiovascular development in the zebrafish. I. Myocardial fate map and heart tube formation*. *Development*, 1993. **119**(1): p. 31-40.
15. Icardo, J.M., *Endocardial cell arrangement: role of hemodynamics*. *The anatomical record*, 1989. **225**(2): p. 150-155.
16. Liu, A., et al., *Biomechanics of the chick embryonic heart outflow tract at HH18 using 4D optical coherence tomography imaging and computational modeling*. *PLoS One*, 2012. **7**(7): p. e40869-e40869.
17. Hogers, B., et al., *Extraembryonic venous obstructions lead to cardiovascular malformations and can be embryolethal*. *Cardiovascular Research*, 1999. **41**(1): p. 87-99.
18. Liu, A., et al., *Quantifying blood flow and wall shear stresses in the outflow tract of chick embryonic hearts*. *Computers & structures*, 2011. **89**(11): p. 855-867.
19. Chan, J., et al., *Dissection of angiogenic signaling in zebrafish using a chemical genetic approach*. *Cancer cell*, 2002. **1**(3): p. 257-267.
20. Dahme, T., H.A. Katus, and W. Rottbauer, *Fishing for the genetic basis of cardiovascular disease*. *Disease models & mechanisms*, 2009. **2**(1-2): p. 18-22.
21. Ota, S. and A. Kawahara, *Zebrafish: a model vertebrate suitable for the analysis of human genetic disorders*. *Congenital anomalies*, 2014. **54**(1): p. 8-11.
22. Tu, S. and N.C. Chi, *Zebrafish models in cardiac development and congenital heart birth defects*. *Differentiation*, 2012. **84**(1): p. 4-16.
23. Stainier, D.Y., *Zebrafish genetics and vertebrate heart formation*. *Nature Reviews Genetics*, 2001. **2**(1): p. 39-48.
24. Stainier, D., et al., *Mutations affecting the formation and function of the cardiovascular system in the zebrafish embryo*. *Development*, 1996. **123**(1): p. 285-292.
25. Driever, W., et al., *A genetic screen for mutations affecting embryogenesis in zebrafish*. *Development*, 1996. **123**(1): p. 37-46.
26. Schmidt, H., et al., *C-type natriuretic peptide (CNP) is a bifurcation factor for sensory neurons*. *Proceedings of the National Academy of Sciences*, 2009. **106**(39): p. 16847-16852.

27. Hamburger, V. and H.L. Hamilton, *A series of normal stages in the development of the chick embryo*. Journal of morphology, 1951. **88**(1): p. 49-92.
28. Scholz, S., et al., *The zebrafish embryo model in environmental risk assessment—applications beyond acute toxicity testing*. Environmental Science and Pollution Research, 2008. **15**(5): p. 394-404.
29. Kimmel, C.B., R. Warga, and T. Schilling, *Origin and organization of the zebrafish fate map*. Development, 1990. **108**(4): p. 581-594.
30. Kimmel, C.B., et al., *Stages of embryonic development of the zebrafish*. Developmental Dynamics, 1995. **203**(3): p. 253-310.
31. Gittenberger-de Groot, A.C., et al., *Basics of cardiac development for the understanding of congenital heart malformations*. Pediatric research, 2005. **57**(2): p. 169-176.
32. Milgrom-Hoffman, M., et al., *The heart endocardium is derived from vascular endothelial progenitors*. Development, 2011. **138**(21): p. 4777-4787.
33. Goenezen, S., M.Y. Rennie, and S. Rugonyi, *Biomechanics of early cardiac development*. Biomechanics and modeling in mechanobiology, 2012. **11**(8): p. 1187-1204.
34. Bakkers, J., *Zebrafish as a model to study cardiac development and human cardiac disease*. Cardiovascular research, 2011. **91**(2): p. 279-288.
35. Barry, A., *The functional significance of the cardiac jelly in the tubular heart of the chick embryo*. The Anatomical Record, 1948. **102**(3): p. 289-298.
36. Groenendijk, B.C., et al., *The role of shear stress on ET-1, KLF2, and NOS-3 expression in the developing cardiovascular system of chicken embryos in a venous ligation model*. Physiology, 2007. **22**(6): p. 380-389.
37. Nakamura, A. and F.J. Manasek, *An experimental study of the relation of cardiac jelly to the shape of the early chick embryonic heart*. Journal of embryology and experimental morphology, 1981. **65**(1): p. 235-256.
38. Johnson, R.C., et al., *The biochemical and ultrastructural demonstration of collagen during early heart development*. Developmental biology, 1974. **36**(2): p. 252-271.
39. Hurle, J., J. Icardo, and J. Ojeda, *Compositional and structural heterogeneity of the cardiac jelly of the chick embryo tubular heart: a TEM, SEM and histochemical study*. Journal of embryology and experimental morphology, 1980. **56**(1): p. 211-223.
40. Beis, D., et al., *Genetic and cellular analyses of zebrafish atrioventricular cushion and valve development*. Development, 2005. **132**(18): p. 4193-4204.

41. Liebling, M., et al., *Rapid three-dimensional imaging and analysis of the beating embryonic heart reveals functional changes during development*. *Developmental Dynamics*, 2006. **235**(11): p. 2940-2948.
42. Männer, J., A. Wessel, and T.M. Yelbuz, *How does the tubular embryonic heart work? Looking for the physical mechanism generating unidirectional blood flow in the valveless embryonic heart tube*. *Developmental Dynamics*, 2010. **239**(4): p. 1035-1046.
43. Johnson, B.M., D.M. Garrity, and L.P. Dasi, *The transitional cardiac pumping mechanics in the embryonic heart*. *Cardiovascular Engineering and Technology*, 2013. **4**(3): p. 246-255.
44. Jaffrin, M. and A. Shapiro, *Peristaltic pumping*. *Annual Review of Fluid Mechanics*, 1971. **3**(1): p. 13-37.
45. Forouhar, A.S., et al., *The embryonic vertebrate heart tube is a dynamic suction pump*. *Science*, 2006. **312**(5774): p. 751-753.
46. Hickerson, A.I., D. Rinderknecht, and M. Gharib, *Experimental study of the behavior of a valveless impedance pump*. *Experiments in Fluids*, 2005. **38**(4): p. 534-540.
47. Loumes, L., I. Avrahami, and M. Gharib, *Resonant pumping in a multilayer impedance pump*. *Physics of Fluids (1994-present)*, 2008. **20**(2): p. 023103.
48. Maes, F., et al. *The pumping mechanism of embryonic hearts*. in *5th European Conference of the International Federation for Medical and Biological Engineering*. 2012. Springer.
49. Lee, V.C., et al., *Experimental investigation of open loop multi-stage impedance pumping system*. *Journal of Engineering Science and Technology*, 2011. **6**(5): p. 551-557.
50. Johnson, B., et al., *Altered mechanical state in the embryonic heart results in time-dependent decreases in cardiac function*. *Biomechanics and modeling in mechanobiology*, 2015: p. 1-11.
51. Miller, L.A., *Fluid dynamics of ventricular filling in the embryonic heart*. *Cell biochemistry and biophysics*, 2011. **61**(1): p. 33-45.
52. Warren, K.S. and M.C. Fishman, *"Physiological genomics": mutant screens in zebrafish*. *American Journal of Physiology-Heart and Circulatory Physiology*, 1998. **275**(1): p. H1-H7.
53. Sedmera, D., et al., *Functional and morphological evidence for a ventricular conduction system in zebrafish and Xenopus hearts*. *American Journal of Physiology-Heart and Circulatory Physiology*, 2003. **284**(4): p. H1152-H1160.

54. Chapman, R., *Excitation-contraction coupling in cardiac muscle*. Progress in biophysics and molecular biology, 1980. **35**: p. 1-52.
55. Johnson, B.M., *Quantifying function in the zebrafish embryonic heart: A study on the role of timed mechanical cues*. 2014, COLORADO STATE UNIVERSITY.
56. Cummings, B., *Actin-Myosin Sliding Filament Theory*. 2001, Addison Wesley Longman, Inc.
57. Kim, J., P. Moin, and R. Moser, *Turbulence statistics in fully developed channel flow at low Reynolds number*. Journal of fluid mechanics, 1987. **177**: p. 133-166.
58. Fung, Y.-c., *Biomechanics: circulation*. 2013: Springer Science & Business Media.
59. Hierck, B.P., et al., *Fluid shear stress and inner curvature remodeling of the embryonic heart. Choosing the right lane!* The Scientific World Journal, 2008. **8**: p. 212-222.
60. REPLOGLE, R.L., H.J. MEISELMAN, and E.W. MERRILL, *SPECIAL ARTICLE Clinical Implications of Blood Rheology Studies*. Circulation, 1967. **36**(1): p. 148-160.
61. Papaioannou, T.G. and C. Stefanadis, *Vascular wall shear stress: basic principles and methods*. Hellenic J Cardiol, 2005. **46**(1): p. 9-15.
62. Santhanakrishnan, A., et al., *Flow within models of the vertebrate embryonic heart*. Journal of theoretical biology, 2009. **259**(3): p. 449-461.
63. Moore, B.L. and L.P. Dasi, *Coronary Flow Impacts Aortic Leaflet Mechanics and Aortic Sinus Hemodynamics*. Annals of biomedical engineering, 2015: p. 1-11.
64. Yalcin, H.C., et al., *Hemodynamic patterning of the avian atrioventricular valve*. Developmental Dynamics, 2011. **240**(1): p. 23-35.
65. Reckova, M., et al., *Hemodynamics is a key epigenetic factor in development of the cardiac conduction system*. Circulation research, 2003. **93**(1): p. 77-85.
66. Hogers, B., et al., *Unilateral vitelline vein ligation alters intracardiac blood flow patterns and morphogenesis in the chick embryo*. Circulation research, 1997. **80**(4): p. 473-481.
67. Tobita, K., et al., *Three-dimensional myofiber architecture of the embryonic left ventricle during normal development and altered mechanical loads*. The Anatomical Record Part A: Discoveries in Molecular, Cellular, and Evolutionary Biology, 2005. **283**(1): p. 193-201.
68. Brouzés, E. and E. Farge, *Interplay of mechanical deformation and patterned gene expression in developing embryos*. Current opinion in genetics & development, 2004. **14**(4): p. 367-374.

69. Jacob, E., et al., *Influence of hypoxia and of hypoxemia on the development of cardiac activity in zebrafish larvae*. American Journal of Physiology-Regulatory, Integrative and Comparative Physiology, 2002. **283**(4): p. R911-R917.
70. Schirone, R.C. and L. Gross, *Effect of temperature on early embryological development of the zebra fish, Brachydanio rerio*. Journal of Experimental Zoology, 1968. **169**(1): p. 43-52.
71. Malone, M.H., et al., *Laser-scanning velocimetry: a confocal microscopy method for quantitative measurement of cardiovascular performance in zebrafish embryos and larvae*. BMC biotechnology, 2007. **7**(1): p. 40.
72. Carter, K.M., C.M. Woodley, and R.S. Brown, *A review of tricaine methanesulfonate for anesthesia of fish*. Reviews in Fish Biology and Fisheries, 2011. **21**(1): p. 51-59.
73. Topper, J.N. and M.A. Gimbrone Jr, *Blood flow and vascular gene expression: fluid shear stress as a modulator of endothelial phenotype*. Molecular medicine today, 1999. **5**(1): p. 40-46.
74. Li, C. and Q. Xu, *Mechanical stress-initiated signal transduction in vascular smooth muscle cells in vitro and in vivo*. Cellular signalling, 2007. **19**(5): p. 881-891.
75. Knöll, R., *A role for membrane shape and information processing in cardiac physiology*. Pflügers Archiv-European Journal of Physiology, 2015. **467**(1): p. 167-173.
76. Olesen, S.-P., D. Clapham, and P. Davies, *Haemodynamic shear stress activates a K⁺ current in vascular endothelial cells*. Nature, 1988. **331**(6152): p. 168-170.
77. Thi, M.M., et al., *The role of the glycocalyx in reorganization of the actin cytoskeleton under fluid shear stress: a "bumper-car" model*. Proceedings of the National Academy of Sciences of the United States of America, 2004. **101**(47): p. 16483-16488.
78. Franke, R.-P., et al., *Induction of human vascular endothelial stress fibres by fluid shear stress*. 1984.
79. Mammoto, A., T. Mammoto, and D.E. Ingber, *Mechanosensitive mechanisms in transcriptional regulation*. Journal of cell science, 2012. **125**(13): p. 3061-3073.
80. Traub, O. and B.C. Berk, *Laminar shear stress mechanisms by which endothelial cells transduce an atheroprotective force*. Arteriosclerosis, thrombosis, and vascular biology, 1998. **18**(5): p. 677-685.
81. Fujita, M., et al., *Filamin C plays an essential role in the maintenance of the structural integrity of cardiac and skeletal muscles, revealed by the medaka mutant zacro*. Developmental biology, 2012. **361**(1): p. 79-89.

82. Groenendijk, B.C., et al., *Development-related changes in the expression of shear stress responsive genes KLF-2, ET-1, and NOS-3 in the developing cardiovascular system of chicken embryos*. *Developmental Dynamics*, 2004. **230**(1): p. 57-68.
83. Moskowitz, I.P., et al., *Transcription factor genes Smad4 and Gata4 cooperatively regulate cardiac valve development*. *Proc Natl Acad Sci USA*. **201**(1): p. 108.
84. Ruparel, A.A., et al., *Characterization and investigation of zebrafish models of filamin-related myofibrillar myopathy*. *Human molecular genetics*, 2012. **21**(18): p. 4073-4083.
85. Valdés-Mas, R., et al., *Mutations in filamin C cause a new form of familial hypertrophic cardiomyopathy*. *Nature communications*, 2014. **5**.
86. Groenendijk, B.C., et al., *Changes in shear stress-related gene expression after experimentally altered venous return in the chicken embryo*. *Circulation research*, 2005. **96**(12): p. 1291-1298.
87. Vermot, J., et al., *Reversing blood flows act through klf2a to ensure normal valvulogenesis in the developing heart*. *PLoS biology*, 2009. **7**(11): p. e1000246.
88. Dekker, R.J., et al., *Prolonged fluid shear stress induces a distinct set of endothelial cell genes, most specifically lung Krüppel-like factor (KLF2)*. *Blood*, 2002. **100**(5): p. 1689-1698.
89. Komuro, I. and Y. Yazaki, *Control of cardiac gene expression by mechanical stress*. *Annual review of physiology*, 1993. **55**(1): p. 55-75.
90. Goishi, K., et al., *Inhibition of zebrafish epidermal growth factor receptor activity results in cardiovascular defects*. *Mechanisms of development*, 2003. **120**(7): p. 811-822.
91. Kopp, R., T. Schwerte, and B. Pelster, *Cardiac performance in the zebrafish breakdance mutant*. *Journal of experimental biology*, 2005. **208**(11): p. 2123-2134.
92. Lagendijk, A.K., et al., *MicroRNA-23 restricts cardiac valve formation by inhibiting Has2 and extracellular hyaluronic acid production*. *Circulation research*, 2011. **109**(6): p. 649-657.
93. Bartman, T., et al., *Early myocardial function affects endocardial cushion development in zebrafish*. *PLoS biology*, 2004. **2**(5): p. 673-681.
94. Timmerman, L.A., et al., *Notch promotes epithelial-mesenchymal transition during cardiac development and oncogenic transformation*. *Genes & development*, 2004. **18**(1): p. 99-115.

95. Li, P. and R.K. Wang, *Optical coherence tomography provides an ability to assess mechanical property of cardiac wall of developing outflow tract in embryonic heart in vivo*. Journal of biomedical optics, 2012. **17**(12): p. 120502-120502.
96. Jenkins, M., et al., *4D embryonic cardiography using gated optical coherence tomography*. Optics Express, 2006. **14**(2): p. 736-748.
97. Jenkins, M.W., M. Watanabe, and A.M. Rollins, *Longitudinal imaging of heart development with optical coherence tomography*. Selected Topics in Quantum Electronics, IEEE Journal of, 2012. **18**(3): p. 1166-1175.
98. Chen, C.-Y., et al., *Time-resolved OCT- μ PIV: a new microscopic PIV technique for noninvasive depth-resolved pulsatile flow profile acquisition*. Experiments in fluids, 2013. **54**(1): p. 1-9.
99. Chico, T.J., P.W. Ingham, and D.C. Crossman, *Modeling cardiovascular disease in the zebrafish*. Trends in cardiovascular medicine, 2008. **18**(4): p. 150-155.
100. Kagemann, L., et al., *Repeated, noninvasive, high resolution spectral domain optical coherence tomography imaging of zebrafish embryos*. Molecular vision, 2008. **14**: p. 2157.
101. Hassan, Y., T. Blanchat, and C. Seeley Jr, *PIV flow visualisation using particle tracking techniques*. Measurement Science and Technology, 1992. **3**(7): p. 633.
102. Lee, J.Y., H.S. Ji, and S.J. Lee, *Micro-PIV measurements of blood flow in extraembryonic blood vessels of chicken embryos*. Physiological measurement, 2007. **28**(10): p. 1149.
103. Keane, R.D. and R.J. Adrian, *Theory of cross-correlation analysis of PIV images*. Applied scientific research, 1992. **49**(3): p. 191-215.
104. Lee, J., et al., *Moving domain computational fluid dynamics to interface with an embryonic model of cardiac morphogenesis*. PloS one, 2013. **8**(8): p. e72924.
105. Hove, J.R., *Quantifying cardiovascular flow dynamics during early development*. Pediatric research, 2006. **60**(1): p. 6-13.
106. Poelma, C., et al., *Accurate blood flow measurements: are artificial tracers necessary?* PloS one, 2012. **7**(9).
107. Jamison, R.A., et al., *In vivo wall shear measurements within the developing zebrafish heart*. PloS one, 2013. **8**(10): p. e75722.
108. Jamison, R.A., A. Fouras, and R.J. Bryson-Richardson, *Cardiac-phase filtering in intracardiac particle image velocimetry*. Journal of biomedical optics, 2012. **17**(3): p. 0360071-0360077.

109. Johnson, B.M., D.M. Garrity, and L.P. Dasi, *Quantifying function in the early embryonic heart*. Journal of biomechanical engineering, 2013. **135**(4): p. 041006.
110. Kopp, R., B. Pelster, and T. Schwerte, *How does blood cell concentration modulate cardiovascular parameters in developing zebrafish (Danio rerio)?* Comparative Biochemistry and Physiology Part A: Molecular & Integrative Physiology, 2007. **146**(3): p. 400-407.
111. Parrie, L.E., et al., *Zebrafish tbx5 paralogs demonstrate independent essential requirements in cardiac and pectoral fin development*. Developmental Dynamics, 2013. **242**(5): p. 485-502.
112. Westerfield, M., *The zebrafish book*. 1995, University of Oregon Press, Eugene, OR.
113. Guryev, V., et al., *Genetic variation in the zebrafish*. Genome research, 2006. **16**(4): p. 491-497.
114. Männer, J., et al., *High-resolution in vivo imaging of the cross-sectional deformations of contracting embryonic heart loops using optical coherence tomography*. Developmental Dynamics, 2008. **237**(4): p. 953-961.
115. Eves, H., *Two surprising theorems on Cavalieri Congruence*. The College Mathematics Journal, 1991. **22**(2): p. 118-124.
116. Vennemann, P., R. Lindken, and J. Westerweel, *In vivo whole-field blood velocity measurement techniques*. Experiments in fluids, 2007. **42**(4): p. 495-511.
117. Santiago, J.G., et al., *A particle image velocimetry system for microfluidics*. Experiments in fluids, 1998. **25**(4): p. 316-319.
118. Olsen, M.G. and C.J. Bourdon, *Out-of-plane motion effects in microscopic particle image velocimetry*. Journal of Fluids Engineering, 2003. **125**(5): p. 895-901.